UNIVERSITY OF CALIFORNIA
SANTA CRUZ

THE INFLUENCE OF VADOSE ZONE DYNAMICS ON THE MOVEMENT OF RECURRING LANDSLIDES

A dissertation submitted in partial satisfaction
of the requirements for the degree of

DOCTOR OF PHILOSOPHY

in

EARTH SCIENCES

by

Colleen R. Murphy

September 2023

The Dissertation of Colleen R. Murphy
is approved:

_____
Professor Noah Finnegan, chair

_____
Professor Andrew Fisher

_____
Jonathan Perkins, Ph.D.

_____
Peter Biehl
Vice Provost and Dean of Graduate Studies

Table of Contents

List of Figures

List of Tables

Abstract

The Influence of Vadose Zone Dynamics on the Movement of Recurring Landslides

Colleen R. Murphy

When an initial landslide does not fully evacuate all the failed material, remaining deposits may be susceptible to recurring landsliding in the future. These types of consecutive landsliding systems present significant natural hazards and play an important role in landscape evolution, however they are difficult to incorporate into hazard assessments and geomorphic analyses because they violate a commonly held assumption of stationarity. Illuminating the dominant processes that control the behavior and triggering conditions of recurring landslides is critical for improving these assessments.

Landslide movement in the simplest form occurs when the balance of shear stress driving material downslope exceeds the shear strength within a hillslope. In the regime of Coulomb friction, this can be articulated as:

$$\tau = (\sigma - p)tan\varphi + c$$

Where τ is shear stress, σ is normal stress, p is pore-water pressure, φ is friction angle, and c is effective cohesion. For rainfall driven landslides, infiltration of rainwater into the subsurface increases pore-water pressure within the landslide body, thereby reducing effective normal stresses $(\sigma - p)$ and shifting the balance towards landslide movement. Field observations suggest that pore-water pressure rise (and consequently landslide deformation) is controlled by the details of how rainfall

infiltrates through the vadose zone, i.e., the unsaturated region below the ground surface and above the water table.

In this dissertation, I present three studies combining field observations and numerical data to explore the influence of vadose zone processes on recurring landslides. In the first chapter, I synthesize field observations of a large, slow-moving landslide near San Jose, California, USA to explore how lithologically controlled weathering patterns influence earthflow hydrology and deformation. I find that the landslide has a thin weathered zone, comparable to other landslides in the same geologic formation, which results in a small amount of dynamic storage. I propose that this storage capacity constrains the possible range of stress within the landslide body and consequently limits landslide movement as excess water is shed via springs and saturation overland flow once the water table reaches the surface. In the second chapter, I use dynamically downscaled climate model projections to model variably saturated groundwater conditions over 150 years at this same landslide. Using field data from chapter 1, I link the groundwater water data to an empirical model of landslide movement to explore how multiyear precipitation variability will affect future landslide movement. I find that future increases in precipitation variability may lead to a decrease in slow-landslide movement in California, particularly in areas where the amount of possible recharge is precipitation limited. Declining landslide movement is due in part to greater precipitation intensity which diverts rainfall to runoff rather than recharge. Additionally, the impact of wet years on landslide movement is limited by storage constraints and the impact of dry years may

propagate forward for multiple years due to the importance of antecedent saturation state. Finally, in the third chapter, I use numerical experiments to investigate the dominant controls on the reactivation of coastal bluff landslides along Puget Sound, Washington, USA. I find that the changes in hydraulic conductivity and strength from root reinforcement have the greatest impact on the likelihood of landslide reactivation, followed by changes in the properties of the soil water retention curve. Collectively, these studies advance our understanding of vadose zone processes within landslides and the resulting effects on landslide movement.

Acknowledgments

This dissertation would not exist without the generous and extensive support of numerous colleagues, friends, and family. Foremost, I would like to thank my advisor, Noah Finnegan, for his unwavering support, guidance, and scientific curiosity throughout this journey. And extra thanks for always being willing to jump in with a shovel. I would also like to thank my committee, Andy Fisher and Jon Perkins, for their abundant kindness and scientific guidance, both technical and abstract. Their advice greatly improved this dissertation. Thanks also to Ben Mirus, who oversaw the development of Chapter 3 and was an endless source of patient mentorship while I struggled up the learning curve of numerical modeling. Thanks also to Nicole Feldl and Slawek Tulaczyk who provided their technical expertise at important junctures in this research and to Ferdinand Oberle, coauthor on chapter 1, for lending his expertise in electrical resistivity.

Research is rarely a solo endeavor but that is particularly true for fieldwork. Deepest thanks to everyone who ever carried anything or dug a hole at OREO! This work truly could not have been done without you. In particular, thanks to Alex Nereson who first established Oak Ridge Earthflow Observatory; none of this would have been possible without the logistical and academic foundations that Alex built. I would also like to thank other Geomorph group members Em Schnorr and Will Chapman, who have provided invaluable field and emotional support throughout this thesis. Thanks for being there through all the highs and the lows.

Lastly, thanks to all my friends who have been with me through different parts of this journey, and to my family: Mom, Dad, and Sarah. Thanks for all your love and support.

Chapter 1: Vadose Zone Thickness Limits Pore-fluid Pressure Rise in a Large Slow-moving Earthflow

Previously published as:

Murphy, C. R., Finnegan, N. J., & Oberle, F. K. J. (2022). Vadose zone thickness limits pore-fluid pressure rise in a large, slow-moving earthflow. https://doi.org/10.1029/2021JF006415e2021JF006415

Abstract

The rate and timing of hydrologically forced landslides is a complex function of precipitation patterns, material properties, topography, and groundwater hydrology. In the simplest form, however, slopes fail when subsurface pore pressure grows large enough to exceed the Mohr-Coulomb failure criterion. The capacity for pore pressure rise in a landslide is determined in part by the thickness of the unsaturated zone above the water table, which itself is set by weathering patterns that should have predictable patterns across different lithologies. To investigate how this structure affects landslide behavior, we exploit a multi-year record of precipitation, pore pressure, and velocity from Oak Ridge earthflow, a slow-moving landslide set in Franciscan mélange, northern California, USA. In conjunction with electrical resistivity tomography and hydraulic conductivity measurements, these data show that Oak Ridge has a thin weathered profile that is comparable in thickness to other mélange landslides in California. We propose that due to the inherently thin vadose zone, mélange landscapes experience an unusually high water table that frequently brings them close to movement, however the capacity to increase stress is limited by the small amount of dynamic storage available. Instead, excess pore pressure is shed via springs and saturation overland flow once the water table reaches the surface. Linkages between weathering patterns, hydrology, and deformation can explain behavior patterns exhibited by Franciscan mélange earthflows across a large precipitation gradient.

1.1 Introduction

Landslides vary in size, speed, and destructiveness over several orders of magnitude, ranging from rapid, catastrophic hillslope failures that can wipe out roads and towns instantaneously, to slow, persistent mass movements that last over decades or even centuries. The fatalities and property damage that can result from rapid landslides are well known (Fleming & Taylor, 1980; Froude & Petley, 2018). And while the consequences of slow, persistent landslides may not be readily obvious, they nevertheless have a suite of documented impacts ranging from progressive infrastructure damage (Bertolini et al., 2005; Mansour et al., 2011; Nappo et al., 2019) to ecological effects (Beeson et al., 2018) to controls on sediment budgets and landscape evolution on geologic timescales (Kelsey, 1978; Mackey & Roering, 2011; Simoni et al., 2013). Identifying inherent mechanical or hydrological properties of a system that may impose bounds on landslide movement is valuable for forecasting changes in landslide behavior under a changing climate.

To that end, slow-moving landslides are particularly useful because they enable long-term monitoring that can provide insight into the processes governing movement. This broad category generally includes landslides that move from millimeters to meters per year (Hungr et al., 2014), although some classifications include landslides that move up to 100 m/year (Lacroix et al., 2020). They tend to be deep-seated (> 3 m thick; LaCroix et al., 2020) and move persistently or seasonally on the timescale of years to decades (e.g., Chambers et al., 2011; Corominas et al., 2005; Handwerger et al., 2013; Iverson & Major, 1987; Malet et al., 2002; Schulz et

al., 2018; Schulz, McKenna, et al., 2009). Slow-moving landslides occur globally in regions with mechanically weak, clay-rich rocks or soil (Keefer & Johnson, 1983; Lacroix et al., 2020) and typically gentle slopes <20 degrees (Lacroix et al., 2020). Failure plane depth likely coincides with material transitions (e.g., weathering fronts or lithologic contacts) but a broadly applicable standard has not yet been determined.

Stress perturbations from many different sources can trigger movement in these landslides on timescales from minutes to hours. Documented sources of stress perturbations include earthquakes (e.g., Lacroix et al., 2015), undrained loading (e.g., Booth et al., 2018), and atmospheric pressure variations (e.g., Schulz, Kean, et al., 2009). By far the most common driver of movement is groundwater pressure fluctuations resulting from infiltrating precipitation (Corominas et al., 2005; Iverson & Major, 1987; Malet et al., 2002). For this class of landslides, infiltrating rainfall or snowmelt events increase pore water pressure and consequently reduce the effective normal stresses, thereby reducing Coulomb friction (Iverson, 2000; Terzaghi, 1943). Changes in pore water pressure in both space (e.g., Perkins et al., 2017; Reid & Iverson, 1992) and time (e.g., Iverson, 2000; Reid, 1994) control movement.

Observations of pore water pressure changes in response to rainfall at numerous slow-moving landslides suggest that vadose zone processes (Berti & Simoni, 2010; Bogaard & van Asch, 2002; Malet et al., 2005), including fracture flow (Krzeminska et al., 2013), are a critical component to routing water in this system. These vadose zone processes in turn are mediated by properties of the layered soil, weathered rock, and fresh bedrock (and the transitions between these layers) in which

they occur (Montgomery et al., 1997; Onda et al., 2004; Salve et al., 2012). Patterns of this weathered profile should be predictable at the landscape level based on knowledge of lithology, climate, and tectonic history (Riebe et al., 2017). By extension, predictable patterns of weathering should lead to predictable patterns of landslide behavior within a given lithology via the imposed hydrologic controls.

Analyses of slow-moving landslide inventories in California and Italy support this hypothesis. Landslide velocities in the Eel River catchment, northern California Coast Ranges reached historic lows during the 2012-2015 drought (Bennett et al., 2016a) but saw widespread acceleration due to extreme rainfall in 2017 (Handwerger, Fielding, et al., 2019a). These landslides are primarily seated in Franciscan mélange, a tectonically generated block-in-matrix formation characterized by pervasively sheared, fine-grained, and clay-rich matrix material with interspersed blocks of more competent material. Zooming in to a sub-annual scale, analysis of InSAR time series for a subset of 10 of these landslides reveals that they all respond within 40 days to the onset of seasonal rainfall (Handwerger et al., 2013). In Italy, a landslide inventory from the Northern Appenines reveals striking differences in landslide form and kinematic behavior when comparing landslides derived from pelitic flysch and those found in chaotic clay shales with block-in-matrix fabric, yet within each lithology the landslides behave very similarly to each other (Bayer et al., 2018).

These regional scale studies broadly illustrate trends in landslide behavior associated with different lithologies, but they lack the detailed field measurements necessary to illuminate processes that may be at play. Complementing these analyses,

we present here a case study of a large earthflow in the California Coast Ranges and analyze relationships between precipitation, pore-fluid response, and displacement to document how hydrologic constraints on the system affect landslide movement. We discuss implications of our findings for understanding earthflow behavior across a precipitation gradient in California and the potential for this work to be extended in concert with new advances in bedrock critical zone science.

1.1.1 Oak Ridge Earthflow Study Locale

Slow-moving landslides occur in a wide variety of climates and rock types around the world, ranging from shales in Japan to gneiss in the Italian Alps to accretionary prism mélange in the California Coast Ranges (Keefer & Johnson, 1983; Lacroix et al., 2020). Importantly, while these locales may seem disparate, they all share a common thread of weak and/or altered rocks that are characteristic of slow movement. Typically there are also significant clay layers present in the formation that cause water retention through a bathtub effect (Baum & Reid, 2000; Nereson et al., 2018) and provide a discrete failure surface over which the slow landslide can move through frictional sliding (Keefer & Johnson, 1983).

Earthflows, a common form of slow-moving landslides in California, frequently occur in the Franciscan mélange, a subset of the broader Franciscan Complex that formed in a subduction zone off the North American plate during the Mesozoic and early Cenozoic eras (Wakabayashi, 1992). The Franciscan mélange lacks coherent bedding and instead exhibits scale-independent block-in-matrix fabric characterized by a fine-grained deformed matrix interspersed with blocks of variably-

sized, competent rock such as sandstone, schist, serpentine, and chert (Medley, 2001). Within the Franciscan Complex, mélange terranes are often interspersed with more coherent terranes of sedimentary rocks (sandstone at our study site) or occasionally basalt (Rubin, 2002). Although they are often lumped together on geologic maps for simplicity, it is important to both distinguish mélange units from other coherent terranes in the Franciscan Complex and in many cases to distinguish the mélange matrix itself from the some of the larger coherent blocks it may contain due to the different material properties. In these mapping efforts, the fine-grained, mechanically weak nature of mélange means that it can sometimes be difficult to distinguish from colluvial soils (Wakabayashi & Medley, 2004). However, weathered mélange bedrock can be distinguished from colluvial soils by its well-defined matrix foliation and the fact that it does not have a base (Wakabayashi & Medley, 2004). The clay-rich and pervasively sheared nature of the mélange matrix leads to a low shear strength (friction angle (Φ) = 12–14°) (Nereson & Finnegan, 2018; Roadifer et al., 2009) and a general mechanical weakness that is associated with the development of earthflows.

Our study site, Oak Ridge earthflow, is a large, seasonally active, earthflow located in the northern Diablo Range approximately 20 km northeast of San Jose, California, U.S.A. (Fig. 1.1). The Diablo Range is a subset of the California Coast Ranges that broadly marks the border between the eastern side of the Franciscan Complex and the western side of the Great Valley Sequence, a group of late Jurassic to Cenozoic deep-marine sedimentary formations. Locally, geology at Oak Ridge

consists of Mesozoic-early Cenozoic Franciscan Complex rocks (Rubin, 2002). Alternating bands of sandstone and highly sheared, clay-rich mélange comprise the bedrock foundation beneath the earthflow; the landslide body itself is dominated by mélange (Fig. 1.1c). Mélange, both in the body of the landslide and on the surrounding stable slopes, contains fragments of sandstone, chert, greenstone, and blueschist ranging in size from pebbles to large boulders which contribute to a characteristic hummocky topography. Soil cover on the mélange is very thin (~10 cm), hence the subsurface critical zone processes discussed in this paper are primarily relevant to the seasonally unsaturated weathered rock above the water table which can hold large reserves of rock moisture (Rempe & Dietrich, 2018).

Oak Ridge earthflow spans 1.8 km in length (area = 0.35 km^2) along a south-facing slope of Oak Ridge with 600 m of relief and an average slope of 17°. Between 1937 and 2017, Oak Ridge earthflow moved >275 m in the fastest part of the landslide (Nereson & Finnegan, 2018). For a detailed description of the morphology and kinematic zones, see Nereson & Finnegan (2018). Aside from a single man-made cattle pond and periodic livestock grazing, the area is undisturbed by development.

Oak Ridge receives rain and occasional snow mostly between October and April, which is typical for the Mediterranean climate. Average annual rainfall is 52.7 cm (PRISM Climate Group, 2014). Vegetation is dominated by deciduous oak savanna-woodland, grading from predominantly grass cover at the top of the earthflow to denser oak woodland at the toe.

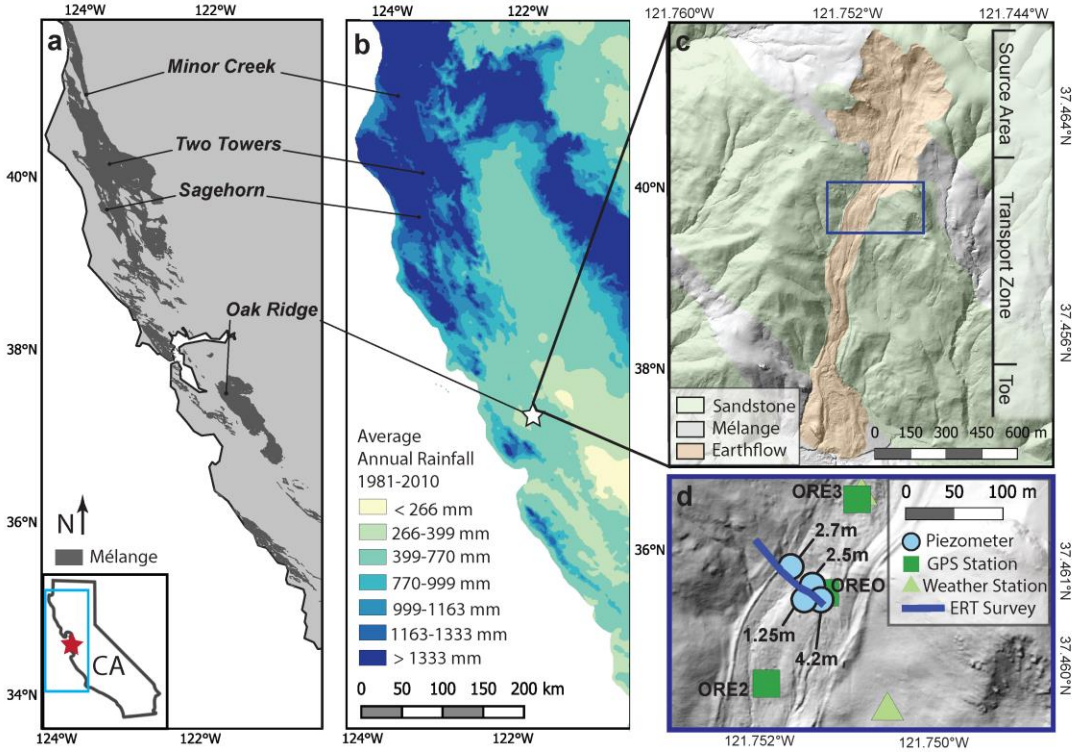

Figure 1.1 | (a) Geologic units in California containing Franciscan mélange (Jennings et al., 1977). Locations of Oak Ridge and three other monitoring sites discussed in this paper – two earthflows (Minor Creek and Two Towers) and one ecohydrology study site (Sagehorn) – are also mapped. Inset map shows extent of 1a and 1b within California. Red star in inset shows approximate location of Oak Ridge. Scalebar in 1b also applies here. **(b)** Average annual precipitation for a thirty-year period from PRISM Climate Group (2014) divided by quantiles. **(c)** Hillshade map of Oak Ridge Earthflow derived from lidar. Bedrock units after (Dibblee, 2006) and (Graymer et al., 2006). Extent of figure 1d shown in blue. **(d)** Location of monitoring equipment. Piezometers are identified by depth and GPS stations by name.

1.2 Methods

1.2.1 Electrical Resistivity

We conducted two electrical resistivity surveys on a cross-section of the landslide, first in June 2018 and then again in November 2018 when we reoccupied the same line. The utility of electrical resistivity to examine the geological structures of landslides and determine groundwater interfaces has long been established (Dahlin, 2001; Perrone et al., 2014). A SuperSting R8 system (Advanced Geosciences Inc.

[AGI], Austin, TX, USA) was used for a survey line that spanned approximately 90 meters (marked in blue on Fig. 1.1d) and used 45 electrodes spaced two meters apart. Each electrode was pinned to the underlying sediment with a 35-cm stainless steel spike. In an effort to minimize known potential errors (Zhou & Dahlin, 2003), each electrode was tested to ensure a good and consistent connection to the ground. For each survey date, we repeated surveys to acquire data in both dipole-dipole and Schlumberger configurations. Apparent resistivity values were calculated based on the known value of current injected and the measured value of voltage at each electrode. We then inverted the results to obtain electrical resistivity tomography. During data processing, we used a topographic profile derived from 3-meter resolution LiDAR to account for influences from variable topography.

1.2.2 Hydraulic Conductivity

Between November 2018 and September 2019, we measured field-saturated hydraulic conductivity in 14 augered boreholes on the earthflow and 6 off the earthflow using the Model 2800K1 Guelph Permeameter, a constant head device available from Soilmoisture Equipment Corp. Boreholes were augered by hand to depths ranging between 27 and 64 centimeters. The average depth on the earthflow was 46 cm and the average depth off the earthflow was 39 cm. All boreholes were augered using the 3-in. diameter auger included in the Guelph permeameter kit and then roughened using the brush attachment to minimize the effects of any smear layers created during the process of augering. Because soil horizons are thin to nonexistent on the landslide body, we consider the measurements on the earthflow

representative of the weathered mélange bedrock. In contrast, the measurements made off the earthflow represent true soil overlying sandstone blocks. Borehole locations and depths are available in Figure 1.9 and Table 1.1 respectively.

All calculations of field-saturated hydraulic conductivity, K_{fs}, were done using the single-head method outlined by Elrick & Reynolds (1992)with the constant $\boldsymbol{\alpha}$ (dependent on soil properties) set at 0.12. When measurements of a steady-state flow rate were achieved for two different head values in the same borehole and at the same depth, we calculated K_{fs} for each head value and averaged the results together per the manufacturer's directions.

1.2.3 Rainfall

We have measured rainfall, temperature, relative humidity, and barometric pressure at Oak Ridge from 27 January 2016 to the present using a Hobo Micro Station Data Logger and sensors manufactured by Onset Corporation. Data reported here cover the period from 27 January 2016 through 12 June 2020. The logger and sensors were mounted on a metal pole planted in stable ground adjacent to the earthflow (Figure 1.1d). All weather data is recorded in 10-minute intervals. The rain gauge operates with a tipping bucket mechanism that sums rainfall in 2-mm increments over the 10-minute interval.

1.2.4 Pore-water Pressure

We installed four non-vented vibrating-wire piezometers (RST Instruments, model VW2100-0.07) on the earthflow to measure pore-water pressure at depths ranging from 1.25 m to 4.2 m below the ground surface (see locations in Figure 1.1d).

Model VW2100-0.07 piezometers are accurate between 70 kPa and 0.07 kPa with a precision of 0.0175 kPa. To install piezometers, we hand-augered boreholes that were later backfilled with a slurry of water, cement, and bentonite (weight ratio 2.49 : 1: 0.41) following the "fully-grouted" method encouraged for vibrating wire piezometers (Contreras et al., 2012). Piezometer readings are taken every 10 minutes and corrected for changes in ground temperature and atmospheric pressure using a linear calibration provided by the manufacturer for each sensor.

During the dry summer, piezometer readings typically either drop far below atmospheric pressure or abruptly revert to zero and maintain that reading until winter when the water table rises above the piezometer depth again. We interpret very negative readings to represent suction under low moisture conditions when the piezometer is far above the water table. When readings abruptly revert to zero, we assume that the pore spaces around the piezometer have equilibrated to atmospheric pressure as a result of the fracture network that forms due to desiccation during the drying period as the water table drops below the piezometer.

1.2.5 Landslide Displacement

To record earthflow displacement, we installed three continuous GPS stations that use Trimble NetR9 receivers and a Trimble GNSS Zephyr antenna. Data are telemetered directly from Oak Ridge to UNAVCO, and then are post-processed with corrected satellite positions at the geodetic laboratory at University of Nevada Reno (Blewitt et al., 2018). Positions are calculated in the North American (NA) terrestrial reference frame which typically has a precision of 1 mm, 0.9 mm, and 3.4 mm in the

north, east, and vertical components respectively. Data reported here come from the middle GPS station (OREO), which has operated continuously from 26 January 2016 to present. See Nereson (2018) for the steps to derive tectonically-corrected positions in the direction of earthflow motion from the UNR data. GPS-derived velocities were calculated over 11-day windows to balance temporal resolution with velocity uncertainty (which increases as the time window gets smaller).

1.2.6 Springs

We mapped the locations and extents of springs, marshes, ponds, and any associated ephemeral streams on 19 February 2019 on the upper half of the landslide. Springs here refer to a source where flowing water transitions from underground to overland flow. We define marshes as areas of soggy ground that have standing water up to a few inches deep which may be disconnected by topographic heterogeneities or vegetation, and ponds as standing water a few inches to several feet deep formed in natural topographic depressions. Most of these hydrologic features are ephemeral and are observed only in the wet season after Oak Ridge has received sufficient precipitation, however a few persist throughout the year, including a prominent perennial wetland in the center of the landslide transport zone.

We also measured discharge at all springs with sufficient flow on 19 February 2019 by recording the cross-sectional area of the associated stream and estimating velocity with a float tracer and a stopwatch. On 15 March 2019, we returned and measured discharge at any springs still flowing by recording the volume of water accumulated in a bucket over a set time interval where topography allowed, and by

measuring cross sectional area and flow velocity in other locations. On 4 September 2019, we were unable to measure flow at any of the springs due to the dry conditions.

1.3 Results

1.3.1 Electrical Resistivity

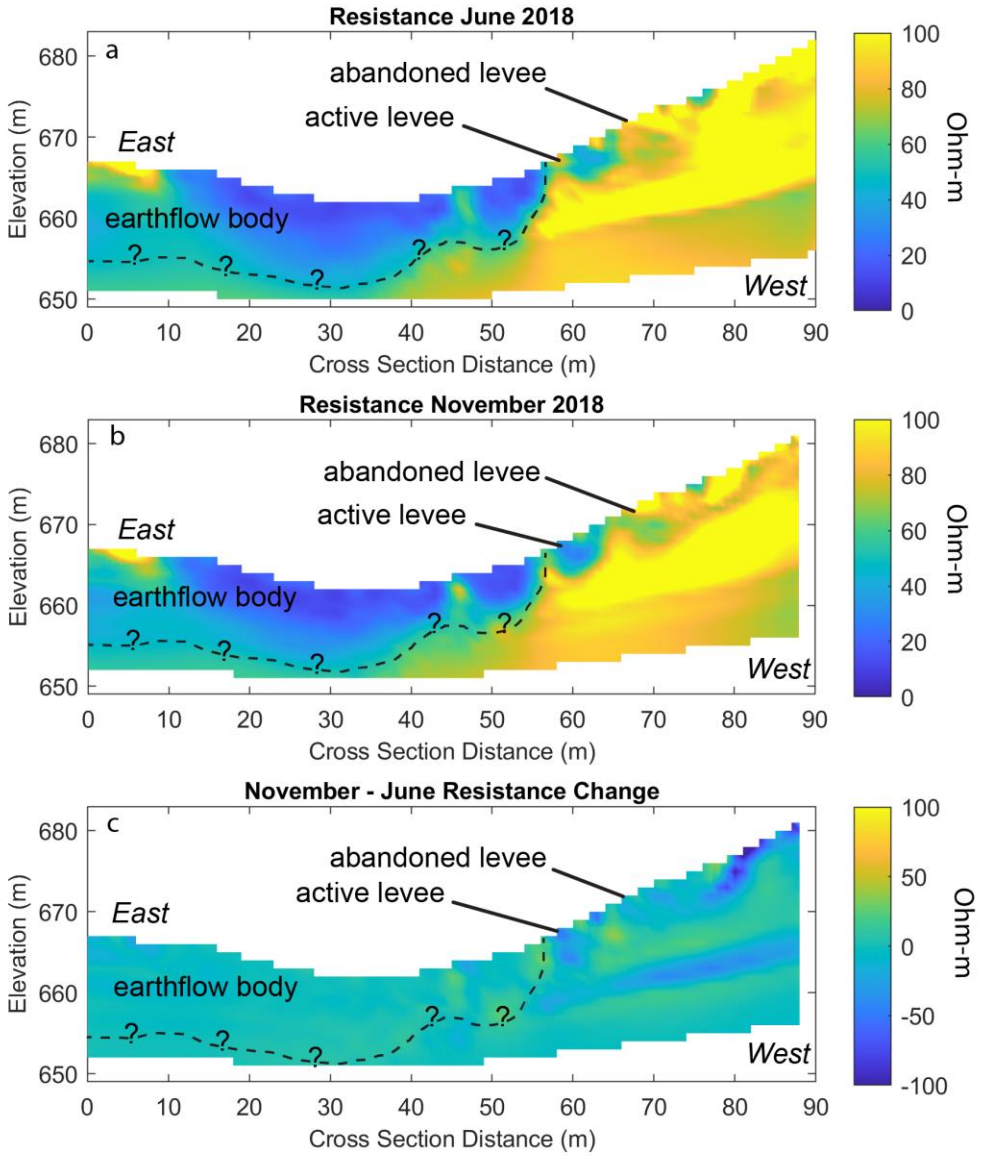

Figure 1.2 Results of the June 2018 **(a)** and November 2018 **(b)** electrical resistivity surveys and the difference between the two **(c).** Units are Ohm-m. We have capped the scalebar here at 100 Ohm-m to highlight the contrast between mélange and sandstone. Cross-section runs east to west, looking downslope and to the south on Oak Ridge earthflow. Location marked in Fig. 1.1d.

We measured remarkably similar resistances during the June and November electrical resistivity surveys (Fig. 1.2). In both cases, we see higher resistivities on the western half of the line (~100 Ohm-m) and resistivities one order of magnitude lower (~10 Ohm-m) on the eastern half starting at 56 meters along the cross section, which corresponds exactly to the western boundary of the landslide (identified by a seasonal strike-slip fault that forms at the base of the lateral levee during winter when landslide velocity is greatest). These numbers align with typical expected values for sandstones and shales/clays respectively (Palacky, 1987). Surface mapping indicates that the local geology consists of sandstone to the west of the landslide levee and that the active landslide body to the east of the levee is predominantly mélange (Fig. 1.1c). Between 0 and 55 meters along the survey line, we also observe a vertical transition to high resistivities occurring at about 10 meters below the surface. Higher resistivity sections at 45 m and 10 m along the survey line correspond to meta-sedimentary blocks embedded in the mélange.

Differencing the June and November surveys (Fig. 1.2c) confirms that there was little resistivity change despite the roughly 30 kPa drop in pore-fluid pressure measured during the 5-month interval (Fig. 1.4a). The changes that were measured occur mostly on the western side of the cross section (outside the landslide boundary) and are heterogeneous in sign and location. Results from both the Schlumberger and

dipole-dipole nodal configurations were similar, so for the sake of brevity only the Schlumberger results are presented here; dipole-dipole results are shown in Figure 1.10.

Our interpretation of the electrical resistivity tomography (Fig. 1.2) and geologic surface mapping (Fig. 1.1c) together suggests that the body of Oak Ridge earthflow is predominantly mélange, bounded laterally and possibly basally by sandstone. Although resistivity can be influenced by a range of factors beyond lithology (e.g., water content, fluid chemistry, or porosity), pore-fluid pressures dropped by roughly 30 kPa between the two surveys and we measured less than seven millimeters of rain, yet ERT did not display a decline in resistivity that we would expect due to lower water content. There is also little reason to expect dramatic differences in fluid chemistry across the transect, hence the striking similarity between the June and November ERT measurements lends credence to our interpretation that observed resistivity contrasts delineate lithologic contacts. Additionally, the drop in resistivity values from ~100 Ohm-m to ~ 10 Ohm-m occurs exactly at the mapped surface contact between the mélange-rich landslide body and the sandstone-rich levee on our survey transect (Fig. 1.2). This contrast appears to extend at an angle down into the subsurface to about 10 meters depth before leveling off and continuing horizontally to the east. We tentatively interpret this to be the base of the landslide (marked by the dashed line in Fig. 1.2). While this interpretation is not well-constrained, the slip surface must be deeper than 4.2 meters because we have a piezometer installed to that depth that has not been damaged by landslide

movement. Additionally, if we apply the scaling relationship developed by Handwerger et al. (2013) for earthflow thickness in the Eel River catchment, we predict that the basal depth of Oak Ridge earthflow should be deeper, ~19 m. This is calculated using the relationship $D = \alpha A^{\gamma}$, where D is earthflow depth, A is earthflow planform area (0.35 km^2), $\alpha = 0.46$, $\gamma = 0.29$, and the r^2 value of the relationship is 0.45. These constraints give us feasible upper and lower bounds on the possible landslide thickness.

The current transport zone is bounded on either side by raised sandstone outcrops which the landslide body seems to be funneling between. It is likely that the landslide originated in a band of mélange (the current source area) and began translating downslope over the adjacent band of sandstone, preventing it from laterally spreading until it reaches the relatively less confined valley bottom.

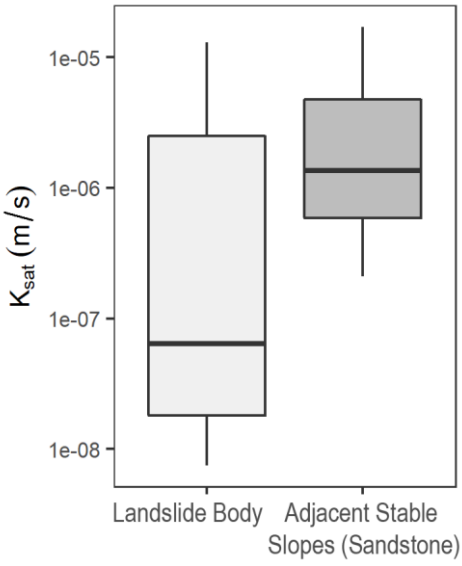

Figure 1.3 | Field-saturated hydraulic conductivity is lower on the active earthflow (left) than on the surrounding stable slopes (right) when measured by Guelph permeameter.

1.3.2 Hydraulic Conductivity

The geometric mean of the field-saturated hydraulic conductivity on the active earthflow (7.1 x 10^{-8} m/s, n=13) is significantly lower than on the adjacent stable slopes (1.7 x 10^{-6} m/s, n=6) (Fig. 1.3). The former is typical for silty soils and the latter for silty to clean sand (Freeze & Cherry, 1979).

We successfully measured hydraulic conductivity in 13 of the 14 boreholes on the earthflow. Data from the unsuccessful borehole, P4, were discarded because the water level rose steadily over the 1-hr observation period. Complete results including hydraulic conductivity values, depths, and imposed heads are listed in Table 1.1. Overall, lower head values tended to produce lower hydraulic conductivities. When possible, we account for this difference by following the standard method of averaging together the hydraulic conductivity values determined by each head measurement to get a final representative conductivity value for the borehole. The fastest measured K_{fs} on the earthflow was 1.3×10^{-5} m/s, which was anomalously high when compared to the other measurements. We attribute this unusually high conductivity to the presence of a sandy lens we encountered while augering. The lowest hydraulic conductivity was 7.5×10^{-9} m/s.

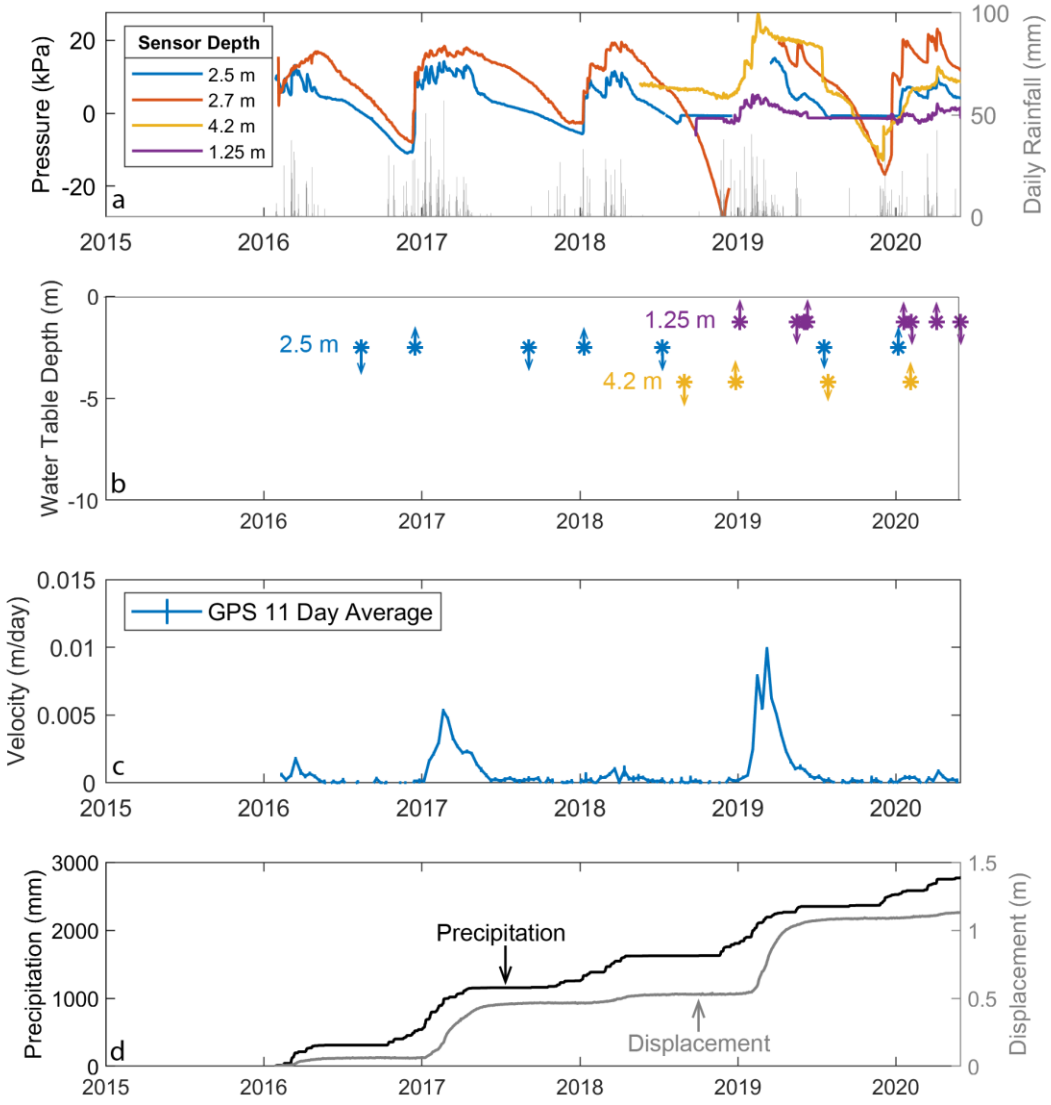

Figure 1.4 | Time series monitoring data from Oak Ridge earthflow. **(a)** Daily rainfall record and pore-fluid pressures from the four piezometers. **(b)** Instances where the three 1.25 m, 2.5 m, and 4.2 m piezometers (all located in cluster in the center of the earthflow, Fig. 1.1d) measured 0 kPa indicating the presence of the water table. Arrows indicate whether the water table was rising or falling at the time. **(c)** Velocity computed over an 11-day window from the middle GPS station (OREO). Location shown in Fig. 1.1d. **(d)** Cumulative precipitation and displacement over the monitoring period. Velocity, pore-fluid pressure, and rainfall data previously published in (Finnegan et al., 2021a).

1.3.3 Rainfall

Average annual rainfall measured on-site during the monitoring period was 640 mm, slightly higher than the 572 mm average calculated by the PRISM Climate Group for 1981–2010. Total water-year (October 1 – September 30) rainfall was 666 mm for 2016, 845 mm for 2017, 520 mm for 2018, 743 mm for 2019, and 427 mm for 2020. Cumulatively, Oak Ridge received 2,777 mm of rain during the monitoring period (Fig. 1.4).

1.3.4 Pore-water Pressure

Piezometers indicate that the pore-fluid pressures in our monitoring location roughly fluctuate between 25 kPa and -25 kPa (Fig. 1.4a). Pore pressure response to storms is minimal until a few weeks after the start of seasonal rainfall at which point there is an abrupt ~ 10 kPa rise in pressure and piezometers start to show 1–2 kPa pressure fluctuations in response to individual storms. 1D variably saturated flow modeling reveals that the abrupt seasonal increase in pressure occurs due to a rapid rise of the water table from the downward advection of a seasonal wetting front (see Finnegan et al. (2021) for a more thorough discussion of the early season infiltration dynamics).

The piezometer at 1.25 m depth recorded positive pore-fluid pressures for about 5 months in 2019 (January through June) and 2 months in 2020 (April through June) indicating the presence of an apparent water table above this depth at those times. The 2.5 m piezometer generally becomes unsaturated somewhere between June and September and remains dry through December or January. Figure 1.4b plots

times when the 1.25 m, 2.5 m. and 4.2 m piezometers measured zero kPa, indicating times when the water table was at that depth. From this we can see a rough approximation of the water table rise and fall throughout the year. Assuming hydrostatic conditions and averaging all pore-fluid pressure measurements over all the monitoring years, we find that the average apparent water table at Oak Ridge is roughly two meters beneath the surface at our monitoring location. Hydrostatic conditions are almost certainly a poor assumption because there are strong vertical hydraulic gradients that complicate the relationship between measured pore-fluid pressure and the actual water table location (Finnegan et al., 2021). However, this calculation gives us a rough approximation of the apparent hydrologic conditions. Taken together, the piezometric data indicate that Oak Ridge earthflow is frequently close to saturation during winter months.

1.3.5 Landslide Displacement

Displacement at Oak Ridge occurs exclusively during the wet season, slowing to zero during the dry summer months (Fig. 1.4c). Winter velocities are typically a few millimeters per day, reaching a peak of one cm/day during winter 2019 (the second wettest year in our monitoring record). The landslide moved 1.13 meters between 2016 and 2020 at the OREO GPS station, with the majority of movement occurring in 2017 and 2019 (Fig. 1.4d).

The seasonal onset of landslide motion coincides with the abrupt rise in pore-fluid pressure discussed above that occurs a few weeks after the first rains of the year (Fig. 1.4). Once the landslide is near saturation, it is very responsive to pore-pressure

fluctuations and acceleration usually happens within about a day of a rainfall event (Finnegan et al. 2021).

Figure 1.5 summarizes the relationship between landslide velocity and pore-fluid pressure as measured at each of the four piezometers. There is variation among the piezometers, but the relationship is clearly non-linear with a distinct pore-fluid pressure threshold required for motion to begin and an apparent cap which the pressure never exceeds despite increasing velocities. Although Figure 1.5 suggests more pressure rise is possible at each piezometer, it is important to keep in mind that the line indicating the ground-surface assumes hydrostatic conditions; the fact that there is strong vertical infiltration at Oak Ridge (Finnegan et al., 2021) means that this hydrostatic assumption almost certainly overestimates the water table height. Hence, it is likely the cap in pore pressure is much closer to the maximum pressure attained at each piezometer than is apparent from Figure 1.5. Additionally, hummocky earthflow topography can prevent the water table from perfectly mimicking the landslide surface (Iverson & Major, 1987), and slope-parallel channels on either side of our piezometers may cause lateral drainage that also influences the maximum achievable water table height. Notably, all the movement also happens in a very small range of pore pressures (approximately 10 kPa of change can shift the balance from no motion to motion) indicating that landslide motion is quite sensitive to small pore-fluid pressure fluctuations.

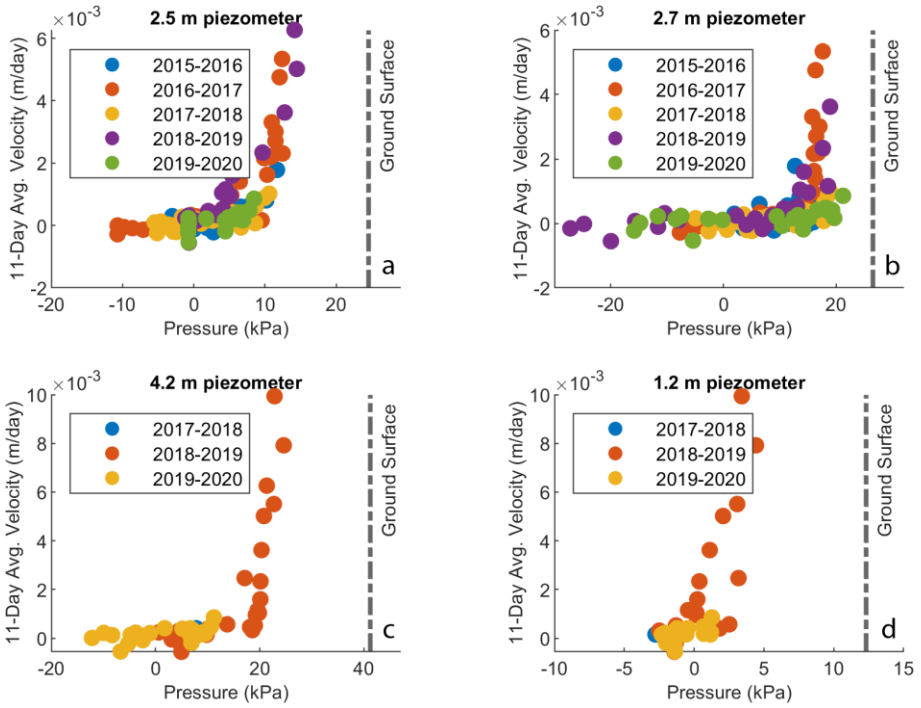

Figure 1.5 | 11-day averaged velocities of Oak Ridge earthflow plotted against median pore-fluid pressure at each piezometer for the same period. Data is color coded by water year (Oct. 1 – Sept. 30). Dashed vertical lines show the amount of pore-fluid pressure representing complete saturation between the sensor and the ground surface at each location assuming hydrostatic conditions. Note that x-axes are scaled to the range of pore-fluid pressures typical for each piezometer. The 2.7 m and 2.5 meter piezometers were offline from 12 December 2018 – 4 April 2019 and 20 December 2018 – 15 March 2019 respectively due to dead batteries, hence they did not record pore-fluid pressure during the high velocity periods of winter 2019.

1.3.6 Springs

During the winter months, Oak Ridge earthflow overflows with abundant springs, ponds, and wetlands (Fig. 1.6). The spring discharge decreases as pore-fluid pressures decrease following storms and there is usually no measurable discharge during the dry season (Fig. 1.6d), although some of the wetlands are perennial and do persist through the summer. These hydrologic features are concentrated in the active

part of the earthflow (Fig. 1.6e) and are rarely present outside of the landslide boundaries.

We recorded an average discharge of 2.36 x 10^{-2} m^3/s from the springs on 19 February 2019, and 2.40 x 10^{-3} m^3/s on 15 March 2019. When we sum the February discharge over a day and divide by the mapped area of the landslide (~247,000 m^2, Fig. 1.6f) we can compare magnitudes to typical rainfall amounts. Prior to 19 February (on which no rainfall was recorded), there were seven consecutive days of rainfall that totaled 74.3 mm. In comparison, the area-normalized spring discharge on 19 February was ~10 mm, or roughly equivalent to the average daily rainfall rate for the preceding week of moderate rainfall. This observation implies that when the landslide is near saturation, the flux of water discharged via springs is comparable to the flux of rainwater that is available to be infiltrated.

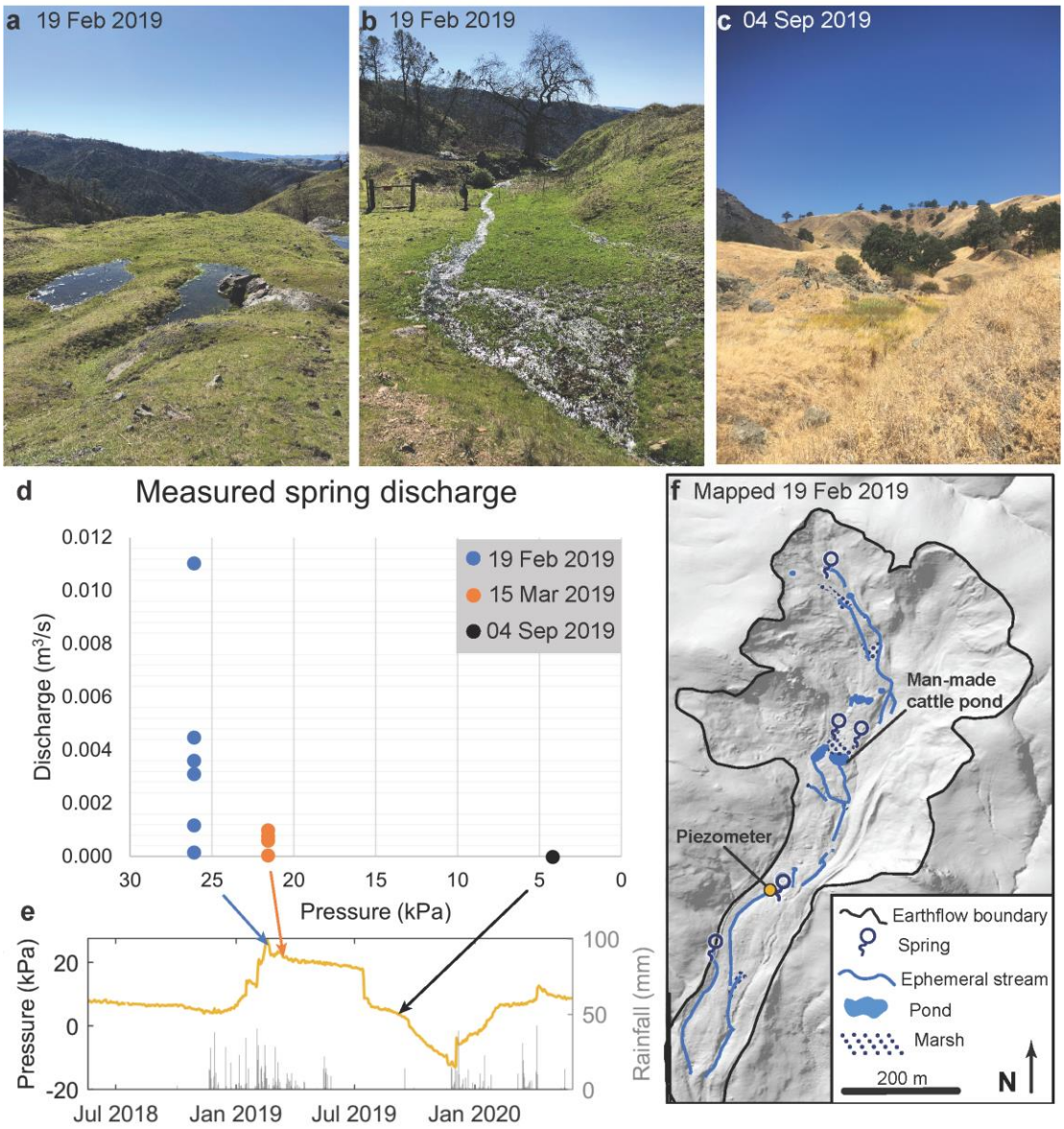

Figure 1.6 | During the rainy season Oak Ridge earthflow hosts abundant ponds and springs **(a and b).** These disappear during the hot, dry summer with exception of a few perennial wetlands **(c).** Spring discharge generally decreases as pore pressure decreases **(d and e)**. Data from the 4.2 meter piezometer shown here. **(f)** Locations of springs, streams, and other hydrologic features mapped on the earthflow. Piezometer location marked by yellow circle. All hydrologic features mapped here are natural, with the exception of a man-made cattle pond which was built up in a natural topographic depression and is unlined, so the water levels reflect the general conditions of the landslide water table.

1.4 Discussion

Field data from Oak Ridge earthflow indicate the landslide is quite sensitive to precipitation inputs after it reaches a sufficient saturation threshold, generally responding within a day to rainfall events (Finnegan et al., 2021). We observed a clear non-linear relationship between measured pore-fluid pressure and landslide velocity (Fig. 1.5). We see a distinct pore pressure threshold in this relationship that must be reached for motion to begin and an apparent cap on the system setting a maximum pore pressure that can be achieved. Similar tight and nonlinear coupling between piezometric records and landslide displacement has been observed at slow-moving landslides in Spain and France (Corominas et al., 2005; Malet et al., 2002). At Oak Ridge, the fastest and slowest recorded velocities correspond with only a 10 kPa pressure difference.

Through our field monitoring, we also found that the water table within Oak Ridge earthflow remains within a few meters of the surface year-round and that during the wettest times of the year it is shallower than ~1 m from surface. When the water table approaches the surface, excess water is shed via springs (and likely saturation overland flow, although we did not directly observe this). Hydraulic conductivity in the mélange matrix material that dominates the landslide body is fairly low, $\sim 10^{-8}$ m/s. In contrast, the sandstone outcrops and soils bounding the landslide have no observed springs and the soils have an order of magnitude higher hydraulic conductivity. We have never been able to auger to the water table despite

augering during the wettest times of the year down to 4 meters (the depth of our deepest piezometer on the earthflow) at the same elevation as the landslide body.

Taken together, these observations paint a picture of a clay-rich, frequently saturated, poorly draining landslide teetering back and forth just on the brink of movement for roughly half the year. Although we do not know precisely the processes that start or stop movement of the landslide, the apparent cap on possible pore pressures and the contrasting hydrologic behavior of the mélange and the sandstone suggest that material-specific hydrologic and mechanical properties may play an important role.

Stepping back, in the simplest form, hillslope stability will depend on the balance between destabilizing slope-parallel shear stresses and stabilizing slope-normal stresses. For landslides that are forced hydrologically (as opposed to seismically, e.g., (Jibson, 2007), the balance shifts toward slope movement when pore pressures increase, lowering the effective normal stress. This stress balance is commonly modeled through the Mohr-Coulomb equation (Terzaghi, 1943):

$$\tau = (\sigma - p)tan\varphi + c \qquad (1)$$

Where τ is shear stress, σ is normal stress, p is pore pressure, φ is friction angle, and c is effective cohesion. Superficially, this simple link between pore pressure and effective normal stress is well understood, yet the details of how exactly this relationship manifests, and what velocity patterns will result once movement occurs,

remain elusive. We can divide the problem into two different stages: 1) How does driving stress increase relative to shear strength (i.e. the relationship between precipitation and subsurface pore-fluid pressure), and 2) How will the landslide move in response to changing pore-fluid pressure (i.e. the relationship between stress and strain)?

In the following sections, we use our case study at Oak Ridge earthflow to explore how the material-specific hydrologic properties impact the these two questions. We explore how lithologically-controlled weathering patterns mediate the relationship between precipitation and subsurface pore pressure in landslides and the implications of this relationship for landslide movement in response to weather patterns across California. We also briefly summarize some of the existing work on the relationship between stress and strain in landslides and discuss how Oak Ridge can provide insight into this complicated problem.

1.4.1 Weathering, Pore-fluid Pressure, and Stress

A geomorphologist's conceptual model for a hillslope consists of regolith (rock weathered to any degree) above unweathered bedrock. The regolith layer can be further divided into a top layer of mobile regoglith (soil) underlain by immobile regolith, consisting of saprolite and weathered rock. Saprolite is a specific category of weathered rock that has been broken up to the point that it can be dug through with a shovel but still retains the original rock structure (Anderson & Anderson, 2010). Within these layers, the variably saturated (vadose) zone generally extends through the soil mantle and the weathered bedrock, meeting the groundwater table at the top

of fresh, unweathered bedrock, where reduced porosity and hydraulic conductivity significantly slow drainage. Seasonal fluctuations and water table rises typically occur within the weathered zone (Lebedeva & Brantley, 2013; Pedrazas et al., 2021; Rempe & Dietrich, 2014). (Notably, although the increase in conductivity with weathering is generally true in sedimentary and metamorphic settings, the opposite may actually be true in volcanic settings, where extremely high initial conductivity often decreases as rock weathers because the primary minerals turn into clays (e.g., Schopka & Derry, 2012). Recent research shows that there are predictable, lithologically controlled bedrock weathering patterns across landscapes (Riebe et al., 2017). Considerable research efforts have been directed towards quantifying these patterns in recent years, particularly as part of the U.S.-based, NSF-funded Critical Zone Observatories program and its successor the Critical Zone Collaborative Network (Callahan et al., 2020; Flinchum et al., 2018; Hahm et al., 2019; Holbrook et al., 2014; Leone et al., 2020; Moravec et al., 2020; Pedrazas et al., 2021).

As part of this effort to quantify critical zone processes, Hahm et al. (2019) documented a thin weathered zone in the Franciscan mélange at Sagehorn-Russell Ranch ("Sagehorn") in the Northern California Coast Ranges (location mapped in Fig. 1.1a). Through hydrological monitoring and material characterization of recovered cores, they found that the weathered zone of the argillite-matrix mélange extends ~ 3 m into the subsurface. Below this lies clay-rich, unweathered mélange matrix which essentially cannot drain due to its low permeability. This thin weathered zone limits storage capacity and causes excess rain to be shed via shallow storm and

saturation overland flow. In contrast to the mélange matrix, Hahm et al. (2019) document a deep weathered zone of ~30 m at the ridge of a nearby site (Angelo Coast Range Reserve) underlain by argillite and sandstone in a similar climate. This deeply weathered profile allows ample storage. Although it is unclear exactly what determines the depth of weathering in these two landscapes, it is clear that the two different lithologies have substanstial differences in subsurface structure that manifest in dramatically different hydrologic regimes. The water table at Sagehorn typically resides two to four meters below the ground surface, which is strikingly similar to what we see at Oak Ridge and what has been observed at the Minor Creek (Iverson & Major, 1987a) and Two Towers (Schulz et al., 2018) earthflows, both also located in Franciscan mélange (locations mapped in Fig. 1.1a).

The limited storage capacity that results from a thin weathered zone has important implications for the ability of hydrologically-forced landslides in the Franciscan mélange to increase stress. As precipitation infiltrates into the subsurface, there is a finite amount of space that can be filled above the initial water table (i.e. the unsaturated zone), beyond which excess water will spill out as springs and saturation overland flow. Because the pore pressure acting on the failure plane is directly linked to the height of the water table above the failure surface (e.g., Finnegan et al., 2021), the range of possible stresses will depend on the amount of water that can build up above the failure plane and may or may not be enough to instigate landslide movement. An exception to this would be the occasional case of undrained loading, e.g. a debris flow occurring on top of an existing landslide (Booth et al., 2018).

This framework suggests that the mechanics of landslide movement are fundamentally mediated by weathering patterns because the pore pressure that can build up on a failure plane is linked to the thickness of the unsaturated zone. At Oak Ridge and similar sites in the Franciscan mélange (e.g., Minor Creek and Two Towers earthflows), the thin weathered zone (~ 3 m) that develops above low permeability, undrained bedrock means that the height of the water table is significant relative to landslide depth (which is > 3 m for most slow-moving landslides, LaCroix et al., 2020) and hence the landslide body may saturate after relatively little rainfall. However, once the water table reaches the landslide surface, pore-fluid pressures will be limited by the available space and excess water will spill out in the form of saturation overland flow and springs until the water table recedes. In contrast, a region that hosts a thick weathered zone, for example a sandstone or mudstone dominated landscape, may maintain a much deeper water table and experience much larger annual fluctuations (see the description of the Angelo Coast Range Reserve site by Hahm et al. [2019] for an example and Fig. 1.7 for a conceptual illustration). Landslides in these settings, therefore, have the potential to build up significantly more stress above the failure place before the water table reaches the surface. In this way, weathering patterns across a landscape may significantly influence landslide behavior by controlling the magnitude of water table rise relative to landslide depth achievable in the subsurface. A full test of this hypothesis would require datasets of bedrock weathering patterns across many different lithologies coupled with

observations of vadose zone dynamics and landslide movement in sites with range of weathered profile thicknesses.

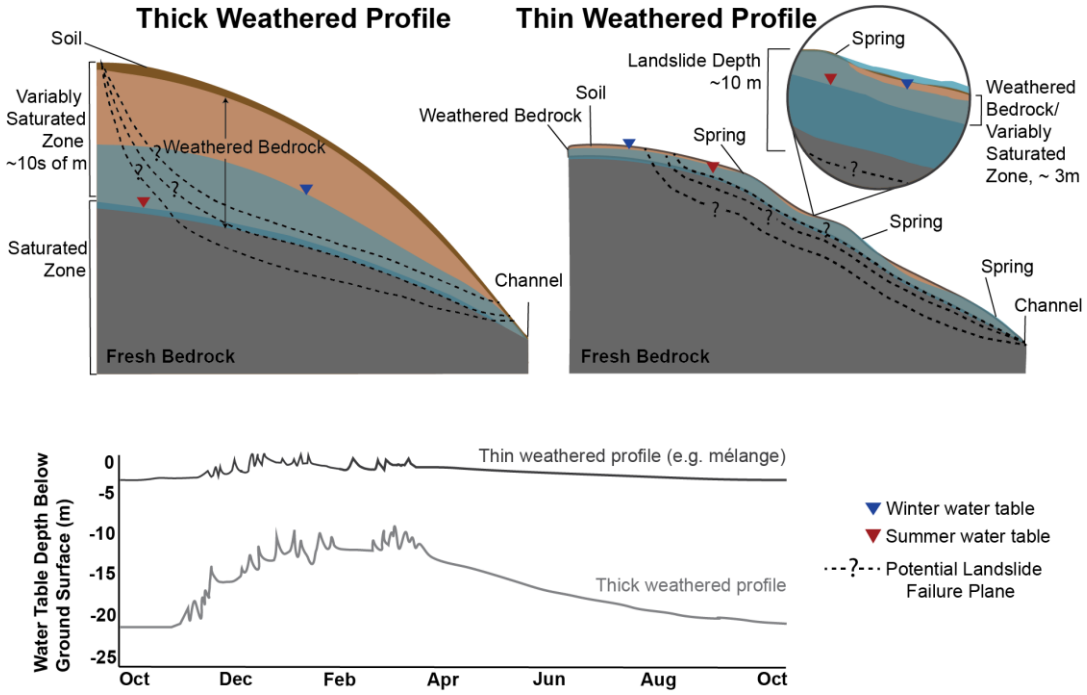

Figure 1.7 | Conceptual hillslope cross sections illustrating the contrasting structure and hydrology of a thick weathered profile (left) and a thin weathered profile (right). The graph below compares how water tables in the two hillslopes would likely evolve over the course of a year in response to precipitation in a Mediterranean climate (cool, wet winters and hot, dry summers). The water table in a region with a thick weathered profile rarely reaches the surface but does vary by many meters annually, causing large fluctuations in stress over a potential landslide failure plane. In contrast, a region with a thin weathered profile such as the Franciscan mélange sees a variation of around three meters or less. During winter, the water table often saturates to the ground surface and spills out excess water via saturation overland flow during storms and via springs afterward, which persist due to the combination of elevated water levels and rumpled topography. Hillslope cross sections inspired by Figure 5 of Hahm et al. (2019). Figure not to scale.

1.4.2 Comparing Landslide Behavior Along a Precipitation Gradient

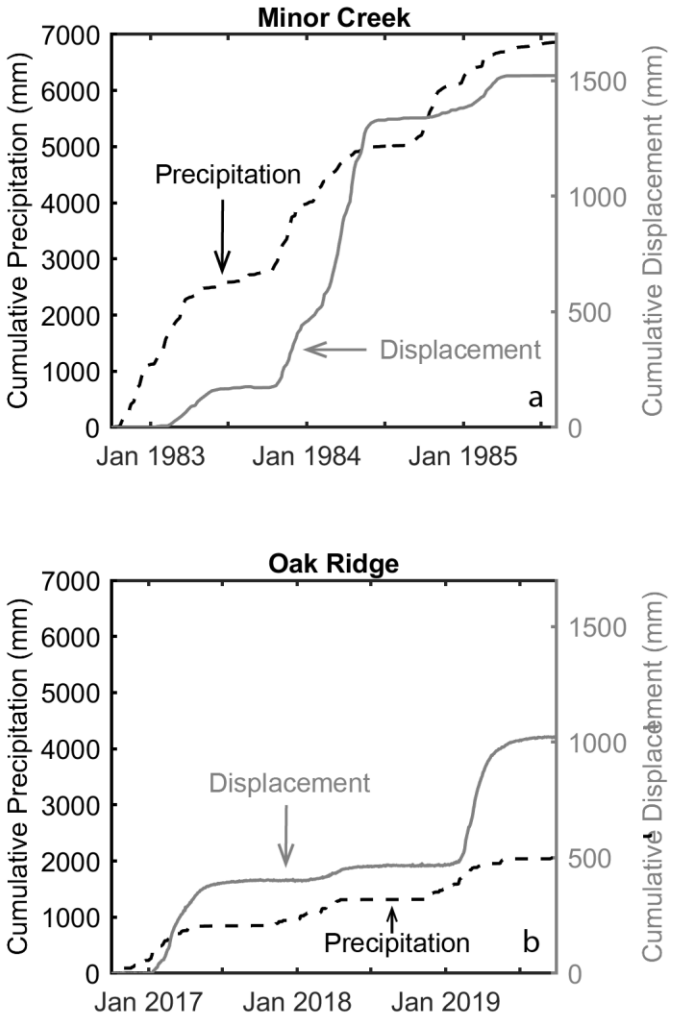

Figure 1.8 | Cumulative precipitation and displacement at **(a)** Minor Creek earthflow October 1982 – September 1985 and **(b)** Oak Ridge earthflow October 2016 – September 2019. Minor Creek received over three times the amount of precipitation Oak Ridge did over a three-year period, yet it only moved 0.5 meters more. Minor Creek data digitized from Iverson and Major (1987).

Lithologically controlled bedrock weathering patterns that constrain the timing and magnitude of stress buildup at a landslide failure plane could also explain why earthflows in California behave remarkably similarly across a dramatic climate gradient. Minor Creek earthflow, located in Humboldt County in the far north-west corner of California, receives more than three times the annual precipitation that Oak Ridge does (Fig. 1.1), yet the displacement patterns between the two are strikingly similar (Fig. 1.8). During a three-year period from October 1982 to October 1985, Minor Creek received nearly 7000 mm of precipitation that caused 1.5 meters of displacement, whereas Oak Ridge moved 1 meter on 2000 mm of precipitation that fell between

October 2016 and October 2019. Based on the average water table heights for the two landslides, both have a limited storage capacity which, when exceeded, will cause excess water to spill out as springs and overland flow rather than continuing to drive landslide movement. This implies that landslides in Franciscan mélange should all have a similar capacity for movement regardless of where they fall on the north-south precipitation gradient that spans the state (Fig. 1.1a and 1.1b). This capacity may not always be met: during a drought year, a landslide in the drier regions may not receive enough rain to start or sustain movement. This was the case, for example, between 2012 and 2015 when earthflow velocities across northern California reached historical lows due to the prolonged drought (Bennett et al., 2016b). On the other end of the spectrum, the extreme rainfall that California received in 2017 triggered a wide-spread, short-lived increase in both activity and velocity of landslides (Handwerger, Fielding, et al., 2019). In this case, assuming a landslide in the wet regions and a landslide in the dry regions both receive sufficient precipitation to fill storage, we would predict that the excess water a landslide in a wetter region receives will have no effect on the landslide's speed or displacement. Instead, lithologic continuity across a climate gradient will moderate precipitation variability in areas dominated by mélange and similar rock types. This explains why Handwerger et al., (2019) did not observe a clear relationship between spatial gradients in rainfall and the ratio of water year 2016 to water year 2017 landslide velocities as part of their survey of northern California earthflows. This potential moderation of precipitation variability by subsurface storage limitations will be increasingly important as

California's precipitation regime shifts to increasing variability in future years (Swain et al., 2018).

1.4.3 Landslide Movement in Response to Stress Changes

Once rising pore pressure increases the driving shear stresses in a landslide relative to its shear strength, the second major conundrum for predicting landslide motion is how the landslide will move in response to the stress change. The exact constitutive relationship needed to predict this remains elusive. Quantitative models of landslide velocity typically try to explain only one style of movement (Baum & Johnson, 1993; Denlinger & Iverson, 2001; Hungr, 1995; Schulz et al., 2018), however a few recent studies have proposed mechanistic frameworks that cover the spectrum of observed speeds. The most prominent work in this area builds on the critical-state soil-mechanics framework to explain a diversity of landslide motion through pore pressure feedbacks and associated dilation or contraction of basal shear zones (Iverson, 2005). Alternatively, researchers have drawn from the development of rate-and-state friction theory in fault mechanics literature to suggest that slow landslide motion occurs when friction increases with either velocity or slip and that fast landslide motion occurs when friction decreases with increasing velocity or slip (Handwerger et al., 2016; Helmstetter et al., 2004; Scaringi et al., 2018). Building on a rate- and state-dependent frictional model, Handwerger et al. (2016) further proposed a framework in which dynamic rupture (and therefore landslide acceleration) is suppressed in slow landslides when slip occurs over a smaller area than the critical nucleation length given reasonable assumptions about stiffness,

friction, and pore fluid pressure. Other researchers have proposed threshold-based models wherein landslides creep until a yield stress or gradient is reached, after which movement is governed by either rate-and-state friction (Petley et al., 2017) or a dense granular flow rheology (Ferdowsi et al., 2018).

While one or more of these mechanisms are likely integral to setting the velocity at Oak Ridge earthflow, our monitoring data are currently insufficient to distinguish between them, thus we cannot entirely predict the details of landslide movement. However, our observed relationship between velocity and pore-fluid pressure may allow some broad constraints and insights on movement of the earthflow in response to stress changes. At Oak Ridge, we observe a distinct non-linear relationship between landslide velocity and pore-fluid pressure (Fig. 1.5), as has been observed at other slow-moving landslides (Corominas et al., 2005b; Malet et al., 2002). Extrapolating this relationship suggests that if pore-fluid pressures were able to increase above the level at which the thin vadose zone appears to restrict them at Oak Ridge, then much faster velocities could be reached that could potentially lead to runaway acceleration. However, within the relatively small range of pore-fluid pressures that we have observed corresponding with landslide movement (~10 kPa), we have only measured slow, creeping motion (~ 1 cm/day at the fastest). Given how close to the surface the water table at Oak Ridge is during the winter months, it is hard to build up significantly more stress than this. An increase of 2 m of the water table—which would saturate the roughly 2 m vadose zone at Oak Ridge—represents at most (assuming hydrostatic pressure) an ~18 kPa pressure change. However, the

relatively low friction angle (θ) of Oak Ridge earthflow (12–14 degrees) (Nereson et al., 2018) means that an 18 kPa change in pressure is equivalent to only a ~ 4 kPa drop in shear strength according to equation 1. Importantly, even this modest loss of shear strength can cause movement, as we have observed, yet the subsurface storage capacity constraints suggest that it is hard, although perhaps not impossible, to build sufficient stress to cause runaway acceleration of the landslide.

Regulation of pore pressures via a thin vadose zone could also potentially occur in other clay-rich lithologies that tend to host slow-moving landslides. For example, the Slumgullion landslide in Colorado, USA, occurs in clay-rich weathered volcanic rocks and maintains a water table one to two meters below the ground surface that typically varies by one meter or less over the year (Schulz, McKenna, et al., 2009). Indeed, Coe et al. (2003) have previously theorized that high pore pressures at Slumgullion might be equilibrated through a network of springs. Notably, Slumgullion (20×10^6 m^3, average 20 m thick) moves in association with atmospheric tides that have an amplitude of ~0.5 kPa (Schulz, Kean, et al., 2009). Together, Oak Ridge and Slumgullion demonstrate that very little change in stress is required to trigger earthflow motion, however, as we have illustrated at Oak Ridge, lithologically imposed constraints may provide an important limit to more rapid movement.

Although there is currently no widely accepted theory for creep in landslides, laboratory experiments show that creep can be a precursor to rapid failure. For example, experiments demonstrate that modest short-term variations in pore-fluid pressure (~ 20-100 kPa) can cause pulses of acceleration that are then attenuated by

shear zone dilation (Agliardi et al., 2020; Carey et al., 2019), as proposed in the theoretical model of Iverson (2005) and potentially observed in the field by (Schulz, McKenna, et al., 2009). Agliardi et al. classify this phase of movement as the Creep I regime. As the experiments continue, repeated pore pressure steps push the material closer to the Mohr-Coulomb failure envelope, eventually driving it through all three phases of creep into catastrophic failure, as also shown in Moore and Iverson's (Moore & Iverson, 2002) experiments on till. Complementing this work, computational experiments by (Damsgaard et al., 2016) on ice flow dynamics have revealed that rate-dependent creeping motion arises when load-bearing force chains in granular sediments rearrange in response to cyclic variations in pore-water pressure (similar in magnitude, ~ 100 kPa, to the laboratory experiments above) that change the orientation of the maximum compressive stress. Similarly, subduction-zone studies have linked episodic tremor and slip to creeping motion associated with modest increases in pore fluid pressure (Bürgmann, 2018). This modeling provides a potential mechanistic link between small variations in pore pressure and creep in granular materials, such as landslides like Oak Ridge earthflow. However, to the extent that creep represents a precursor to catastrophic failure, a limited capacity to increase pore pressure may effectively throttle landslide acceleration by restricting deformation to the Creep I regime articulated by Agliardi et al. (2020); the pore pressure changes that we have observed in the field are typically an order of magnitude less than what laboratory experiments require to produce catastrophic failure.

Importantly, this simplified framework, in which lithologically controlled weathering patterns bound the range of potential stress buildup in a landslide and thus indirectly influence subsequent landslide movement, cannot explain the full complexity of observed landslide behaviors. For example, it would not explain the behavior of shallow, partially saturated landslides that are strongly influenced by suction stresses (Godt et al., 2009) or landslides that exhibit significant evolution of material behavior, such as debris flows (Iverson, 1997). Additionally, it does not account for surging behavior that has been observed in earthflows (e.g., Keefer & Johnson, 1983), which likely occurs due to mechanical processes about which we remain agnostic. Ultimately, the linkage between the Franciscan mélange and its propensity for creep arises from some combination of its hydrology, as we have focused on here through our case study at Oak Ridge earthflow, and its mechanical behavior (e.g., propensity for dilation or velocity-strengthening properties). The relative importance of these two components is unclear, and it is possible that the role of hydrology is essentially negligible. For example, clay rich fault gouges commonly exhibit velocity strengthening behavior (Ikari et al., 2009), which could explain creep without appealing to hydrological forcing. That said, there are many examples of catastrophic landslides that occur in clay, particularly where relatively permeable sands are deposited over impermeable clay layers (e.g., Perkins et al., 2017). One distinguishing characteristic of this and other examples of settings where clay is interbedded with more permeable layers is the potential for pore fluid pressures to increase by magnitudes that are not possible at a setting like Oak Ridge where pore

pressure rise is suppressed via springs and saturation overland flow as the water table reaches the surface. Additionally, the catastrophic Mud Creek landslide in California did occur in Franciscan mélange, demonstrating that creep is not intrinsic to the Franciscan mélange (Handwerger, Huang, et al., 2019). Notably, Mud Creek is in a setting where thick colluvium caps the mélange (Warrick et al., 2019), which could allow for an anomalously deep water table to develop in contrast to many mélange settings. In sum, although we cannot discount the possibility that the mechanical properties of the Franciscan mélange account mostly or entirely for its creeping behavior, we can demonstrate that its capacity to change pore pressure (and hence effective stress) is severely limited by its unique hydrology. This clearly affects the climate sensitivity of earthflows in Franciscan mélange and, to the extent that effective stress and landslide velocity are linked, plausibly impacts the potential for landslides in Franciscan mélange (and possibly other similar settings) to accelerate catastrophically.

1.5 Conclusions

The predominant type of landslide movement in a given landscape depends on the structure and properties of the subsurface and the magnitude and intensity of the forcing agent (either hydrological or seismic). Earthflows are prevalent in the Franciscan mélange that covers much of the California Coast Ranges and appear in many similar mechanically weak, clay-rich materials. Here we argue that the thin weathered zone developed in Franciscan mélange caps the total subsurface stress change achievable through hydrologic forcing alone. Four years of monitoring at Oak

Ridge earthflow found a thin weathered zone that is comparable to other reported mélange sites, and we see a distinctly non-linear relationship between landslide velocity and pore pressure capped by an apparent pressure threshold. A naturally high water table means that Oak Ridge earthflow is close to movement throughout the wet, winter months, but decreases in effective normal stress (and hence shear strength) are suppressed because there is limited dynamic storage capacity. This appears to be enough to just start the initial phases of creep. We do not have sufficient constraints on the mechanical properties to test the many constitutive relationships that have been proposed to govern landslide movement and thus cannot reliably predict the full behavior the landslide. However, we theorize that excess pore pressure beyond the limited storage capacity is released through saturation overland flow and springs, influencing landslide velocity by preventing the buildup of additional stress in the system. In this way, the springs at our field site may act as a pressure release valve and throttle rapid movement of our earthflow even as the hydrologic properties dictated by the weathered profile and the inherent weakness of the Franciscan mélange combine to persistently keep the landscape on the brink of failure. This limited storage capacity could explain the remarkably similar movement patterns observed between Minor Creek and Oak Ridge earthflows, despite Minor Creek receiving over three times as much rain annually as Oak Ridge. Our analysis suggests that, across climates, subsurface structure developed via weathering can dampen the effects of precipitation variability. Additionally, for a given climate, we suggest that

the weathering patterns associated with different lithologies may influence where particular styles of landsliding occur.

1.6 Acknowledgements and Data Availability

We thank UNAVCO for support with GPS installation and the San Francisco Public Utility Commission and Russ Fields for granting access to the field site. In addition, we are grateful to Em Schnorr, Alexander Nereson, and the numerous undergraduate and graduate student field volunteers who assisted in aspects of the work presented here. Funding for this work was provided through the Geomorphology and Land-use Dynamics Program of the National Science Foundation (EAR # 1658800 & EAR #1613122 to NJF). Funding for FKJO was provided by the USGS Pacific Coastal and Marine Science Center. Any use of trade, firm, or product names is for descriptive purposes only and does not imply endorsement by the U.S. Government.

Data: GPS data used in this paper are archived by UNAVCO (https://www.unavco.org/instrumentation/networks/status/nota/overview/OREO) and post processed GPS data are archived at University of Nevada Reno Geodesy Laboratory (http://geodesy.unr.edu/NGLStationPages/stations/OREO.sta) (Blewitt et al., 2018). Pore-water pressure, meterological, ERT, hydraulic conductivity, and spring data are archived by Hydroshare on the Oak Ridge Earthflow Observatory Data page (https://www.hydroshare.org/resource/8e024d2aeb22489c92dbf0c2a1db4608/)

(Finnegan, 2020). Lidar data can be downloaded from OpenTopography (http://www.opentopography.org). Lidar data acquisition and processing completed by the National Center for Airborne Laser Mapping (NCALM) as part of a seed grant to CRM (Murphy, 2019). NCALM funding provided by NSF's Division of Earth Sciences, Instrumentation and Facilities Program. EAR-1830734.

1.7 Supplemental Material

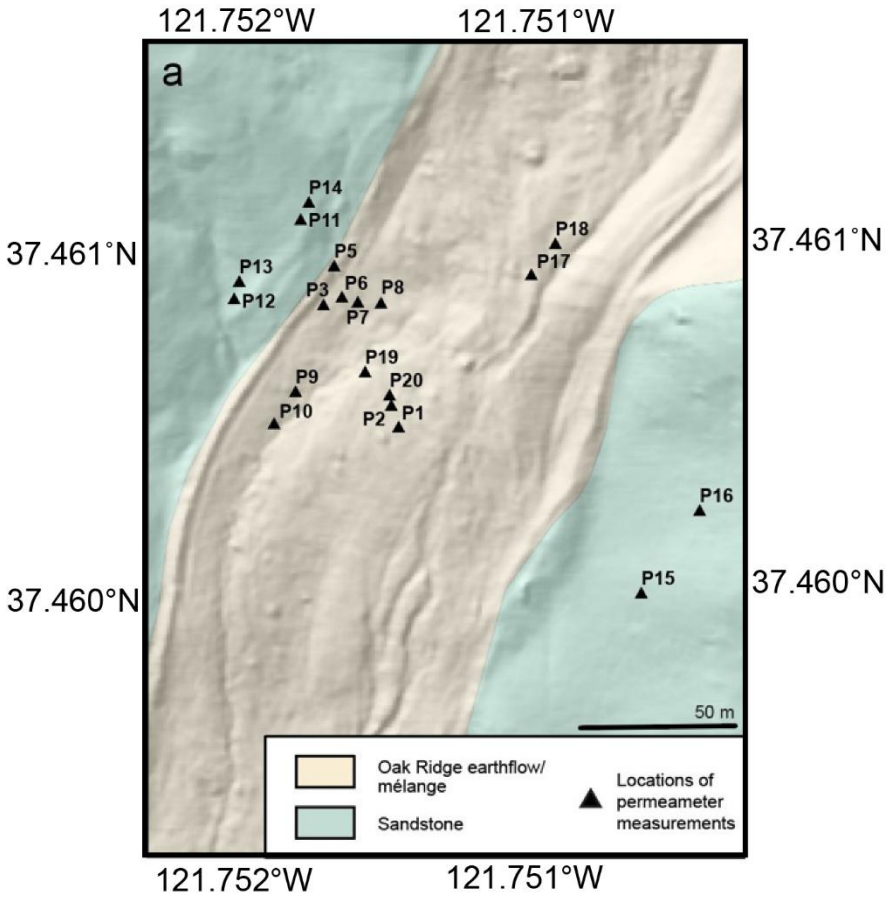

Figure 1.9 | Locations of Guelph permeameter measurements. Background is a hillshade map of Oak Ridge earthflow's transport zone where most of the monitoring equipment is concentrated. Extent mapped is shown by the blue box in Figure 1.1c.

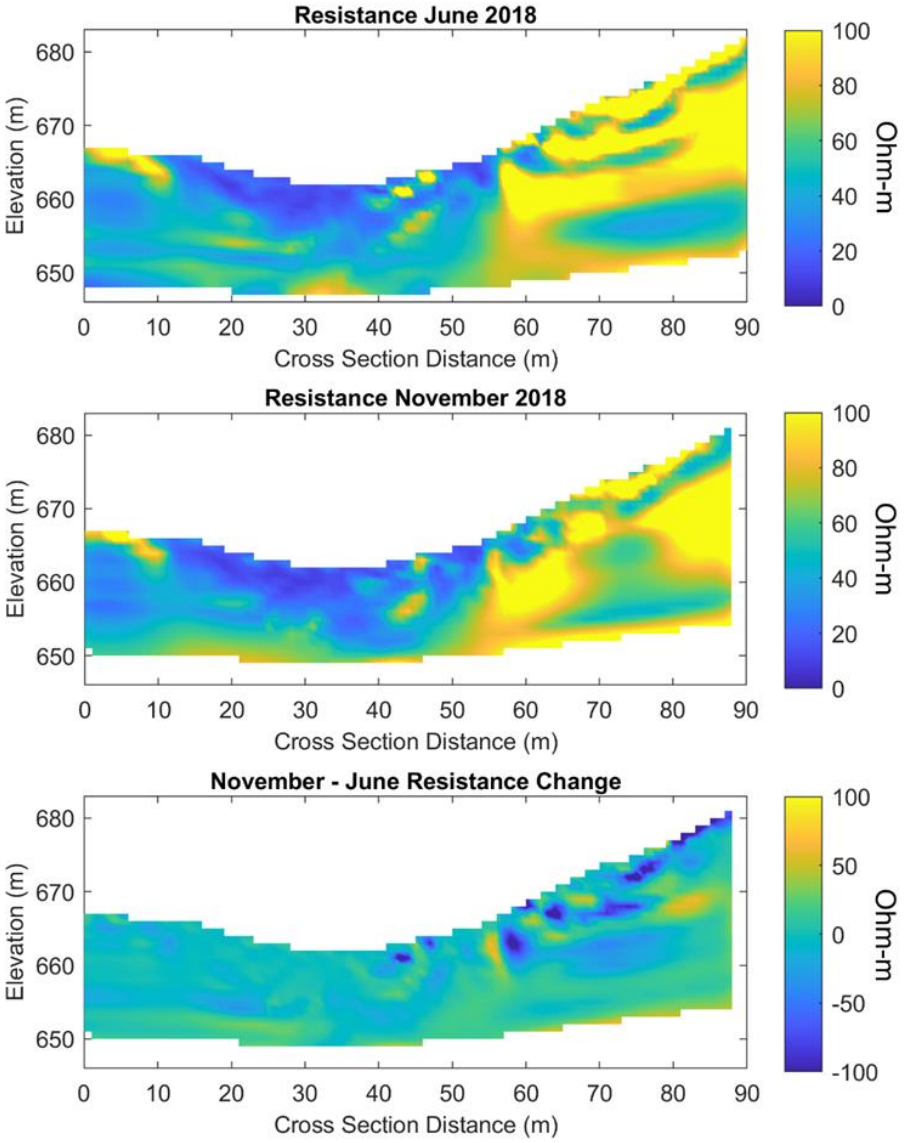

Figure 1.10 | Results of the June 2018 **(a)** and November 2018 **(b)** dipole-dipole electrical resistivity surveys and the difference between the two **(c).** Units are Ohm-m. We have capped the scalebar here at 100 Ohm-m to highlight the contrast between mélange and sandstone. Cross section runs east to west, looking downslope and to the south on Oak Ridge earthflow. Location of the survey line is indicated by the blue line in Figure 1.1d.

Depths, imposed head values, and hydraulic conductivities for Guelph permeameter measurements

Borehole ID	***Depth (cm)***	***Head (cm)***	***K_{fs} (m/s)***
On the active landslide			
P1	50	5	1.3×10^{-5}
P2	49	5, 10	$7.3 \times 10^{-8\dagger}$
P3	64	5, 10	$9.8 \times 10^{-9\dagger}$
P5	38.1	5, 10	$1.1 \times 10^{-8\dagger}$
P6	45.72	5, 10	$7.5 \times 10^{-9\dagger}$
P7	43.18	5, 10	$2.2 \times 10^{-8\dagger}$
P8	43.18	5, 10	$6.4 \times 10^{-8*\dagger}$
P9	45	5	$2.1 \times 10^{-8*}$
P10	45	5	$1.8 \times 10^{-8*}$
P17	45	15	2.8×10^{-6}
P18	30	10	$3.8 \times 10^{-6*}$
P19	45	15	1.4×10^{-6}
P20	45	15	2.5×10^{-6}
Stable soil, weathered from surrounding sandstone blocks			
P11	27	5	2.1×10^{-7}
P12	45	5, 10	$8.4 \times 10^{-7\dagger}$
P13	45	5, 10	$5.2 \times 10^{-7\dagger}$
P14	45	5, 10	$2.2 \times 10^{-6\dagger}$
P15	45	5, 10	$6.2 \times 10^{-6\dagger}$
P16	45	5, 10	$1.7 \times 10^{-5\dagger}$
Geometric mean K_{fs} on the landslide (n=13 boreholes): $7.1 \times 10^{-8}\ m/s$			
Geometric mean K_{fs} on the sandstone (n=6 boreholes): $1.7 \times 10^{-6}\ m/s$			

* The rate of water level change continued to trend down at the conclusion of the test, indicating that a steady-state flow rate had not been reached. Consequently, these K_{fs} values are likely overestimates.

† Final K_{fs} value was determined by averaging together the individual K_{fs} values from the 5 cm head measurements and the 10 cm head measurements

Table 1.1 | K_{fs} values, depth, and imposed head for each borehole. Corresponding locations for each borehole are plotted in Figure 1.9.

Chapter 2: Sensitivity of Slow Landslide Displacement to Interannual Precipitation Variability Driven by Climate Change

Abstract

Precipitation drives slow-landslide movement, however nonlinear relationships between rainfall, pore-water pressure, and landslide displacement make it challenging to predict how landslides will respond to increasing rainfall variability as precipitation intensifies due to climate change. Here we use downscaled climate model projections to simulate variably saturated groundwater conditions over 150 years for a reference landslide in central California, USA. We then link our hydrological model to an empirical model of landslide displacement to explore how multiyear precipitation variability will affect future landslide movement. We find that increasing precipitation variability leads to a decrease in landslide movement over time. The cumulative impact of extremely wet years is less than that of dry years due to limited subsurface storage capacity within the landslide relative to winter rainfall, illustrating the importance of interannual memory. Observations of landslide activity across California in response to recent precipitation extremes corroborate the impact of interannual memory on patterns of landslide movement.

2.1 Introduction

Global landslide hazards are expected to increase in the future as the frequency and magnitude of precipitation shifts in response to anthropogenic climate change (e.g., Coe, 2020; Haque et al., 2019; Kirschbaum et al., 2020; Leshchinsky et

al., 2017; Oakley, 2021). Several recent studies in the western United States have already identified climate-driven changes to slope stability over the last 50 years (East & Sankey, 2020 and references therein). As Earth's climate warms over the coming century, the likelihood of extreme, intense rainfall is expected to increase in many regions, as is severe, prolonged drought (e.g., Cook et al., 2015; Overpeck & Udall, 2010; Swain et al., 2018). This may have profound impacts for the United States, where most landslides are triggered by precipitation (Coe, 2016). However, predicting how landslide behavior will change in response to increasing precipitation variability is challenging due to the nonlinear relationships between rainfall, pore-water pressure, and landslide displacement (e.g., Carey et al., 2019; Malet et al., 2002; Murphy et al., 2022).

The response of individual landslides to climate change will depend on the frequency, duration, and intensity of precipitation and the structure, geometry, and hydraulic properties of the landslide in question (e.g., van Asch et al., 1999). Shallow landslides and debris flows are sensitive to the intensity and duration of individual storms (Iverson, 2000), thus we may expect the frequency of these events to increase in the future due to increasing precipitation intensity (e.g., Chiang & Chang, 2011; Crozier, 2010; Jakob & Lambert, 2009). In contrast, large, deep-seated (>3 m thickness), slow-moving landslides have been shown to respond to multi-year patterns in precipitation (e.g., Bennett et al., 2016b; Coe, 2012; Handwerger et al., 2022; Iverson & Major, 1987b; Malet et al., 2002; Nereson & Finnegan, 2018). Seasonally, they may respond anywhere from days (Baum & Reid, 1995) to months

(Iverson & Major, 1987) to precipitation input depending on the saturation state and rainfall history (Finnegan et al., 2021).

Already over the past decade, parts of California has experienced a historic drought (2012-2016) and the second wettest year on record (2017) (Griffin & Anchukaitis, 2014; Robeson, 2015; Swain et al., 2018). During the drought, slow-moving landslide velocities in the northern California Coast Ranges decelerated to a 70-year minimum (Bennett et al., 2016). During the extremely wet years of 2017 and 2019, landslides accelerated widely throughout the Coast Ranges (Handwerger, Fielding, et al., 2019; Handwerger et al., 2022). Over the coming century, precipitation in California is expected to become more extreme as the frequency of wet years, dry years, and whiplash years (extremely dry years immediately followed by extremely wet years) all increase (Swain et al., 2018). As both wet and dry conditions increase, it is challenging to predict what their cumulative effect will be on the movement of deep-seated landslides.

Here we explore the question of how deep-seated landslides will respond to an increase in precipitation variability. To do this, we capitalize on recent work at Oak Ridge earthflow in the Diablo Range of California, USA, where detailed pore-water pressure records combined with variably saturated groundwater flow modeling have illuminated how rainfall infiltration through dry ground at the start of California's wet season influences the timing and magnitude of the piezometric response to rainfall and hence the onset of landslide motion (Finnegan et al., 2021). At the same time, precise measurements of landslide deformation at Oak Ridge using continuous GPS

stations reveal a consistent relationship from year to year between pore-water pressure and landslide velocity (Murphy et al., 2022). Taken together, these discoveries enable accurate empirical modeling of the response of landslide displacement to seasonal rainfall delivery that allows us to use Oak Ridge as a reference site for exploring how climate change will alter slow landslide behavior. To accomplish this, we couple modeled rainfall (representing both past and future conditions) to a 1D variably saturated groundwater flow model of Oak Ridge. This groundwater flow model is then used to predict pore-water pressure at Oak Ridge earthflow, which in turn produces a daily time series of landslide displacement from 1950 out to 2100 through an empirical model linking pore-water pressure and landslide displacement. This allows us to forecast, in particular, how the movement of Oak Ridge earthflow will likely shift due to climate change. In addition, our work provides a framework, more generally, for exploring how landslides filter rainfall variability and hence what controls the sensitivity of landslide displacement to interannual rainfall variability.

2.2 Methods

2.2.1 Site Description

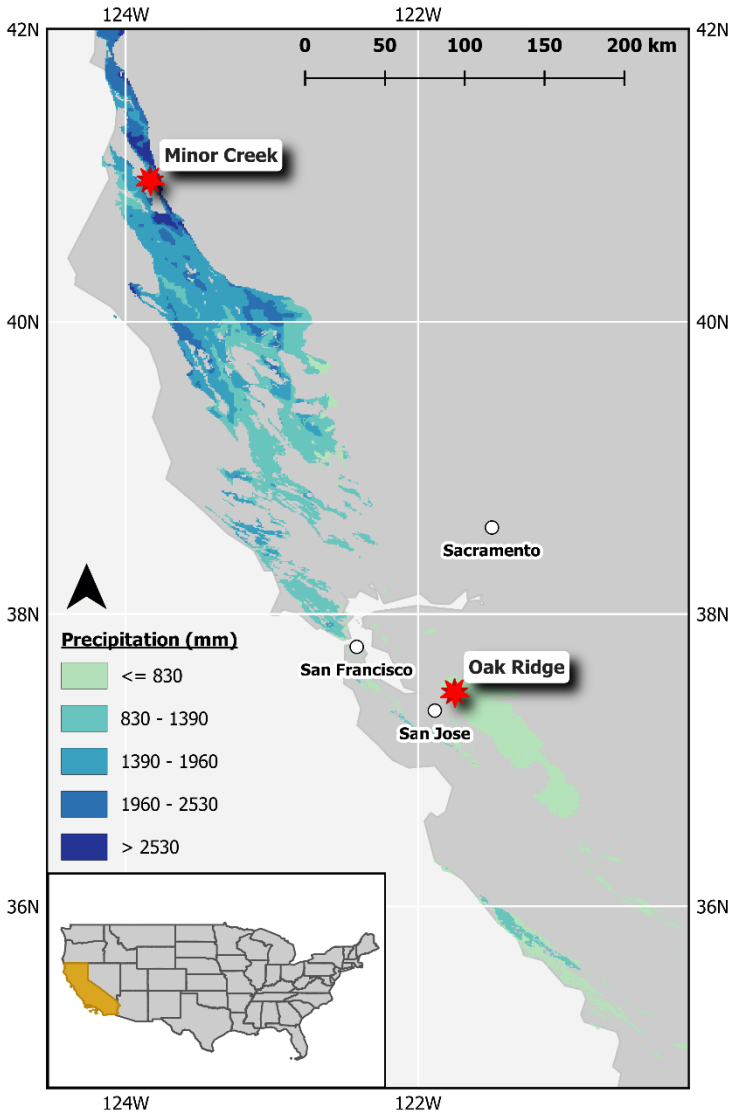

Figure 2.1 | Outcrop area of Franciscan mélange over California. Mélange locations are shown here colored by the average precipitation for the region (PRISM, 2022), illustrating the dramatic north-south precipitation gradient across the state. The location of Oak Ridge and that of another reference site discussed later, Minor Creek, are highlighted by red stars. Inset map shows the location of California (gold) in reference to the rest of the continental United States.

Oak Ridge earthflow is a large, seasonally active, earthflow located in the northern Diablo Range approximately 20 km northeast of San Jose, California, U.S.A. (Fig. 2.1). This site, which has been instrumented with piezometers and continuous GPS stations since 2016 (Finnegan et al., 2021; Murphy et al., 2022), receives an average of 566 mm of rain per year (PRISM, 2022). Rain falls predominantly between October and March, as is typical for a Mediterranean climate. Locally, geology at Oak Ridge consists of Mesozoic-early Cenozoic Franciscan Complex rocks (Rubin, 2002). Alternating

bands of sandstone and highly sheared, clay-rich mélange comprise the bedrock foundation beneath the earthflow; the landslide body itself is dominated by mélange (Murphy et al., 2022). Mélange, both in the body of the landslide and on the surrounding stable slopes, contains fragments of sandstone, chert, greenstone, and blueschist ranging in size from pebbles to large boulders which contribute to a characteristic hummocky topography. Soil cover on the mélange is very thin (~10 cm).

Oak Ridge earthflow spans 1.8 km in length (area = 0.35 km^2) along a south-facing slope of Oak Ridge with 600 m of relief and an average slope of 17°. The landslide is ~8 m deep in the transport zone (Murphy et al., 2022). Between 1937 and 2017, Oak Ridge earthflow moved >275 m in the fastest part of the landslide (Nereson & Finnegan, 2018).

2.2.2 Developing a base model

We used field observations from five years at Oak Ridge to develop a model linking subsurface pore-water pressure to landslide displacement following the approach of Finnegan et al., (2021). For the present study, we modeled variably saturated conditions at Oak Ridge using HYDRUS 1D (rather than vs2dt as applied in earlier work). HYDRUS is a commercial software package that solves the Richards equation (Richards, 1931) to simulate transient, variably saturated, subsurface water flow in a 1D column (Šimůnek et al., 2008) . The model domain consists of a single column with a thickness of 7.5 m, including a 0.5 m thick basal shear zone. The grid consists of 1001 variably spaced nodes. We use the van Genuchten-Mualem approach

(Mualem, 1976; Van Genuchten, 1980) to define the relevant water flow parameters for each hydrogeologic unit (Table 2.1, supplemental material). These parameters are the same as those used by Finnegan et al. (2021) including a measured saturated hydraulic conductivity of 7.1×10^{-8} m/s (Murphy et al., 2022) and an inferred shear zone conductivity of 6×10^{-9} m/s. The remaining hydrologic parameters were selected to match common values for silt loams (Carsel & Parrish, 1988), which are a close approximation of the material in the landslide body based on grain size measurements (Nereson et al., 2018). Upper boundary conditions consist of an atmospheric pressure boundary with surface runoff. The lower boundary condition is a free drainage boundary. We use a composite record of daily rainfall measured at Oak Ridge and another nearby gauge (Finnegan et al., 2021) to model subsurface hydrologic conditions during 2016-2022.

Our goal here is to use our hydrologic model to understand the general vadose zone dynamics that link rainfall variability, shallow pore-water pressure, and hence landslide displacement. Consequently, we adopt the simplest approach possible to facilitate our conceptual experiments. We compared the results of our base model to observations from a 2.5 m deep piezometer located in the transport zone of the landslide (description of piezometer installation and location can be found in Finnegan et al., 2021). Notably, this piezometer rarely saturates to the ground surface even when ponded conditions are observed on the landslide. We attribute this behavior to the hummocky topography of the earthflow which prevents the groundwater table from precisely matching local topography (e.g., Iverson & Major,

1987). To account for this, we adjusted our model domain by 0.5 m (see supplemental material in section 2.6.1). Extending our modeling to three dimensions and incorporating preferential flow (e.g., Krzeminska et al., 2013; Sidle & Bogaard, 2016) and material heterogeneity (e.g., Malet et al., 2005) would likely allow us to match the pore-water pressure more accurately, however we are able to capture the timing and relative magnitude of water table fluctuations at Oak Ridge with our simplified model (Fig. 2.5, supplemental material). This is sufficient to capture the essence of the system and facilitate our conceptual experiments with a minimum of tunable parameters.

We have observed a nonlinear relationship between pore-water pressure and landslide displacement at Oak Ridge (Finnegan et al., 2021; Murphy et al., 2022). Based on these observations, we predict landslide motion via pore-water pressure using an empirical equation relating our 2.5 m piezometer to displacement measured at a nearby GPS station. Above an initiation threshold, landslide displacement is proportional to pore-water pressure cubed (see supplemental material in section 2.6.2).

2.2.3 Climate Projections

Using this base model as a template, we then modeled groundwater behavior using an ensemble of bias-corrected dynamically downscaled precipitation projections (n=12) from the North American CORDEX (Coordinated Regional Downscaling Experiment) archive (Mearns et al., 2017). These data are produced at a spatial resolution of 0.22°/25km by running regional climate models using boundary

conditions from global climate model simulations found in the Coupled Model Intercomparison Project Phase 5 (CMIP5) archive. We use daily data from the RCP (Representative Concentration Pathway) 8.5 pathway, defined by the Intergovernmental Panel on Climate Change (IPCC) fifth assessment report as the highest emissions concentration pathway (Pachauri et al., 2015). Notably, as the high emissions scenario, RCP8.5 does not represent the most likely pathway for global climate change over the coming century. However, the higher forcing does produce a higher signal-to-noise ratio to facilitate detection of significant changes in the climate system. Thus, the resulting analyses, although likely an upper bound on hydroclimatic changes, provide an effective experiment for exploring how precipitation variability influences landslide displacement. Daily temporal resolution has been shown to be sufficient for modeling the behavior of deep-seated, slow-moving landslides (e.g., Finnegan et al., 2021). Using a multi-model ensemble helps to mitigate the inherent uncertainty associated with climate model projections and facilitates comparisons between models to see how our reference site may respond to variability within the ensemble. By modeling the hydrological response from 1950-2100 we can compare historic to future time periods and validate against existing records of landslide displacement.

Rising temperatures due to climate change have the potential to mitigate precipitation increases through increased evapotranspiration. Using a moisture balance index to account for changes in both precipitation and temperature, Coe (2012) forecasted a decrease in movement at Slumgullion landslide in Colorado, USA

by the end of the century. We tested the impact of including evapotranspiration in our hydrological model using the Hargreaves method built into HYDRUS 1D and found that while including evapotranspiration did cause a decrease in movement relative to models without evapotranspiration, there was minimal change in the relative trends when comparing historic modeled displacement to projected displacement (see supplemental material in section 2.6.3). Given that the relative difference in displacement does not change appreciably when including evapotranspiration, we did not include it in our models in favor of focusing on the hydrologic dynamics of infiltration and drainage within the landslide.

2.3 Results

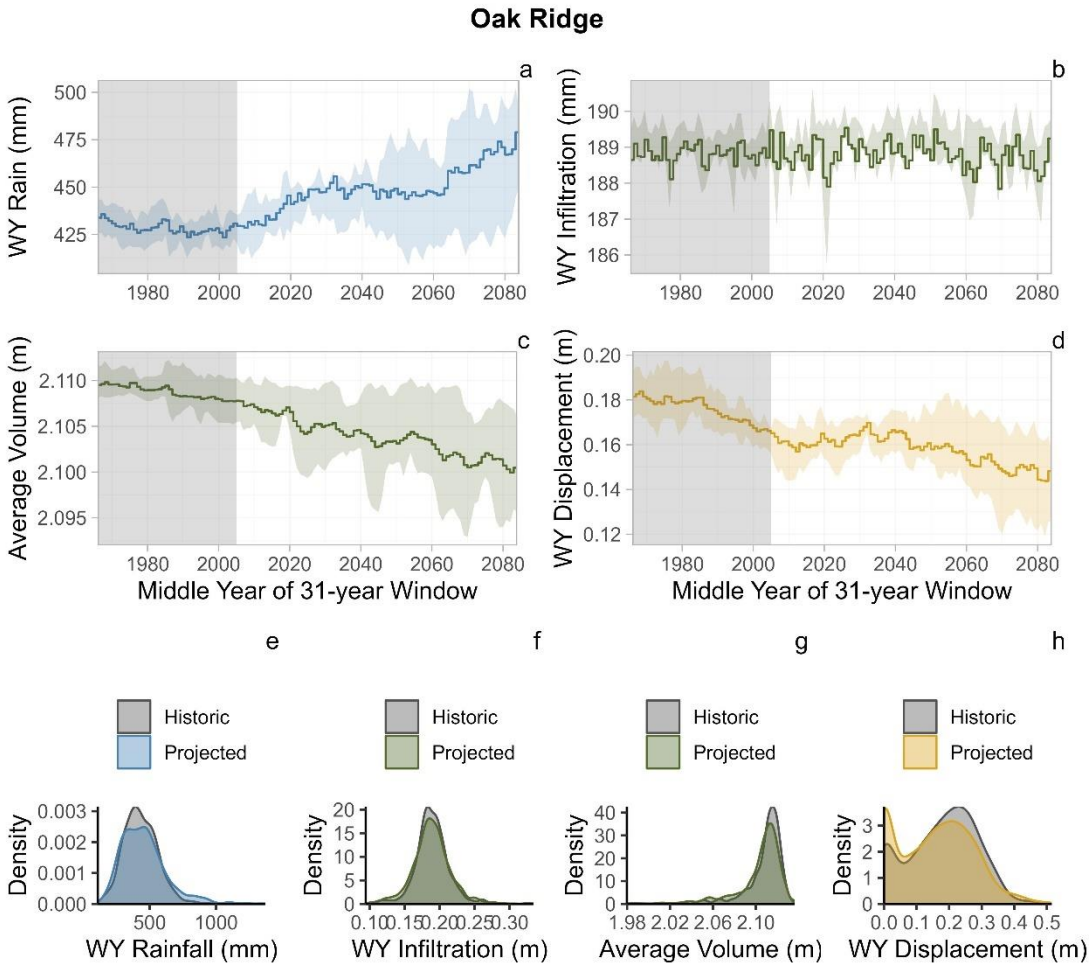

Figure. 2.2 | Modeled Conditions at Oak Ridge. (a-d) Ensemble averages of total water year (WY) rainfall **(a),** total WY infiltration **(b),** the average volume of water in the model domain (i.e., in the landslide) over the water year **(c),** and total WY displacement **(d).** For panels **a-d**, soil lines show the ensemble average smoothed using a 31-yr centered moving window for visualization purposes. Shading represents the 20th and 80th percentiles across the ensemble. Gray boxes indicate the historic period (1951-2005). **(e-h)** Density plots of total WY rainfall **(e)**, total WY infiltration **(f)**, average volume of water in the model domain **(g)**, and total WY displacement respectively **(h)**. These distributions encompass all years from all 12 ensemble members.

Water year rainfall (Oct. 1 – Sep. 30) ranges from 109 mm to 1372 mm across all 12 ensemble members. At Oak Ridge, we see a small but significant trend of 0.32 mm/yr in the ensemble average of water year rainfall between 1951 and 2100 (Mann-

Kendall test: p = 0.004; Sen's slope 95% CI [0.10, 0.52]). This results in a projected increase of approximately 10% from the historical average of 432 mm/yr by the end of the century (Fig. 2.2a). Comparing the distribution of precipitation during the historic period (1951-2005) with an equal range of years during the projected period (2045-2099), reveals a small but significant difference in variance as well (Fig. 2.2e; historic interquartile-range [IQR] 168 mm/yr; projected IQR 218 mm/yr; Brown-Forsythe test: F(1, 1318) = 44.392, p = 3.938e-11). Average annual rainfall in the CORDEX dataset (432 mm/yr) is less than the PRISM 30-year normal at Oak Ridge (566 mm/year).

We see no trend in annual infiltration over the study period (Mann-Kendall test: p = 0.87), however variation in annual infiltration does differ slightly between the historical (IQR 2.5 cm/yr) and projected (IQR 3.4 cm/yr) periods (Fig. 2.2f; Brown-Forsythe test: F(1, 1318) = 22.538, p = 2.285e-6). Infiltration ranges from 9 – 34 cm/yr across the ensemble with an average of 19 cm/yr.

Despite the projection of increasing rainfall and constant infiltration, we see systematic decreases in both the average volume of water in the landslide (Fig. 2.2c) and landslide displacement (Fig. 2.2d) from our models. The average volume of water exhibits a significant decreasing trend of -4.76e-5 m/yr, leading to an approximately 0.4% decrease from the historical average of 2.12 m by the end of the century (95% CI [-7.08e-5, -2.35e-5]; Mann-Kendall test: p = 4.57e-5). Variation in the average volume of water in the landslide is greater during the projected period (IQR 0.020 m) than the historic period (IQR 0.014 m) (Fig. 2.2g; Brown-Forsythe test: F(1, 1318) =

27.967, p = 1.444e-07). Landslide displacement exhibits a decreasing trend of -0.03 cm/yr, resulting in an approximately 18% decrease in annual displacement from the historical average of 18 cm/yr by the end of the century (95% CI [-0.0004 -0.0001]; Mann-Kendall test: p = 0.0002532). Variation in annual displacement also differs significantly between the historic (IQR 16 cm/yr) and projected periods (IQR 20 cm/yr) (Fig. 2.2h; Brown-Forsythe test: F(1, 1318) = 8.5597, p = 0.003496).

2.4 Discussion

Our model results forecast a decrease in annual displacement at Oak Ridge by the end of the century despite a small increasing trend in average annual rainfall. This runs counter to the common hypothesis that increasing frequency of extreme rainfall leads to greater landslide activity (e.g., Handwerger et al., 2019; Haque et al., 2019; Kirschbaum et al., 2020). We note that our modeling system uses many simplifications to capture the essence of behavior at Oak Ridge while ignoring potential complexities that may arise from detailed hydromechanical interactions (e.g., Carey et al., 2019; Iverson, 2005), material heterogeneities (e.g., Malet et al., 2005), or sediment supply limitations (e.g., Mackey & Roering, 2011). Consequently, we interpret these results focusing on the general patterns that arise rather than the exact magnitude of change. Below we discuss multiple mechanisms by which more extreme precipitation patterns may lead to a decrease in the activity of slow-moving landslides.

2.4.1 Impact of precipitation extremes on infiltration

Projected changes in annual precipitation across California are generally inconsistent and may vary regionally, however there is increasing consensus that future precipitation is likely to be more extreme, more volatile, and delivered during a shorter rainy season than our current baselines (Dong et al., 2019; Persad et al., 2020; Polade et al., 2017; Swain et al., 2018). By the end of the 21st century, some models project that the maximum precipitation event in parts of the western United States could be 50% larger than today (Chen et al., 2017) and in California the frequency of what is now a 50-yr event could double (AghaKouchak et al., 2018). The frequency of both wet and dry extremes is expected to increase, and a 25% to 100% increase in extreme dry-to-wet precipitation events has been projected (Swain et al., 2018). At Oak Ridge, we anticipate a slight increase in precipitation based on projections from the CORDEX dataset, however more rainfall does not strictly correlate with more landslide motion (e.g., Figure 2.2)

There are several facets of increasingly extreme precipitation which may mute the potential impact of more frequent wet years on landslide motion. First, increasing rainfall intensity during individual events may cause an increase in infiltration excess overland flow, leading to a larger fraction of rain being diverted to runoff that would have otherwise become infiltration during a less intense storm. Second, once the landslide becomes saturated, subsequent rainfall will runoff as saturation excess overland flow. This suggests that a contracting rainy season may lead to less landslide movement over time as more of the rain becomes concentrated in a smaller fraction of the year, causing a higher proportion of rain to fall on an already saturated landslide.

Although our model projects no change in average annual infiltration at Oak Ridge, we do see an increase in the frequency of both high and low infiltration years (Fig. 2.8, supplemental material) as well as an increase in runoff (Fig. 2.9, supplemental material), demonstrating how more intense rainfall may contribute to less infiltration and consequently less landslide movement in a given year.

However, an increase in rainfall intensity alone does not explain the decreasing trend in landslide displacement, as several ensemble members project a decrease in landslide displacement without an increase in runoff. In these cases, an increased frequency of years with low rainfall is likely a primary driver of decreasing displacement through low annual infiltration totals and/or the cumulative impacts of successive dry years. The latter effect is discussed in more depth in the following section.

2.4.2 Effect of memory on landslide movement

Although we anticipate a future increase in the frequency of both wet and dry extremes in California, their impacts will not necessarily be equal. The skewed distribution of average volume in the landslide (Fig. 2.2g) highlights an important asymmetry in our study system: the maximum volume, and by extension the maximum pore-water pressure possible without undrained loading effects, is constrained by the thickness and porosity of the landslide. While some ponding may occur due to the irregular topography of the landslide, the water table effectively cannot rise above the landslide surface (Murphy et al., 2022). Conversely, while very low conductivity shear layers at the base of the landslide likely contribute to the

existence of an ongoing perched water table in the landslide body (Baum & Reid, 2000; Nereson et al., 2018), pore-water pressures do decrease through drainage during periods without incoming recharge. This suggests that hydrologic behavior at Oak Ridge switches from being storage-limited during wet periods to precipitation-limited during dry periods. In the former case, rainfall exceeds available storage and excess water gets diverted into runoff. In the latter case, storage capacity exceeds infiltration, and the rate of incoming recharge may not be sufficient to keep up with drainage from the landslide. This asymmetry essentially means that while the hydrologic system cannot get ahead due to an upper limit on available storage, it can always fall farther behind.

Due to these system limitations, we anticipate that the increasing frequency of dry extremes will diminish the efficacy of wet years through the impact of antecedent conditions. The ability of a given amount of recharge to trigger landslide movement will vary through time depending on whether the initial water table is high enough to allow connectivity between the infiltrating wetting front and the water table (Finnegan et al., 2021). A year where drainage rates dramatically outpace incoming infiltration may lead to an unusually low water table at the start of the following water year. In this case, more rain than usual will be required to raise the water table back to a height sufficient to trigger landslide movement, meaning that while the landslide may receive an average or even above average amount of infiltration, a larger fraction of the infiltration occurs without triggering landslide movement. Consequently, when a wet year follows a dry year, it will be less impactful than it

otherwise would have been due to the drier antecedent conditions. Figure 3 illustrates this via the hydrologic dynamics and associated landslide displacement for a single ensemble member during a sequence of eight water years (WY). The sequence begins with WY2060, which exceeded the historical 80th percentile for rainfall (Fig. 2.3d). Above average rainfall was then partitioned into abundant runoff and relatively average cumulative infiltration (Fig. 2.3a). Following WY2060, we see a sequence of four years where annual rainfall was below the 20th percentile. This corresponds to below average displacements in WY2061 and WY2062, followed by no displacement in WY2063 and WY2064 (Fig. 2.3e). In 2065, above average rainfall leads to small amounts of displacement. Then in WY2066, rainfall below the 20th percentile leads to slightly above average displacement, followed by below average rainfall and no displacement again the following year.

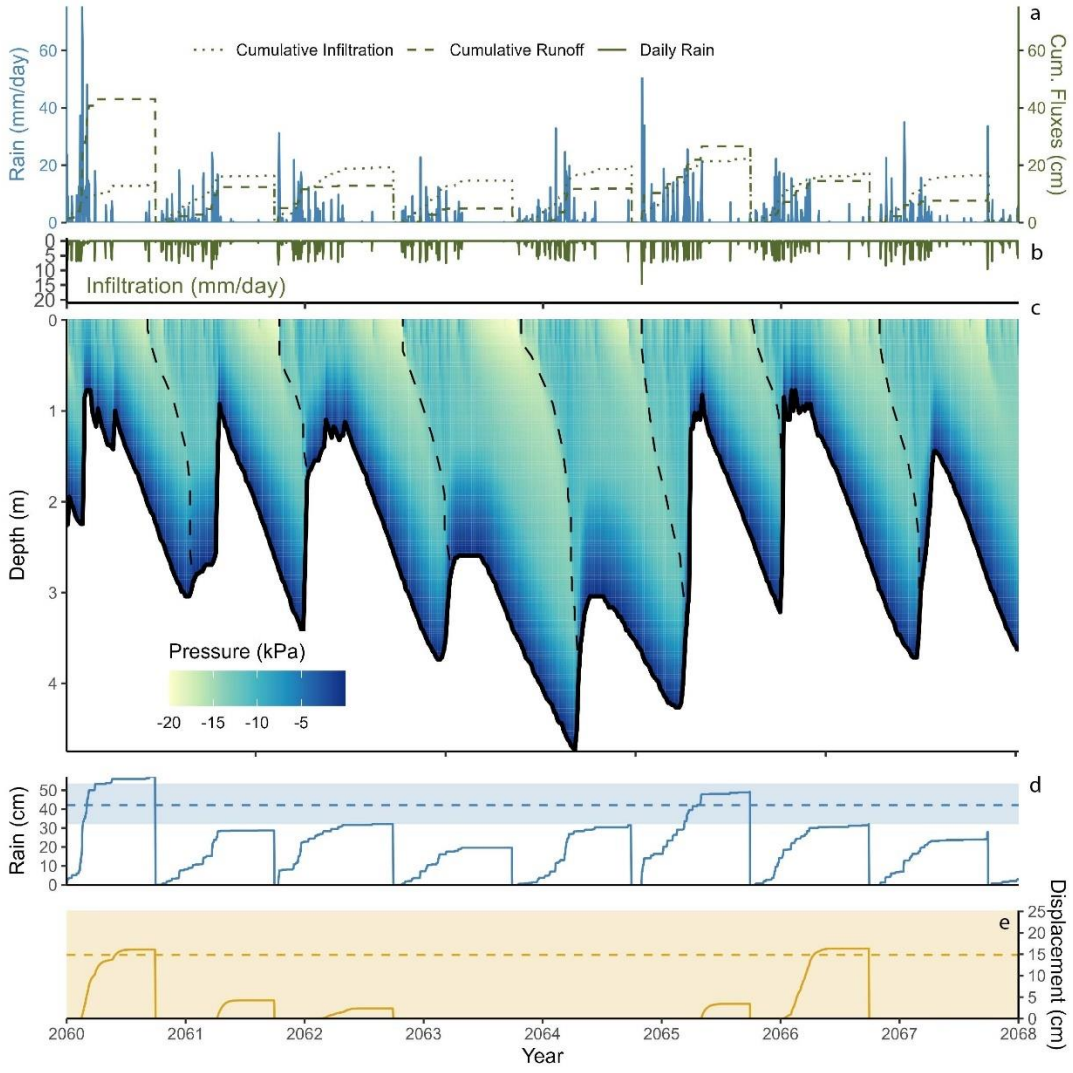

Figure 2.3 | Model results illustrating hydrological dynamics for a single ensemble member between 2060 and 2068. (a) Daily rainfall (solid blue line), and cumulative water year runoff (dashed green line) and infiltration (dotted green line). **(b)** Daily infiltration. **(c)** pressure head in the variably saturated zone over the 8-year period. The white region indicates water table depth. Dashed lines mark an approximation of the seasonal wetting front. **(d)** Cumulative water year rainfall (solid blue line). The dashed blue line represents the historical average and shading marks the 20th and 80th percentiles. **(e)** Same as in (d) but for displacement.

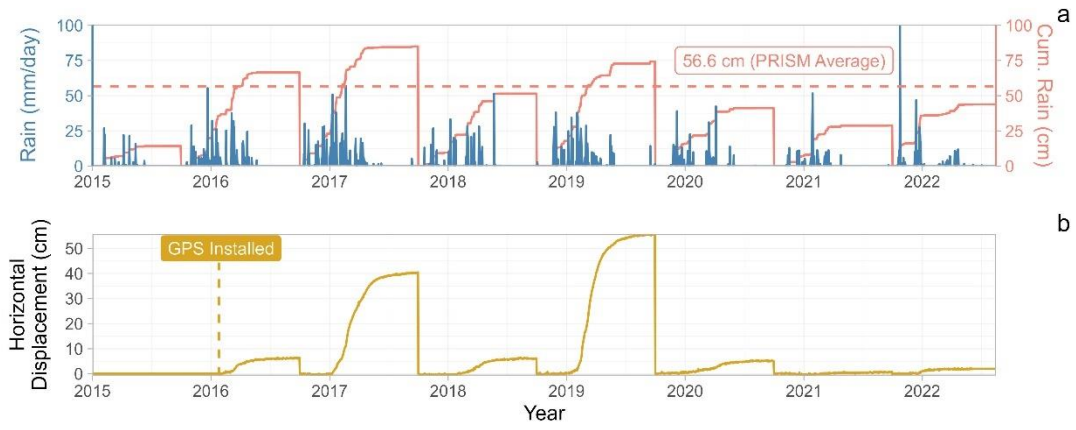

Figure 2.4 | Observations of rainfall and displacement at Oak Ridge earthflow. (a) Solid blue line represents daily rainfall. The solid pink line show cumulative water year rainfall. Dashed pink line marks the 30-year normal rainfall at Oak Ridge (PRISM, 2022). **(b)** Cumulative water year displacement recorded at the middle GPS station at Oak Ridge.

Field observations from Oak Ridge earthflow between 2016 and 2023 cover an extraordinary range of precipitation variability, as discussed above, and hence provide an opportunity to validate the results of the modeling. Notably, we can clearly observe the impact of antecedent conditions in field observations at Oak Ridge. In WY2016, we observed above average rainfall (67 cm) but very little movement (6 cm), followed by extraordinary rainfall (85 cm) and high movement (41 cm) in WY2017, and subsequently slightly below average rainfall (51 cm) and below average movement (6 cm) in WY2018 (Fig. 2.4). In WY2019, total rainfall (74 cm) was less than in WY2017 yet displacement was higher (55 cm). These patterns demonstrate how multiyear variability is integrated into long-term patterns of landslide movement. WY2015 was the last year of a historic drought, the effects of which we see propagating forward for the next two years.

2.4.3 Patterns of landslide movement across California

The impact of antecedent rainfall on slow-moving landslide activity was also apparent in observations of similar landslides across California between 2016 and 2018 using satellite-based interferometric synthetic aperture radar (InSAR) (Handwerger et al., 2022). In their survey, Handwerger et al. observed that while WY2016 had both wetter and drier average conditions across the state, landslide consistently moved slower than average, likely in response to lingering effects of the drought. In contrast, a few landslides exhibited higher than average velocities in WY2018, even though WY2018 was drier than average across the state. This demonstrates the sensitivity of the system to antecedent rainfall from the extremely wet WY2017.

Franciscan mélange, which hosts the majority of slow-moving landslides in California (Handwerger et al., 2022; Xu et al., 2021), spans a precipitation gradient of more the 2 m/yr (Fig. 2.1). As we have observed, Oak Ridge earthflow exists in an intermediate zone in that range where precipitation in some years far outpaces the dynamic storage capacity and in other years is insufficient to fill available storage. This framing is akin to the storage-limited vs precipitation-limited framework articulated by Hahm & Dralle et al. (2019) for Mediterranean plant productivity, but has not to our knowledge been explored for landslide dynamics. This framing leads to a natural hypothesis that landslides in the far northern part of the state, e.g., Minor Creek landslide located in Humboldt County (location marked in Fig. 2.1; Iverson & Major, 1987), should be buffered from the effects of drought as precipitation should almost always exceed available storage capacity. The driest years in this part of the

state are approximately equal to the wettest years at Oak Ridge (Fig. 2.10, supplemental material). Results from a 12-member ensemble model forecasting future movement at Minor Creek show no projected changes in annual rainfall, infiltration, or total volume of water in the landslide, but do show a slight decrease in annual movement (see supplemental material in section 2.6.4 and Fig. 2.11); annual displacement decreases by about 5% at Minor Creek as opposed to 18% at Oak Ridge. Given the small magnitude of this change, it is unclear whether the decrease in displacement stems from changes in precipitation patterns that are masked by annual rainfall statistics or whether it represents a type II error. These results also highlight the heterogeneity of expected precipitation changes over California and suggest a need for more widespread modeling to address regional changes. Notably, the hypothesis that landslides in consistently storage limited climates should be buffered from the effects of drought is inconsistent with the results of Handwerger et al. (2022) who found that the landslide behavior they surveyed was independent of both size and climate. This discrepancy highlights the potential importance of factors beyond hydrologic dynamics that may govern landslide motion, e.g., base-level forcing (Bennett et al., 2016; Roering et al., 2015) and sediment supply (Mackey & Roering, 2011).

While we cannot reliably predict the exact magnitude of future change at Oak Ridge and other similar systems due to the complex hydro-mechanical processes inherent to landslide motion and the interactions of those processes with external drivers such as sediment supply and baselevel forcing, we conclude that an increase

in precipitation variability in the future accompanied by little to no variation in the mean rainfall is likely to lead to a decrease in the movement of deep-seated, slow-moving landslides.

2.5 Conclusions

The integrated effects of multiyear precipitation patterns are key to forecasting slow landslide movement. At Oak Ridge, coupled simulations of landslide displacement and pore-water pressure indicate that landslide movement will likely decrease in the future as precipitation variability escalates in response to climate change. Because annual displacement totals are strongly dependent on seasonal antecedent conditions, the sensitivity of landslide displacement to interannual precipitation variability is governed by the ratio of subsurface storage capacity relative to rainfall. For a site like Oak Ridge that oscillates between precipitation-limited conditions in wet years and storage-limited conditions in dry years, this leads to a meaningfully asymmetric system where drainage during exceptionally dry years has a more significant impact on the landslide system than recharge during exceptionally wet years. These results emphasize that an increasingly intense future climate does not strictly lead to more landslide activity, even in areas where total rainfall increases. Instead, the memory of the system, dictated by the balance of available storage relative to infiltrating rainfall, governs landslide response to climate change.

2.6 Supplementary Material

	Saturated Water Content, θ_s (-)	Residual Water Content, θ_r (-)	α (1/m)	n	Saturated Hydraulic Conductivity (m/s)
Landslide Body	0.28	0.067	2	1.41	7.1×10^{-8}
Shear Zone	0.38	0.1	2.7	1.23	6×10^{-9}

Table 2.1 | Material parameters for HYDRUS simulation of Oak Ridge earthflow hydrology. α and n are parameters used in the van Genuchten-Mualem approach (Mualem, 1976; van Genuchten, 1980) to relate suction stress and moisture content with a given material. α represents the inverse of the air entry pressure head. n represents the pore-size distribution in the soil.

2.6.1 Calibrating the base hydrological model to field observations

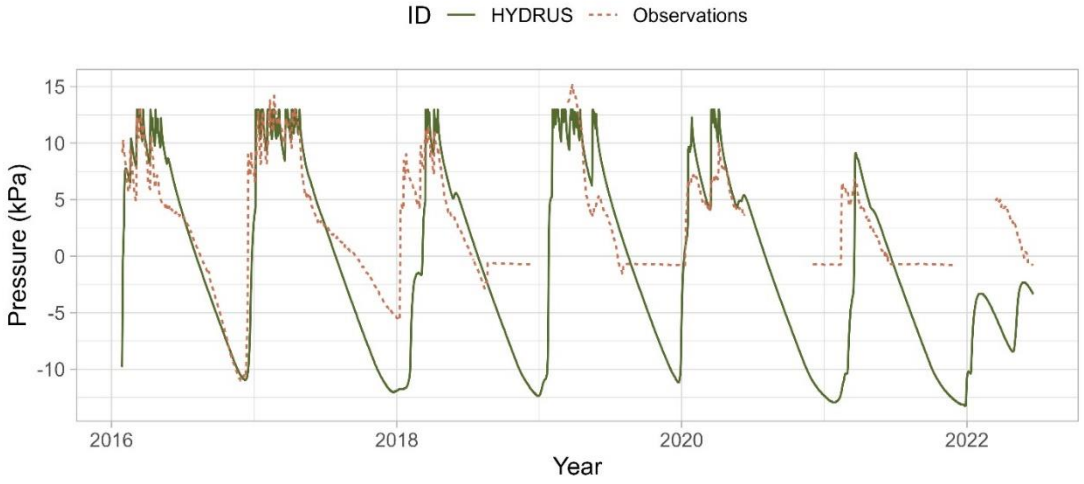

Fig. 2.5 | Comparing HYDRUS output to pore-water pressure observations at Oak Ridge. Solid green line shows output from HYDRUS converted from meters of water to kPa assuming hydrostatic conditions and adjusted downward by 9.5 kPa. Dotted red line shows observations from a piezometer installed at 2.5 m depth in the transport zone of Oak Ridge.

Pore-water pressure was recorded in the landslide body at Oak Ridge in 10-min intervals using a vibrating-wire piezometer (RST Instruments model VW2100-0.07) installed at 2.5 m depth in the transport zone of the landslide body. A full description of the installation process and resulting data can be found in Finnegan et al. (2021). In some years summer pore-water pressure drops far below atmospheric

pressure and during other years it abruptly reverts to zero. We interpret this variability to be due to the time-varying nature of the fracture network which sometimes facilitates equilibration with atmospheric pressure (e.g., when pressure abruptly reverts to zero during the dry months) and sometimes isolates the piezometer allowing recording of negative values due to suction.

HYDRUS produces pressure values in meters of pressure head. We convert these values to kPa assuming hydrostatic conditions and adjust the resulting values down by 9.5 kPa to minimize the root-mean-square error between the two series. In doing so, we can reasonably capture the timing and relative magnitude of pressure fluctuations at Oak Ridge in response to seasonal rainfall. Because the piezometer at Oak Ridge does not consistently record negative pressures, we only use positive values to fit our data.

2.6.2 Empirical relationship between landslide movement and pore-water pressure

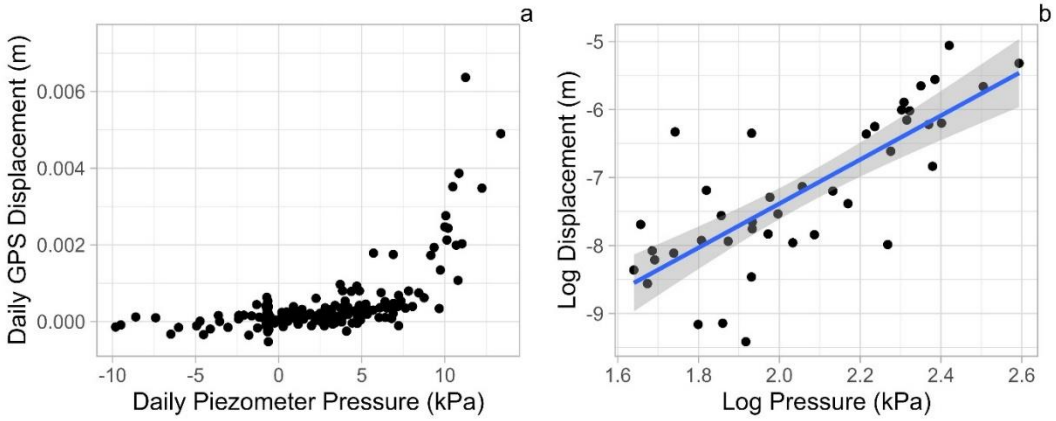

Fig. 2.6 | Empirical relationship between displacement and pore-water pressure. (a) Daily displacement (m) measured at the middle GPS station installed at Oak Ridge vs. daily pore-water pressure measured at the 2.5 m piezometer. Values have been smoothed with an 11-day moving average to minimize noise from the GPS. **(b)** Log-transformed data exceeding

the 5 kPa threshold required for landslide movement to initiate. The blue line shows a trend derived from linear regression. Shading represents 95% confidence intervals.

A coherent relationship between sliding velocity and pore-water pressure has been observed at Oak Ridge which implies the existence of a pore-water pressure threshold that governs landslide motion (Finnegan et al., 2021; Murphy et al., 2022). To develop a usable empirical relationship connecting landslide movement and pore-water pressure, we applied a centered 11-day moving average filter to our GPS and pressure measurements to minimize noise from the GPS. Landslide movement appears to begin when the 2.5 m piezometer reaches a pressure threshold of approximately 5 kPa (Fig. 2.6). We selected all the points above this threshold, applied a log-transformation, and then performed a linear regression to identify the trend (Fig. 2.6). This resulted in the following empirical relationship which we used to model landslide displacement:

$$D = 9.5e^{-7} * x^{3.2413}$$

where x is the pore-water pressure in kPa, and D is the displacement in meters.

2.6.3 Incorporating evapotranspiration into hydrological model

We tested the importance of including evapotranspiration (ET) on a single member of our ensemble (regional model RegCM4 driven by global climate model HadGEM2-ES). Setting the upper boundary condition as a time-dependent flux that accounted for both rainfall and ET, we determined daily potential ET values using

modeled temperatures from the CORDEX archive and a formulation by Hargreaves (1994). We accounted for root-water uptake with a plant water uptake stress response function (Feddes, 1978; Hoffman & Van Genuchten, 1983) assuming a rooting depth of 0.15 m based on field observations and following precedent at similar field sites in the San Francisco Bay area (Thomas et al., 2018). We set plant rooting depth to grow linearly from 0 to 0.15 between January and April and to decrease after that. Grasses at Oak Ridge are typically only active during winter (Nereson et al., 2018) hence we assume no transpiration occurs after June 1. Using these parameters, HYDRUS estimates actual ET based on root-water uptake and calculated pressure head.

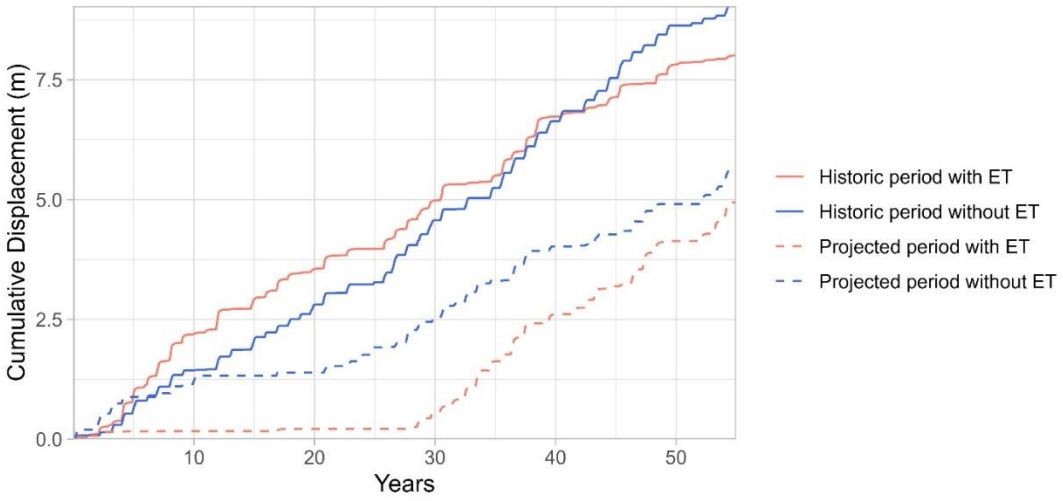

Fig. 2.7 | Comparing modeled displacement from a single ensemble member (rcm: RegCM4, gcm: HadGEM2-ES) with and without ET. Comparing cumulative displacement over 55 years in the historic (solid line; 1950-2005) and projected (dashed; 2043-2098) periods for the model with and without ET (pink and blue lines respectively).

Figure 2.7 compares cumulative landslide displacement over 55-year periods (1950-2005 and 2043-2098) to illustrate how landslide behavior shifts in the future with and without taking ET into account. Including ET lowers historic displacement

totals by 1 m and future displacement by 0.6 m. Notably, the relative differences between historic and projected scenarios remain similar in either case (3.1 meters when accounting for ET and 3.4 meters without ET). Given that relative differences remain similar regardless, we chose not to include ET in our modeling workflow for the sake of simplicity and maintaining a minimum number of tunable parameters.

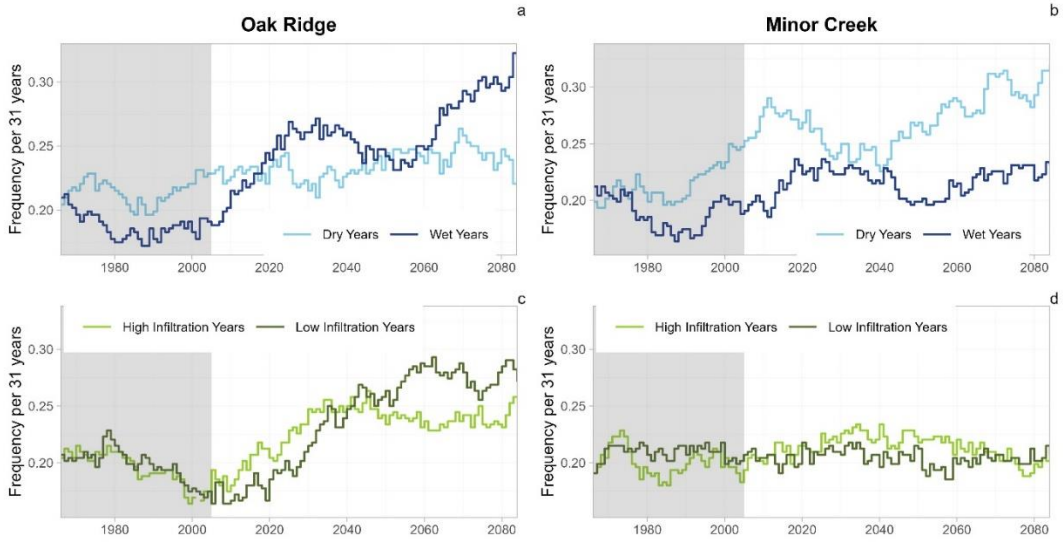

Fig. 2.8 | Change in frequency of extreme years. (a, b) Time series of the frequencies of dry years (light blue line) and wet years (dark blue line) at Oak Ridge (a) and Minor Creek (b). Following McKinnon and Dresser (2021), frequency is calculated empirically for moving 31-yr periods, the standard period used to calculate climate normals. We define dry years as those below the 20th percentile of historical water year precipitation and wet years as those above the 80th percentile. **(c, d)** Same as (a) and (b) but for infiltration.

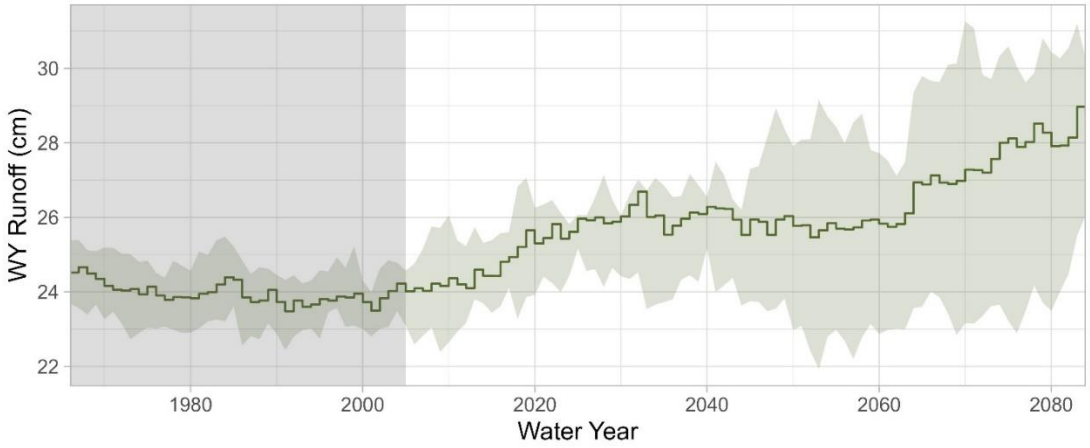

Figure 2.9 | Increase in runoff by the end of the century. Dark green shows average runoff in each water year across the ensemble, smoothed with a 31-yr moving window for visualization purposes. Green shading represents the 20th and 80th percentiles across the ensemble in each water year. Gray box marks the historic period (1951-2005).

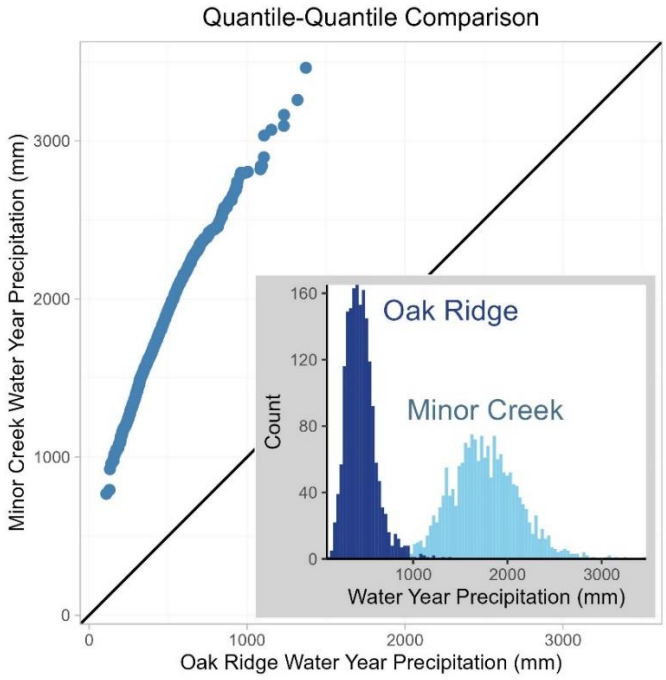

Fig. 2.10 | Comparing the distribution of rainfall at Oak Ridge and Minor Creek. Both the quantile-quantile comparison and the inset histogram illustrate the disparities in water year rainfall between Minor Creek and Oak Ridge. The driest years at Minor Creek barely overlap with the wettest years at Oak Ridge. Data are from CORDEX models of rainfall between WY1951 and WY2099.

2.6.4 Modeling landslide behavior in a storage-limited setting

To test the relative sensitivity to climate change of landslides in the wet and dry regions of the state, we developed a similar suite of simulations using modeled precipitation at Minor Creek. Note that our intent was to test how the system that we have developed would behave in a much wetter climate (Minor Creek behaves similarly to Oak Ridge, despite have three times as much rainfall, cite PRISM norms), thus we use the same hydrological model that is calibrated to Oak Ridge. This facilitates a direct comparison between the two regions rather than precisely replicating the nuances of Minor Creek.

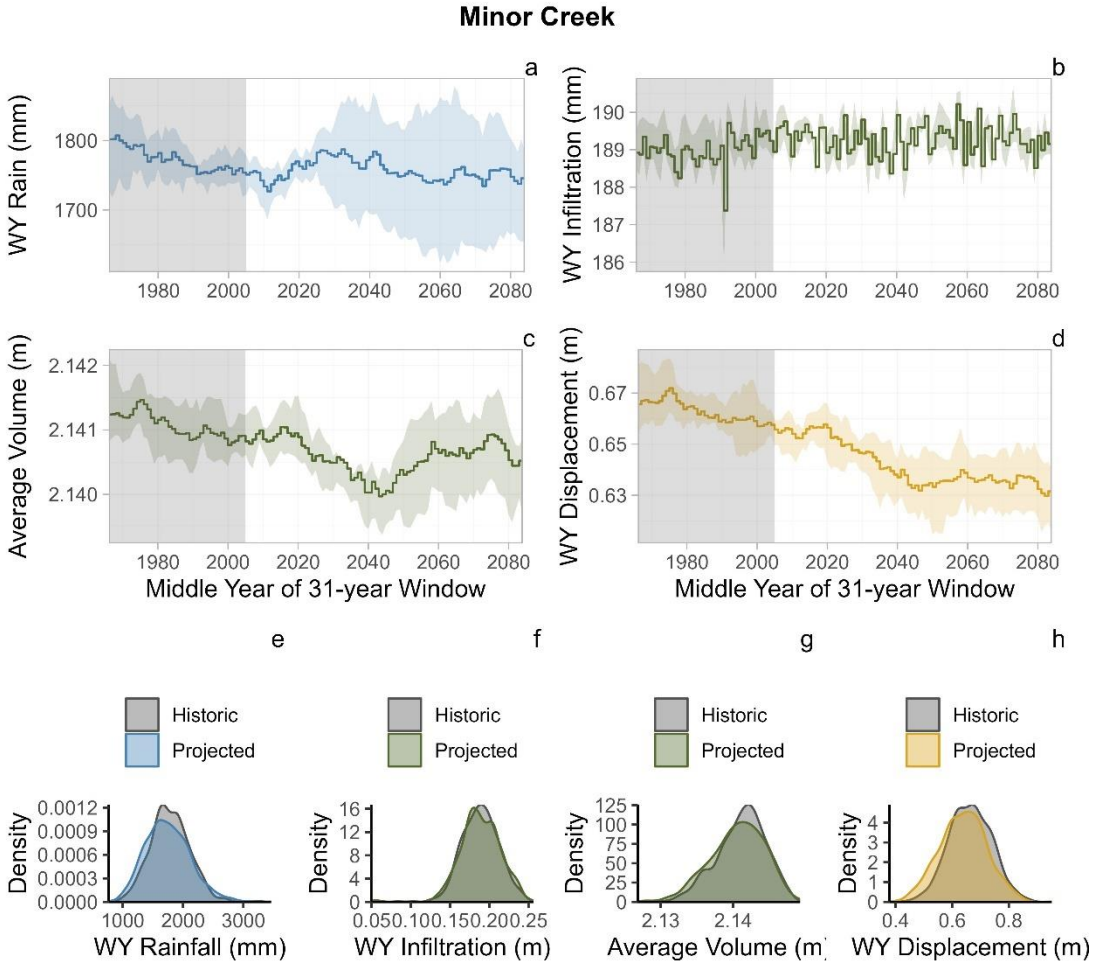

Fig. 2.11 | Projected Conditions at Minor Creek. (a-d) Ensemble averages of total water year (WY) rainfall **(a),** total WY infiltration **(b),** the average volume of water in the model domain (i.e. in the landslide) over the water year **(c),** and total WY displacement **(d).** For panels **a-d**, trend lines show the ensemble average smoothed using a 31-yr centered moving window. Shading represents +/- one standard deviation from the ensemble average. Gray boxes indicate the historic period (1951-2005). Axes have been fixed to facilitate comparison with Fig. 2 **(e-h)** Density plots of total WY rainfall **(e)**, total WY infiltration **(f)**, average volume of water in the model domain **(g)**, and total WY displacement respectively **(h)**. These distributions encompass all years from all 12 ensemble members.

At Minor Creek, we do not see a significant trend in ensemble average of water year rainfall between 1951 and 2100 (Fig. S7a; Mann-Kendall test: $p = 0.1053$). Average rainfall across the whole study period is 1762 mm/yr. The variance, however,

does increase. Comparing the distribution of precipitation during the historic period (1951-2005) with an equal range of years during the projected period (2045-2099), reveals a small but significant difference in variance as well (Fig. 2.11e; historic interquartile-range [IQR] 419 mm/yr; projected IQR 517 mm/yr; Brown-Forsythe test: $F(1, 1318) = 14.291$, $p = 0.0001636$).

We see no trend in annual infiltration over the study period (Fig. 2.11b; Mann-Kendall test: p-value = 0.7589) and no change in variance between the historic and projected periods (Fig. S7f; Brown-Forsythe test: $F(1, 1318) = 1.3145$, $p = 0.2518$). Average annual infiltration at Minor Creek is 0.19 m/yr.

We also see no significant trend in the average volume of water in the landslide (Fig. 2.11c; Mann-Kendall test: p-value = 0.2268), although we do see a small change in the variance between the historic (IQR = 0.004 m) and projected (IQR = 0.005 m) periods (Fig. 2.11g; Brown-Forsythe test: $F(1, 1318) = 4.0603$, $p = 0.04416$). The average volume of water in the landslide at Minor Creek is 2.14 m. The maximum volume is 2.15 m.

We do see a decreasing trend in landslide displacement of -0.0003 m/yr resulting in an approximately 5% decrease in annual displacement from the historical average of 0.66 m/yr by the end of the century (95% CI[-0.0004 -0.0002]; Mann-Kendall test: p = 1.385e-06). Variation in annual displacement also differs significantly between the historic (IQR 0.107 m/yr) and projected periods (IQR 0.113 m/yr) (Brown-Forsythe test: $F(1, 1318) = 6.931$, $p = 0.00857$).

Chapter 3: Numerical experiments reveal dominant hydromechanical controls on reactivation of coastal bluff landslides, Puget Sound, WA

Abstract

To improve landslide susceptibility maps and forecasts of landslide occurrence it is necessary to better understand the behavior and triggering conditions of reactivated and recurring landslides. The inherent unpredictability and destructiveness of landslides, however, makes it difficult to observe changes that happen during failure. Initial landslides may cause substantial alterations to subsurface hydraulic and mechanical properties, as well as topography and vegetation, often increasing the likelihood that the remaining landslide deposits will fail again in the future. Here, we leverage an existing dataset combining field and laboratory measurements from a reactivated landslide along the coastal bluffs of Puget Sound, WA (USA) to examine which changes were most influential in promoting landslide recurrence. We coupled an infiltration model with the infinite slope equation to evaluate failure conditions for idealized hillslopes using properties from the failed and unfailed monitoring sites. Using a nearby unfailed hillslope as a control, we performed a series of virtual experiments to test the relative importance of disturbances to vegetation, strength, and hydrologic properties for determining the timing of slope failures. We found that shifts in root reinforcement and saturated hydraulic conductivity had the largest impacts in our simulations, followed to a lesser

degree by properties of the soil water retention curve. We conclude that the loss of root strength and decrease in conductivity which occurred during the initial slope failure made the landslide site more likely to fail in the future relative to the unfailed control site. This suggests that we need to understand spatial and temporal evolution of hydraulic conductivity and root strength to better understand landslide recurrence phenomena and improve hazard assessments.

3.1 Introduction

Landslides commonly recur in the same location (Temme et al., 2020). This is true both on a landscape scale where regional conditions such as steep topography and low shear strength promote abundant landsliding (e.g., Roering et al., 2005), and on a hillslope scale where landslide deposits that do not fully evacuate are susceptible to remobilization in the future (e.g., Jibson, 2005). In the latter case, an initial landslide may influence susceptibility for subsequent failures by altering subsurface hydrologic or mechanical properties, for example by changing hydrologic connectivity due to altered fast flow pathways or reducing apparent cohesion by breaking tree roots. Consecutive landsliding systems present significant natural hazards and play an important role in landscape evolution, however they are difficult to incorporate into hazard assessments and geomorphic analyses because they violate a commonly held assumption of stationarity. Illuminating the dominant processes that control the behavior and triggering conditions of recurring landslides is critical for improving these assessments.

Reactivated landslide deposits have generated some of the most deadly and destructive landslides in the last two decades in the United States. In 2017, the Mud Creek landslide failed catastrophically after several years of slow deformation, closing California's Highway 1 for over a year and incurring more than $50 million in repair costs (Handwerger, Huang, et al., 2019; Warrick et al., 2019). In 2014, deposits from the 2006 Hazel landslide in Oso, Washington reactivated, causing a debris-avalanche flow and 43 fatalities (R. M. Iverson et al., 2015). In 2005, a landslide at La Conchita, California remobilized from a previous 1995 deposit causing 10 fatalities and damaging 36 homes (Jibson, 2005). These examples, while by no means comprehensive, illustrate the dangers that linger when landslide deposits remain after the initial failure.

Widespread recurrent landsliding also plays a fundamental role in landscape evolution by limiting mountain relief in response to rapid tectonic uplift and river incision (Burbank et al., 1996; Carson & Petley, 1970; Larsen & Montgomery, 2012) and regulating sediment supply to channels (e.g., Benda & Dunne, 1997; Mackey & Roering, 2011). In the northern California Coast Ranges, recurrent landsliding has been identified as a major source of coarse sediment which suppresses channel incision and landscape denudation allowing survival of relict terrain and orogenic relief in the wake of uplift (Bennett et al., 2016). The legacy of past landslides also influences soil depths and regeneration rates, which in turn modify future landslide susceptibility (Fan et al., 2021).

Here it becomes important to distinguish between correlated landsliding and path-dependent landsliding, sensu Temme et al. (2020). Correlated landslides refer to landslides that recur in a similar setting, either in multiple locations simultaneously, in the same location successively, or in multiple locations successively; the key distinction is that these correlated landslides arise due to conducive location properties, e.g., terrain steepness, not due to previous landslides. In contrast, path-dependent landsliding occurs when earlier landslides have a causal relation with later landslides. Reactivated landslides such as the Oso and La Conchita landslides are examples of path-dependent landsliding. The kind of recurrent landsliding that drives landscape evolution may include both correlated and path-dependent landsliding.

Historically, landslide susceptibility models have assumed that the likelihood of landslide occurrence is time independent. Recently however, large, multi-temporal landslide inventories in Italy (Samia et al., 2017) and Nepal (Roberts et al., 2021) have demonstrated that landslide susceptibility is influenced by path-dependency on a shorter timescale of 10-15 years. Taking into account path-dependency and variation in landslide spatial distributions through time has been shown to improve landslide susceptibility models (Jones et al., 2021; Jones et al., 2023; Samia et al., 2018, 2020). Crucially however, these analyses rely on statistical associations and do not attempt to mechanistically link consecutive landslides. Recurrent landsliding may arise from a number of factors, including debutressing of an existing landslide toe through wave action or bank erosion (Collins & Sitar, 2008; Pettit et al., 2014), buildup of pore-water pressure in colluvium-fill hollows due to steep, convergent topography (Ebel et

al., 2008; Montgomery & Dietrich, 1994; Wu & Sidle, 1995), and lithologic controls (Roering et al., 2005). For landslides that completely evacuate the failed material, recurrence is further governed by the timescale required for a sufficient supply of mobile sediment to accumulate through weathering and deposition (Imaizumi et al., 2015; Jakob et al., 2005; Parker et al., 2016). For landslides that do not fully evacuate the failed material (i.e., path-dependent reactivated landslides), there may be hydrological and mechanical changes to the landslide deposit (relative to the unfailed state) that affect the likelihood of future landsliding. For example, damage to vegetation during the initial failure may break roots and thus decrease cohesion (e.g., Schmidt et al., 2001) while also potentially increasing infiltration amounts by reducing canopy interception. Mechanically, landslide reactivation may also be facilitated by the "bathtub effect" where smearing and grain crushing along the main detachment surface during the initial failure leads to the formation of a low permeability clay layer at the landslide base, resulting in an elevated water table that promotes instability (Baum & Reid, 2000). The long lifespan of earthflows is commonly attributed to this mechanism.

In practice it is often difficult to distinguish between correlated and path-dependent landsliding, making direct field observations of landslide triggering conditions and assessments of soil hydrology and mechanical properties especially valuable. One of the rare instances of this elusive field data comes from (Mirus et al., 2017), who studied a pair of hillslopes along the coastal bluffs of Puget Sound to characterize the effects of landsliding on local hydrology and future slope stability.

By comparing their landslide site with a nearby stable hillslope, the authors identified changes in hydrologic connectivity and storage instigated by initial landslide failure that enhanced and prolonged susceptibility to further sliding within the remaining landslide deposit. However, beyond the empirical and qualitative interpretation of the field data this study does not include any causative or mechanistic analysis of landslide reactivation. Building on this work, we here leverage the existing field data from Mirus et al. (2017) to inform physically based hydro-mechanical modeling to identify the dominant processes and explore the conditions that control landslide recurrence. Specifically, we will use this model for virtual experiments to identify the relative importance of hydrologic properties vs strength parameters for determining the timing of landslide reactivation.

3.2 Methods

3.2.1 Site Description

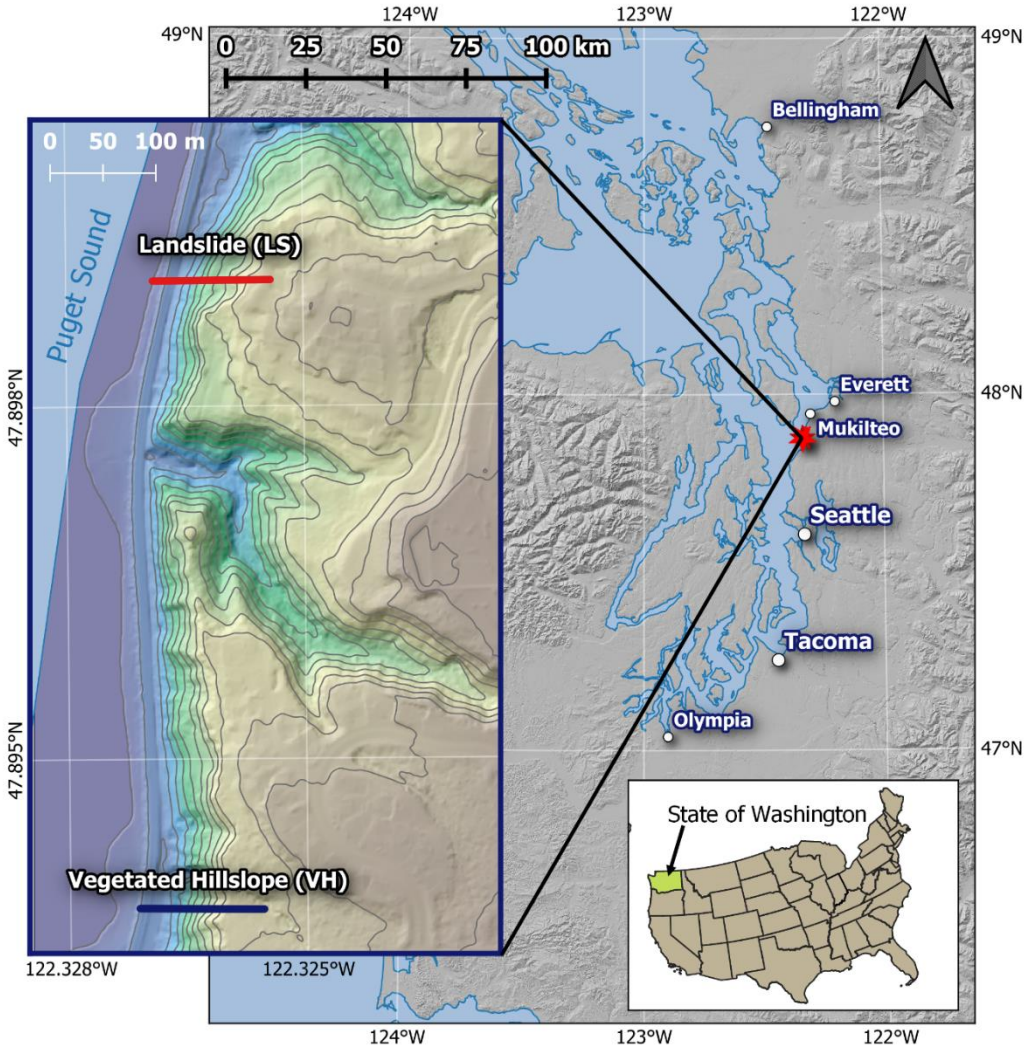

Fig. 3.8 | Map of Puget Sound showing location of field sites near Mukilteo, Washington, USA. Inset map shows a 1 m digital elevation model with the location of field sites from Mirus et al. (2017). Contour interval is 5 m.

Washington's Puget Sound region hosts numerous steep hillsides and coastal bluffs that frequently experience shallow translational landslides Baum et al., 2005a; Baum et al., 2005b; Baum et al., 2000; Godt et al., 2006). Most of these slides occur

between November and April when the region receives nearly three-quarters of its annual rainfall; total rainfall averages about 1 meter annually (Mirus et al., 2017). Regional geology consists of subhorizontally bedded glacial advance outwash sands and underlying glaciolacustrine silts that are particularly conducive to landsliding (Minard, 1983). Localized seeps and springs are also commonly observed, suggesting that perched water tables build up above glacial clay layers and force lateral flow through the overlying sand and gravel promoting instability (Baum et al., 2005). These frequent landslides often disrupt cargo and commuter rail service around Puget Sound and can pose financial and safety risks to both properties and people.

In 2015, the USGS started a monitoring campaign at two sites along the coastal bluffs of the Seattle-Everett railway corridor, within the city of Mukilteo, to study the hydrologic impacts of landslide disturbance and the resulting implications for landslide recurrence (Mirus et al., 2016, 2017; Smith et al., 2017). The study system consists of an existing landslide (LS), which failed initially in 2013 and has remobilized multiple times since then, and a vegetated hillslope (VH) located 0.6 km to the south, which has been stable throughout the monitoring period (Fig. 3.1). Aside from the effects of the previous slope failure, the hillslopes are very similar, making them valuable for testing how previous slope failures affect the likelihood of future mobilization. The two sites have the same total relief of 42 m measured from the railway line to the crest of the bluffs and they have similar average slopes (32° and 35° for the landslide and the vegetated hillslope, respectively). The underlying

geology at both sites consists of partially consolidated glacial till and outwash deposits (Booth et al., 2003; Minard, 1983).

At VH, the top ~1.5 meters consist of colluvium with evidence of bioturbation, macropores, and significant root density which supports a dense mixed forest with an understory of ferns and shrubs (Mirus et al., 2017). This contrasts with LS, where the landslide deposit consists of mostly clay and shows little evidence of soil development or obvious soil structures and hosts only the occasional tilted tree or shrub. Mirus et al. (2017) performed laboratory experiments to quantify the difference in soil structure between these two sites and found that the geometric mean of the saturated hydraulic conductivities is about 2 orders of magnitude lower at LS than VH and the porosity is about 20% lower (0.43 for LS vs. 0.56 for VH), suggesting that slope failure reduced the drainage and unsaturated storage capacity of the landslide site relative to the vegetated hillslope.

Subsurface monitoring also revealed seasonal differences between the two hillslopes. As part of the monitoring campaign, an array of piezometers, tensiometers, and volumetric water content sensors were installed along a transect of each hillslope. LS experiences positive pore-water pressures and near-surface soil saturation earlier than VH does and remains wetter longer. This creates an extended “landslide season” for LS relative to VH during which it is susceptible to slope failure. Tensiometer records, while demonstrating variability along the two hillslopes, broadly indicate that the saturated zone at LS responds more rapidly to individual storms than at VH and that the near surface remains wetter with higher pore pressures (Mirus et al., 2017).

The full list of installed monitoring equipment and recorded data can be found in Smith et al. (2017). A time-lapse camera installed onsite revealed slope movement at LS during the time periods of December 8–9, 2015; January 21–30, 2016; and March 9–14, 2016 Smith et al. (2017).

3.2.2 Hydrogeologic Modeling

To assess the dominant hydromechanical controls on landslide reactivation at our sites we employ the same space-for-time substitution as Mirus et al. (2017) and assume that differences in vegetation and soil properties at LS and VH are due to disturbances associated with the slope failures at LS which began in 2013. Building off of this assumption, we develop hydrogeological models of each site using HYDRUS 1D, a commercial software package that solves the Richards equation to simulate transient, variably saturated, subsurface water flow in multiple dimensions (Šimůnek et al., 2008). After developing one representative base simulation each for the landslide site (LS) and the vegetated hillslope (VH), we performed a series of 16 virtual experiments where we altered parameters within these simulations one at a time to test which of the observed physical differences between the two sites significantly affected the subsurface hydrologic conditions and slope stability. We evaluated stability by comparing pore pressure and factor of safety time series for each scenario. These experiments allow us to resolve the key influences of hydromechanical variables (saturated hydraulic conductivity, K_{sat}; saturated soil water content, θ_s; residual soil water content, θ_r; the inverse of the air-entry pressure head value, α; the pore size distribution shape parameter, n; and apparent cohesion, c’),

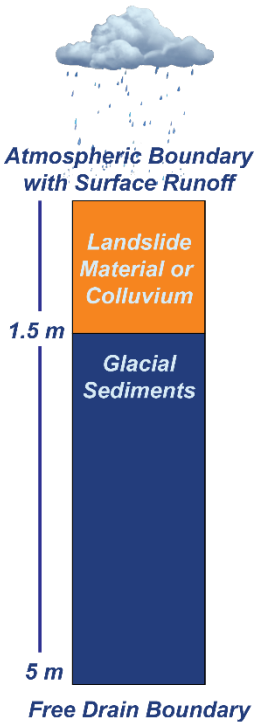

Fig. 3.2 | Model domain for HYDRUS 1D simulations.

particularly which one(s) have the strongest control on pore pressure in one dimension. We also tested the effects of canopy interception and antecedent conditions.

Our base models consisted of a 5-meter-deep column, with 1.5 meters of colluvium/landslide material overlying 3.5 meters of glacial sediments (Fig. 3.2). This roughly aligns with the depths of the landslide/colluvium layers observed in excavated soil pits at the two sites (Mirus et al., 2016), although we chose a discrete boundary here to simplify our simulations rather than replicate the gradual transition that was observed in the field. The finite element mesh for each boundary-value problem contains 1001 nodes with increased nodal density (closer spacing) at the surface and at the boundary between the two hydrogeologic units. We included observation nodes at various depths corresponding to sensor locations at LS and VH to allow us to compare continuous time series of simulated and observed pore pressure (ψ) and water content (θ).

We use the van Genuchten-Mualem approach (Mualem, 1976; Van Genuchten, 1980) to define the water flow parameters for each hydrogeologic unit. The relevant water flow parameters for input into HYDRUS are saturated hydraulic conductivity (K_{sat}, m/s), saturated soil water content (θ_s), residual soil water content (θ_r), the inverse of the air-entry pressure head value (α, 1/m), and the pore size

distribution shape parameter (n). We parameterized the base case of the vegetated hillslope using existing laboratory measurements from Mirus et al. (2016). Based on grain size percentages, we use typical parameters for a silty clay loam to parameterize the landslide base case (Carsel & Parrish, 1988). Notably, the K_{sat} used for the landslide material and listed in Table 3.1 (1.94e-7 m/s) is very close to the fasted K_{sat} measured in the lab for the landslide (3e-7 m/s). Field observations of the underlying glacial deposits indicated that the material was clay-rich and less conductive than the overlying colluvium and landslide deposits, hence we parametrized this layer using typical values for a silty clay (Carsel & Parrish, 1988). Relative to VH soils, the LS parameters represent a much finer-grained, slowly draining soil. The glacial sediment parameters, meanwhile, represent an even finer-grained and less conductive material than both LS and VH. For both LS and VH, we use K_{sat} values at the upper end of the measured range. Given that the laboratory values represent point measurements and do not consider possible fast flow pathways, we assert that the upper end of the hydraulic conductivity distribution provides a reasonable representation of the effective conductivity governing pore pressure response in the field.

The upper boundary condition for all simulations is atmospheric pressure with surface runoff that uses 15-min precipitation measurements recorded on site as input (Smith et al., 2017). We focus on the period between January 1, 2016 and January 31, 2016 because slope failures were observed at LS during the second half of the month. Given that this is a relatively short period of time, we include antecedent conditions in our suite of tested variables to examine differences between the two sites. Because

the simulated time occurs during the rainy winter season, we assume evapotranspiration fluxes are minimal and do not include them in the model input. The lower boundary uses a free drainage condition that is recommended for situations when the water table lies far below the domain of interest (Šimůnek et al., 2008).

We used a variation of the "rain and drain" warm-up simulation protocol described by (Mirus et al., 2011) to establish initial conditions that approximated observed field conditions (Smith et al., 2017). For each simulation, we set a uniform initial pressure head everywhere of -0.1 m and drained the system for approximately 35 days to establish a reasonable distribution of pressure head. For each simulation, we then applied rain at 6 x 10^{-8} m/s until we reached pressure conditions that approximated tensiometer measurements at the beginning of January 2016 (2.2 kPa at 1.42 meters depth for LS and -1.8 kPa at 1.22 meters depth for VH). Because the time required to reach these initial conditions depends on the soil properties, each of the virtual experiments required a different number of days for warm up.

To evaluate how the altered parameters affected the likelihood slope failure, we calculated a factor of safety (FS) time series for each simulation listed in Table 2. To do this, we first calculated the suction stress with the Lu & Likos (2004) approach at the boundary between the overlying layer and the glacial sediments (1.5 m depth):

$$\sigma^s = -\frac{\theta - \theta_r}{\theta_s - \theta_r}(u_a - u_w) \quad (1)$$

where σ^s is the suction stress [$ML^{-1}T^{-2}$], θ is our modeled (dimensionless) water content [-], u_a is the atmospheric pressure [$ML^{-1}T^{-2}$] (here assumed to be zero), and u_w is the pore-water pressure [$ML^{-1}T^{-2}$].

We calculated factor of safety using our calculated suction stress and the infinite slope equation from Lu & Godt (2008):

$$FS(t) = \frac{c' + [\gamma d cos^2\beta - \sigma^s(t)]tan\varphi'}{\gamma d sin\beta cos\beta} \quad (2)$$

where c' is the effective cohesion [$ML^{-1}T^{-2}$], γ is the unit weight of the combined soil and water [$ML^{-2}T^{-2}$], and d is the depth to the failure plane [L], β is the slope angle [°], and φ' is the effective friction angle [°]. Values for cohesion, friction angle, and slope angle are listed in Table 3.1. We set d as the boundary between the landslide deposit/colluvium and the glacial sediments, i.e., 1.5 m. Following precedent, we calculated γ, the unit weight of the landslide material, for each simulation assuming full saturation (Lu & Godt, 2012):

$$\gamma = \gamma_w \left[\frac{G_s + eS}{1 + e}\right] \quad (3)$$

where γ_w is the unit weight of water [$ML^{-2}T^{-2}$], G_s is the specific gravity [-], e is the void ratio [-], and S is the saturation [-]. We assume γ_w equals 9.8 kN m^{-3} and G_s equals 2.65 (Freeze & Cherry, 1979).

The relevant parameters for slope stability are friction angle (φ', deg.), slope angle (β, deg.) and cohesion of the landslide material/colluvium (c', kPa). Based on laboratory strength testing of limited core samples (Mirus et al., 2016), we estimate a friction angle of 29° for both LS and VH. Properties for the glacial deposits were not measured so we assume they have very high strength parameters. Laboratory measurements of samples from LS and VH recorded negligible values of both total and effective cohesion (Mirus et al., 2016), thus we assume that c' for each site represents an apparent cohesion that stems entirely from root reinforcement. We use 4 kPa for apparent cohesion at LS and 8 kPa at VH to test two end members of low and high(er) cohesion. Based on aerial imagery, approximately half the surface area of LS was vegetated in January 2016, whereas the entire hillslope was vegetated at VH. Accordingly, we assign the 2x higher cohesion value to VH to represent the extensive root network relative to LS. These values are based on the upper range of values reported for similar vegetation in Washington State (Schmidt et al., 2001). The complete list of hydrologic and stability parameters for the base case simulations are listed in Table 3.1.

Table 3.1: Base Model Parameters

Unit	K_{sat} (m/s)	θ_s	θ_r	α $(1/m)$	n	φ' (deg.)	β (deg.)	c' kPa
VH Colluvium	1.08e-5[1]	0.56[1]	0.14[1]	2.8[1]	1.47[1]	29	35	8
LS Material	1.94e-7[2]	0.43[2]	0.089[2]	1[2]	1.23[2]	29	32	4
Glacial Deposits	5.55e-8[3]	0.36[3]	0.07[3]	0.5[3]	1.09[3]	-	-	-

[1] Measured in laboratory tests by Mirus et al. (2016)
[2] Typical parameters for a silty clay loam (Carsel & Parrish, 1988).
[3] Typical parameters for a silty clay (Carsel & Parrish, 1988).

3.2.3 Virtual Experiments

We use our two base case scenarios to perform a series of 16 virtual experiments designed to test the relative influence on the subsurface hydrologic response and slope stability of rainfall, initial conditions, and each of the input soil parameters. In each of these 16 scenarios, listed in Table 3.2, we replace a single parameter in the base case simulation with the relevant parameter from the other base case. This allows us to see how the wetter, less permeable, and more disturbed conditions of the landslide affect the pore pressure response of the vegetated hillslope and vice versa. We test all parameters listed in Table 1 except for the friction angle (φ) and the slope angle (β) because the former is identical between the two sites and the latter is only 3 degrees different. For scenarios 6 and 14, we switch the input precipitation between LS and VH to test the effects of differences in canopy interception. For scenarios 7 and 15, we exchange initial conditions between the two

sites to test the effects of antecedent conditions. See Table 3.2 for the full list of experimental scenarios and parameters.

Scenario 1 (LS base properties with the faster K_{sat} from VH) initially failed to converge due to numerical instabilities. This arises from a well-known issue in HYDRUS where the model becomes unstable due to saturation excess infiltration, most commonly with fine-grained soils, $n < \sim 1.1$ (Šimůnek et al., 2008). Given the fine-grained nature of our landslide material and glacial deposits, we use the modified van Genuchten-Mualem model with an air entry value of -2 cm for all scenarios to improve the description of the hydraulic conductivity function near saturation (Schaap & Van Genuchten, 2006; Vogel et al., 1985, 2000). However, this modification is insufficient to achieve full convergence when describing rapid hydraulic conductivity in an otherwise fine-grained soil. Considering this, we ran scenario 1 in a piecewise fashion by reinitiating the simulation after each failed convergence using the pore pressure distribution from the last time step. Each period of instability occurred during a period of high intensity rainfall, so we assumed that complete saturation lasted until the rainfall intensity decreased and restarted the simulation after the peak rain was over.

Table 3.2: Parameters used for the virtual experiments

Scenario	K_{sat} (m/s)	θ_s	θ_r	α	n	Precip	IC*	c'	Time of first failure
				Landslide					
1	VH	LS	LS	LS	LS	LS	Wet	LS	Jan 21, 18:00
2	LS	VH	LS	LS	LS	LS	Wet	LS	---
3	LS	LS	VH	LS	LS	LS	Wet	LS	Jan 22, 05:15
4	LS	LS	LS	VH	LS	LS	Wet	LS	---
5	LS	LS	LS	LS	VH	LS	Wet	LS	---
6	LS	LS	LS	LS	LS	VH	Wet	LS	Jan 22, 10:00
7	LS	LS	LS	LS	LS	LS	Dry	LS	Jan 22, 08:00
8	LS	LS	LS	LS	LS	LS	Wet	VH	---
				Vegetated Hillslope					
9	LS	VH	VH	VH	VH	VH	Dry	VH	---
10	VH	LS	VH	VH	VH	VH	Dry	VH	---
11	VH	VH	LS	VH	VH	VH	Dry	VH	---
12	VH	VH	VH	LS	VH	VH	Dry	VH	---
13	VH	VH	VH	VH	LS	VH	Dry	VH	---
14	VH	VH	VH	VH	VH	LS	Dry	VH	---
15	VH	VH	VH	VH	VH	VH	Wet	VH	---
16	VH	VH	VH	VH	VH	VH	Dry	LS	---

* Wet IC LS = 0.22m pressure at 142cm; Dry IC VH = -0.18m pressure at 122cm
--- no failure

3.3 Results

3.3.1 Base Cases

The 1D base case models roughly match the measured pore pressure record in magnitude and timing (Fig. 3.3). It is challenging to match the records exactly given the simplifications that are inherent to a 1D simulation (ignoring topography, assuming homogeneity, using a discrete hydrogeologic boundary, etc.). Notably however, the base case results follow what we would expect to happen conceptually for the month of January based on the measured rainfall. The pore pressure response is muted until around January 13 when the effects of the first notable rainstorm enter the record. Following this, we see a dramatic wet up around January 21 when the most intense and prolonged rainstorms occur; after this point, the modeled pore pressure is very responsive to any further input having reached saturation. Importantly, when we incorporate the modeled hydrologic response into our factor of safety calculations, we closely replicate the timing of hillslope failures compared to what was seen in the field (Fig. 3.3). Hence, we feel confident using these base models to conduct our 1D virtual experiments.

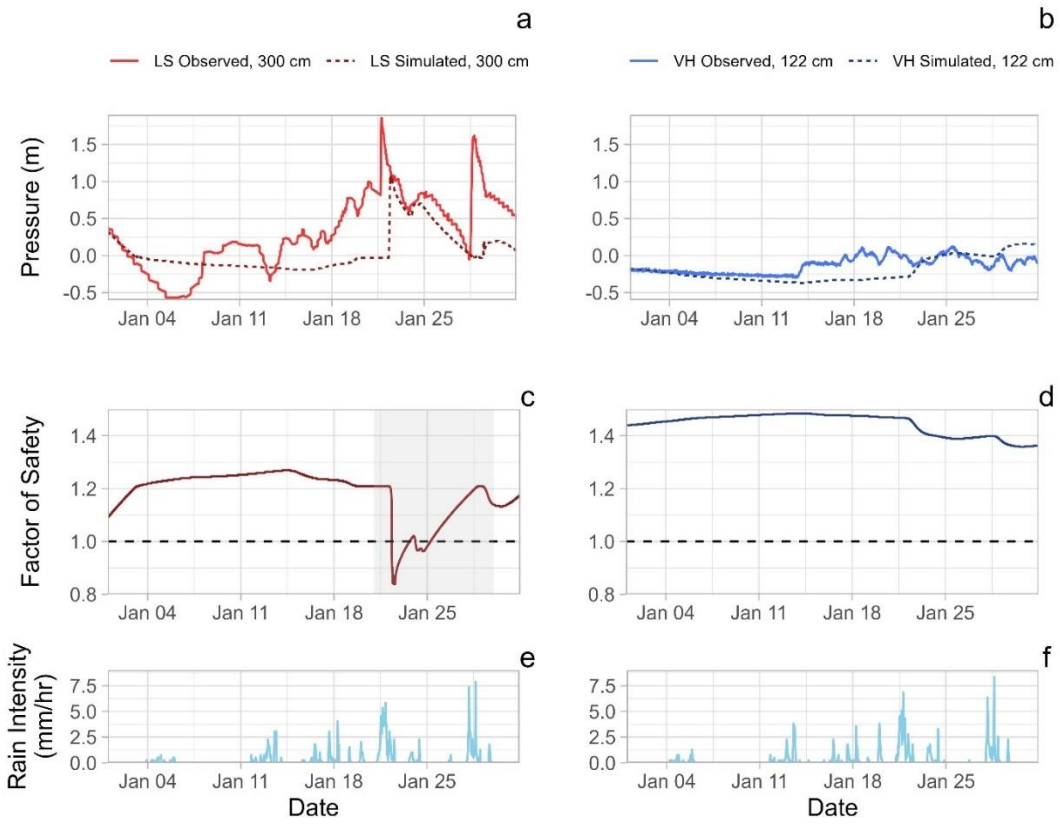

Fig. 3.3 | Base Model Results (a, b) Simulated (dashed line) versus observed (solid line) pressure head during January 2016 at LS (a) and VH (b). **(c, d)** Simulated slope stability at LS (c) and VH (d). Dashed horizontal line represents the threshold for instability. Gray shaded box in part c marks the observed period of instability at LS. **(e, f)** Recorded hourly rainfall intensity shown for LS (e) and VH (f). Observed data from (Smith et al., 2017).

3.3.2 Hydrologic changes

Raising the hydraulic conductivity in the landslide relative to the base case (Scenario 1) causes the pore-pressure record to be more responsive to rainfall (Fig. 3.4a). Pressures rise about a half day earlier in response to the late January rains. Peak pressures reached are approximately 0.35 m higher than the base case and they remain relatively elevated through the remainder of January. In contrast, lowering the hydraulic conductivity in the vegetated hillslope (Scenario 9) causes pore-water

pressures to rise approximately three days later than in the base model (Fig. 3.4b). Pressure changes in response to rainfall and generally more muted and they remain about 0.5 m lower from January 21 onwards.

Altering saturated soil water content (scenarios 2 and 10) produces moderate change relative to the landslide and vegetated hillslope base cases (Fig. 3.4 c,d). When θ_s is increased relative to the LS base case, the system requires about half a day longer to respond to the January 21st storm sequence and ultimately the maximum pressures are ~0.25m lower (Fig. 3.4c). After January 25th however, the pressures remain ~0.25m higher. Similarly, decreasing θ_s relative to the VH base case in scenario 10 causes the wetting front to move faster and the pore pressures to remain ~0.3m higher after wetting up on January 22nd (Fig. 3.4d). Changing the residual soil water content, θ_r (scenarios 3 and 11), causes very little change for either LS or VH (Fig. 3.4 c,d).

Altering the scaling parameters α and n has a bigger effect on the modeled pressures. Scenario 4, which pairs LS base parameters with a higher α, causes the simulation to saturate slower by about 1 day and decreases the maximum pore pressures by ~0.5m, however the pore pressures then remained higher than the base case by ~0.25m for a few days before dipping below the base case pressures again on January 30th (Fig. 3.4e). Increasing n in scenario 5 has a similar effect, but with slightly less lag to saturation and without the dip in pore pressures at the end of January (Fig. 3.4e). In contrast, decreasing α and n relative to the base VH parameters in scenarios 11 and 12 respectively causes the simulations to wet up ~1 day faster in

response to the late January storm inputs and to retain pressures ~0.5m higher than the base case for the remainder of the simulation (Fig. 3.4f).

Exchanging the input precipitation between LS and VH (scenarios 6 and 14) has little to no effect on the modeled pore pressure (Fig. 3.4 g,h). Changing the antecedent conditions for VH caused the system to stay ~0.1-0.2m wetter the entire time than the base case (scenario 15), but the similar swap to dry antecedent conditions for LS (scenario 7) produced no noticeable effect; in fact, the two simulations were nearly identical beyond January 10 and wetted up as a result of the January 21st storm sequence almost simultaneously (Fig. 3.4 g,h).

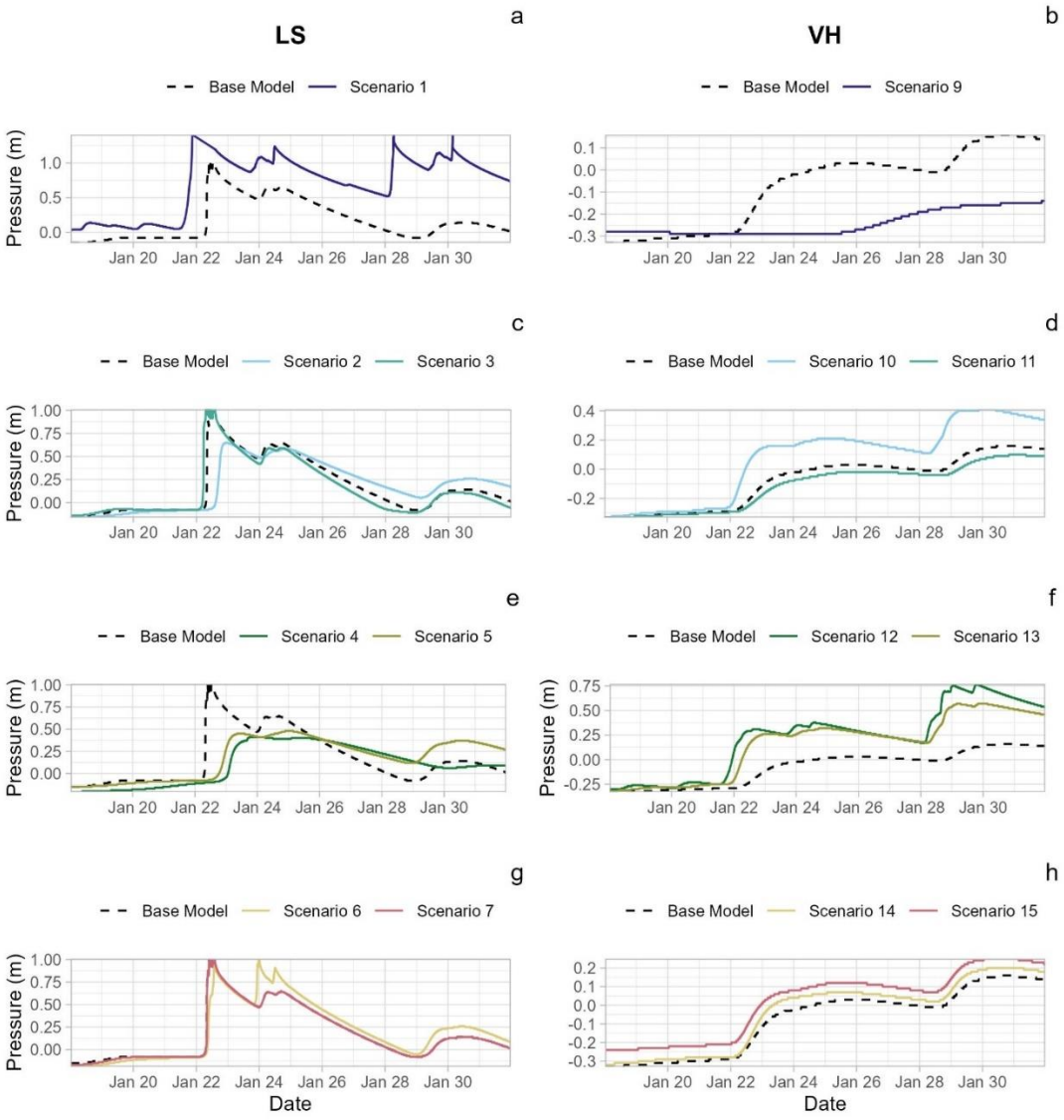

Fig. 3.4 | Simulated pore-water pressures from hydrologic scenarios. (a) Increased hydraulic conductivity (blue line) relative to the base landslide model simulated at 142 cm depth. **(b)** Decreased hydraulic conductivity relative to the base vegetated hillslope model simulated at 122 cm depth. **(c, d)** Same as (a) and (b) for saturated and residual water contents. **(e, f)** Same as (a) and (b) for α and n. **(g, h)** Comparing the effects of altered canopy interception and antecedent conditions.

3.3.3 Factor of Safety

Based on the factor of safety calculations, 4 of the 8 scenarios for LS (in addition to the base case) were likely to fail at some point during the storm sequence in the second half of January 2016. The least stable scenario resulted from increasing the hydraulic conductivity, which caused the factor of safety to abruptly drop below 1 on January 21 at 18:00 and remain <1 for the rest of the month. Increasing the residual moisture content, using the precipitation record from VH, and starting with drier initial conditions at the beginning of January (scenarios 3, 6, and 7 respectively) were similar to the LS base case in terms of timing and likelihood of slope failure. For all four simulations the factor of safety decreased to ~0.8 on January 22 before recovering; however, for the simulation using VH precipitation it decreased again to 0.8 on January 24 whereas the other three simulations remain close to 1. Increasing apparent cohesion from 4 kPa to 8 kPa created the most stable of the LS simulations, with factor of safety values ranging between ~1.6-1.2.

The factor of safety for the VH simulations never dropped below 1. Generally, the values range between ~1.5 and 1.2, except for the lower cohesion simulation which maintains a steady level of about 1.1 until January 22 at which point the heavy

rainfall input causes it to gradually decline. By the end of the month the factor of safety decreased to slightly above 1 (but never crossed the threshold).

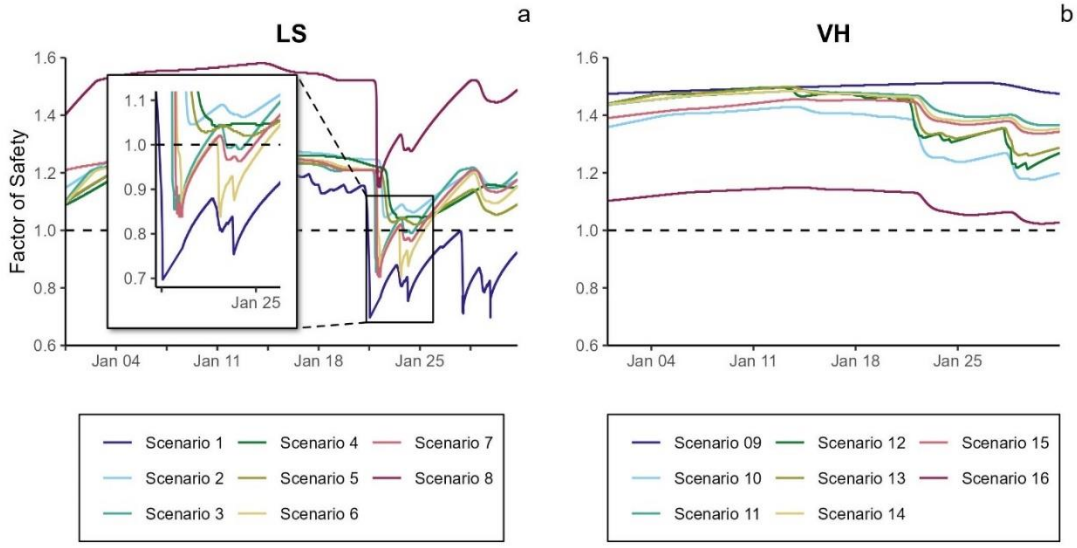

Fig. 3.5 | Time series of factor of safety simulated for all scenarios listed in Table 2 assuming a failure depth of 1.5 meters. **(a)** Alterations to the landslide base model. **(b)** Alterations to the vegetated hillslope base model.

3.4 Discussion

Based on these simulations, apparent cohesion from root reinforcement has by far the largest influence on slope stability, followed by saturated hydraulic conductivity. Notably apparent cohesion is the only variable for which we do not have either field or laboratory measurements and it is also notoriously difficult to constrain at the field scale given spatial variations in species, size, age, and spacing of vegetation (Schmidt et al., 2001). Given the apparent importance of roots within our study system, a more accurate 3D treatment may be warranted that accounts for

spatially variable cohesion as well as temporal parameter variations that occur during the process of failure (e.g., Cohen & Schwarz, 2017). Developing a full 3D model would require a detailed characterization of 3D subsurface geometry and properties that is outside the scope of our current study but may be a useful direction for future work to investigate feedbacks between vegetation and landslide failure that develop during repeated cycles of landsliding.

Saturated hydraulic conductivity also significantly influences the stability of these simulated systems. This is particularly evident from the LS simulations where a faster conductivity caused the hillslope to become unstable 14 hours earlier than the base case and remain unstable for the next 10 days. Additionally, the simulation that alters the VH base case to use the lower LS conductivity maintained the highest factor of safety values of all the VH simulations, reinforcing the conclusion that a higher K_{sat} makes the hillslope less stable, all else being equal. However, we note that these simulations only examine hillslope stability for one month. Over a period of months to years, higher hydraulic conductivity will tend to promote drainage and lead to lower seepage forces (and consequently pore pressures) which would increase hillslope stability. Thus, the effect of hydraulic conductivity will be time scale dependent. Future studies that encompass longer timescales or that combine changes to multiple variables, e.g., increased hydraulic conductivity and drier initial conditions, would be useful to constrain the timescales for these competing effects on landslide stability. Additionally, we note that the extended period of instability that develops when K_{sat} is increased for the LS simulation more accurately matches

observed instability at the site, which occurred off and on between January 21 and January 30, 2016. This suggests that the K_{sat} value used to parameterize the base LS model, which was based on laboratory tests, may be lower than field conditions. This is possibly due to the presence of fast flow pathways which, while less numerous than at VH, may still be more abundant than what is represented by laboratory tests.

Secondary controls on the likelihood of landslide occurrence include θ_s, α, and n. When we increased each of these three parameters for the landslide site, the hillslope remained stable for all of January (although the factor of safety did approach very close to 1 around 23:00 on January 23). Altering any of these three parameters creates more available unsaturated storage within the system and a steeper soil water retention curve, meaning that more water will be required before positive pore pressures can develop. This leads to a lag in saturation timing relative to the base case and an overall decrease in the maximum pore pressures achieved (given identical rainfall inputs) which in turn makes the slope more stable. Similarly, decreasing θ_s, α, and n for VH caused the largest and fastest pore pressure responses of the VH parameter combinations by decreasing the available unsaturated storage and allowing infiltrating water to reach the water table more rapidly.

Antecedent conditions and precipitation differences had a negligible impact on slope stability. The antecedent conditions did have some effect on the modeled pore pressure, as demonstrated by scenario 14 which starts with the “wet” initial conditions and stays wetter during the entire modeled period than the VH base case. However, the effect is not enough to generate instability. Additionally, it is difficult to

disentangle the role of the soil water retention curves vs. different cumulative rainfalls in setting the different antecedent conditions, so it is possible that this effect is already accounted for by alterations in θ_s, α, and/or n.

This insignificance of canopy interception was unexpected given that LS received 228 mm more precipitation than VH did during the full monitoring period (July 11, 2015, to August 9, 2016; Smith et al., 2017). However, closer examination revealed that LS only received 9mm more precipitation during January than VH did. This indicates that cumulative differences in rain fall have a larger effect on subsurface conditions (via antecedent conditions) than differences in any given month. This is likely related to interception rates varying throughout the year due to seasonal changes in canopy cover.

Taken in sum, these results highlight the importance of changes in both hydrologic properties and apparent cohesion in affecting slope stability for reactivated landslides and suggest that decreases in root reinforcement and hydraulic conductivity were the dominant contributors to enhanced landslide potential at LS in 2016. Although we use static values to parameterize the models in this study, the importance of these two factors suggests that the temporal dynamics may be critical to understanding this system and thus estimating hazard. Following an initial landslide, we expect the processes of revegetation, bioturbation, and pedogenesis to gradually restore hillslope stability by increasing root reinforcement and enhancing hillslope drainage (e.g., Fan et al., 2022). Quantifying the timescales for healing after landslide disturbance is important to effectively incorporating path-dependent

landsliding in hazard assessments. These have the potential to vary based on location, climate, and vegetation type. For forests in the Oregon Coast Range, anthropogenic disturbance imparts a lasting legacy on root cohesion of at least a century (Schmidt et al., 2001), whereas grass vegetation in Japan was shown to recover within 12 years after landslide disturbance (Saito et al., 2022). Field studies from the southern Rocky Mountains indicate that six years post-landslide failure neither vegetation nor soil depth had recovered, and the authors speculate that recovery rates may decline in the future as the climate warms and dries (Buma & Pawlik, 2021). Additional field constraints on the recovery rate of different vegetation types and how soil structure coevolves with vegetation growth are needed to accurately model the likelihood of landslide recurrence within time-dependent susceptibility models.

The time-dependent nature of root cohesion and hydraulic conductivity post-failure also raises the question of how repeated cycles of landsliding may affect recovery rates. Aerial imagery of LS illustrates the sequence of landsliding in 2013, followed by partial vegetation regrowth and then subsequently follow up landsliding in 2016 and 2017 (Fig. 3.6). By 2021, the landslide scar has become covered by vegetation, although the tree canopy is not yet as tall as it was prior to landsliding. While vegetation recovery and associated changes in soil structure presumably began to take place after the initial disturbance in 2013, they were interrupted by landslide recurrence happening on a shorter timescale than that which is required for full recovery. The effects of this interruption have not been quantified here but could be significant long-term in repeated cycles of landsliding. In forests that are logged for

example, simulations have shown that repeated harvesting cycles cumulatively decrease root stability (Sidle, 1992). Similar effects are likely relevant for landslide-induced disturbances and as recovery rates change in the future due to changes in climate, these effects may be exacerbated.

Fig. 3.6 | Images from Google Earth showing the changes in tree cover at LS due to landsliding and subsequent vegetation regrowth between 2012 and 2021.

Our ability to answer these questions and to quantify the exact magnitude of change at LS within this study is limited by simplified modeling representation we have adopted. We have employed a 1D representation of two study sites to isolate the effects of our chosen suite of hydrological, environmental, and mechanical variables on landslide recurrence while minimizing the complexity of required input data.

While this treatment is effective as an initial approach, it does limit our ability to analyze the effects of spatial heterogeneity and temporal evolution on our study system. For example, the initial landslide failure caused non-uniform changes in slope and produced a lumpy topography that leads to restricted drainage and shallow rapid earthflows in gently sloping areas of the landslide (Mirus et al., 2017). These topographic effects are not captured in our model system but likely affect where on the hillslope future failures will initiate. Additionally, there is considerable spatial variability recorded in the hydrologic response at different instrument locations and observed within soil pits (Mirus et al., 2017). These effects are not captured within a 1D representation but are likely also important for determining where failures may initiate. Future work developing a full 3D representation of our field system would help address some of these issues while also allowing a more realistic treatment of cohesion.

3.5 Conclusions

Landslides alter the hydrologic, mechanical, and topographic properties of a hillslope in ways that may increase susceptibility to future failures when the initial deposit is not evacuated completely. Field studies of a recurring landslide along the coastal bluffs of Puget Sound identified reductions in hydrologic connectivity and storage that resulted from the initial landslide failure. Here we use a coupled hydromechanical model to quantify the relative importance of individual components of landslide disturbance on landslide hazard persistence. Our analysis indicates that hydraulic conductivity and apparent cohesion from root reinforcement are the two

most influential factors. We expect these two factors to coevolve during the healing process post-disturbance, however recovery rates are likely to vary widely depending on climate, soil type, and vegetation species. Comprehensive measurements of root reinforcement through space and time for different vegetation species are necessary to inform time-dependent landslide susceptibility estimates.

References

AghaKouchak, A., Ragno, E., Love, C., Moftakhari, H., & University of California, I. (2018). *Projected Changes in California's Precipitation Intensity-duration-frequency Curves: A Report for California's Fourth Climate Change Assessment*. California Energy Commission.

Agliardi, F., Scuderi, M. M., Fusi, N., & Collettini, C. (2020). Slow-to-fast transition of giant creeping rockslides modulated by undrained loading in basal shear zones. *Nature Communications*, *11*(1), 1–11. https://doi.org/10.1038/s41467-020-15093-3

Anderson, R. S., & Anderson, S. P. (2010, June 16). Geomorphology: The Mechanics and Chemistry of Landscapes. https://doi.org/10.1017/CBO9780511794827

Baum, R. L., & Reid, M. E. (2000). Ground Water Isolation by Low-Permeability Clays in Landslide Shear Zones. In *Landslides in Research, Theory and Practice* (p. 1: 139-144). Thomas Telford Publishing. https://doi.org/10.1680/lirtapv1.34617.0023

Baum, R. L., Godt, J. W., Harp, E. L., & McMullen, J. P. M. & S. R. (2005). Early warning of landslides for rail traffic between Seattle and Everett, Washington, USA. In *Landslide Risk Management*. CRC Press.

Baum, Rex L., & Johnson, A. M. (1993). Steady movement of landslides in fine-grained soils - a model for sliding over an irregular slip surface. *US Geological Survey Bulletin*, *1842 D*. https://doi.org/10.3133/b1842D

Baum, Rex L., & Reid, Mark. E. (1995). Geology, hydrology, and mechanics of a slow-moving, clay-rich landslide, Honolulu, Hawaii. In W. C. Haneberg & S. A. Anderson (Eds.), *Clay and Shale Slope Instability* (Vol. 10, p. 0). Geological Society of America. https://doi.org/10.1130/REG10-p79

Baum, Rex L., Coe, J. A., Godt, J. W., Harp, E. L., Reid, M. E., Savage, W. Z., et al. (2005). Regional landslide-hazard assessment for Seattle, Washington, USA. *Landslides*, *2*(4), 266–279. https://doi.org/10.1007/s10346-005-0023-y

Baum, R.L., Harp, E. L., & Hultman, W. A. (2000). *Map showing recent and historic landslide activity on coastal bluffs of Puget Sound between Shilshole Bay and Everett, Washington* (USGS Numbered Series No. 2346). *Map showing recent and historic landslide activity on coastal bluffs of Puget Sound between Shilshole Bay and Everett, Washington* (Vol. 2346). U.S. Geological Survey. https://doi.org/10.3133/mf2346

Bayer, B., Simoni, A., Mulas, M., Corsini, A., & Schmidt, D. (2018). Deformation responses of slow moving landslides to seasonal rainfall in the Northern Apennines, measured by InSAR. *Geomorphology*, *308*, 293–306. https://doi.org/10.1016/j.geomorph.2018.02.020

Beeson, H. W., Flitcroft, R. L., Fonstad, M. A., & Roering, J. J. (2018). Deep-Seated Landslides Drive Variability in Valley Width and Increase Connectivity of Salmon Habitat in the Oregon Coast Range. *JAWRA Journal of the American Water Resources Association*, *54*(6), 1325–1340. https://doi.org/10.1111/1752-1688.12693

Benda, L., & Dunne, T. (1997). Stochastic forcing of sediment supply to channel networks from landsliding and debris flow. *Water Resources Research*, *33*(12), 2849–2863. https://doi.org/10.1029/97WR02388

Bennett, G. L., Roering, J. J., Mackey, B. H., Handwerger, A. L., Schmidt, D. A., & Guillod, B. P. (2016a). Historic drought puts the brakes on earthflows in Northern California. *Geophysical Research Letters*, *43*(11), 5725–5731. https://doi.org/10.1002/2016GL068378

Bennett, G. L., Roering, J. J., Mackey, B. H., Handwerger, A. L., Schmidt, D. A., & Guillod, B. P. (2016b). Historic drought puts the brakes on earthflows in Northern California. *Geophysical Research Letters*, *43*(11), 5725–5731. https://doi.org/10.1002/2016GL068378

Bennett, Georgina L., Miller, S. R., Roering, J. J., & Schmidt, D. A. (2016). Landslides, threshold slopes, and the survival of relict terrain in the wake of the Mendocino Triple Junction. *Geology*, *44*(5), 363–366. https://doi.org/10.1130/G37530.1

Berti, M., & Simoni, A. (2010). Field evidence of pore pressure diffusion in clayey soils prone to landsliding. *Journal of Geophysical Research: Earth Surface*, *115*(F3). https://doi.org/10.1029/2009JF001463

Bertolini, G., Guida, M., & Pizziolo, M. (2005). Landslides in Emilia-Romagna region (Italy): strategies for hazard assessment and risk management. *Landslides*, *2*(4), 302–312. https://doi.org/10.1007/s10346-005-0020-1

Blewitt, G., Hammond, W., & Kreemer, C. (2018). Harnessing the GPS Data Explosion for Interdisciplinary Science. *Eos*, *99*. https://doi.org/10.1029/2018EO104623

Bogaard, T. A., & van Asch, T. W. J. (2002). The role of the soil moisture balance in the unsaturated zone on movement and stability of the Beline landslide, France. *Earth Surface Processes and Landforms*, *27*(11), 1177–1188. https://doi.org/10.1002/esp.419

Booth, A. M., McCarley, J., Hinkle, J., Shaw, S., Ampuero, J.-P., & Lamb, M. P. (2018). Transient Reactivation of a Deep-Seated Landslide by Undrained Loading Captured With Repeat Airborne and Terrestrial Lidar. *Geophysical Research Letters*, *45*(10), 4841–4850. https://doi.org/10.1029/2018GL077812

Booth, D. B., Troost, K. G., Clague, J. J., & Waitt, R. B. (2003). The Cordilleran Ice Sheet. In *Developments in Quaternary Sciences* (Vol. 1, pp. 17–43). Elsevier. https://doi.org/10.1016/S1571-0866(03)01002-9

Buma, B., & Pawlik, Ł. (2021). Post-landslide soil and vegetation recovery in a dry, montane system is slow and patchy. *Ecosphere*, *12*(1), e03346. https://doi.org/10.1002/ecs2.3346

Burbank, D. W., Leland, J., Fielding, E., Anderson, R. S., Brozovic, N., Reid, M. R., & Duncan, C. (1996). Bedrock incision, rock uplift and threshold hillslopes in the northwestern Himalayas. *Nature*, *379*(6565), 505–510. https://doi.org/10.1038/379505a0

Bürgmann, R. (2018). The geophysics, geology and mechanics of slow fault slip. *Earth and Planetary Science Letters*, *495*, 112–134. https://doi.org/10.1016/j.epsl.2018.04.062

Callahan, R. P., Riebe, C. S., Pasquet, S., Ferrier, K. L., Grana, D., Sklar, L. S., et al. (2020). Subsurface Weathering Revealed in Hillslope-Integrated Porosity Distributions. *Geophysical Research Letters*, *47*(15). https://doi.org/10.1029/2020GL088322

Carey, J. M., Massey, C. I., Lyndsell, B., & Petley, D. N. (2019a). Displacement mechanisms of slow-moving landslides in response to changes in porewater pressure and dynamic stress. *Earth Surf. Dynam*, *7*, 707–722. https://doi.org/10.5194/esurf-7-707-2019

Carey, J. M., Massey, C. I., Lyndsell, B., & Petley, D. N. (2019b). Displacement mechanisms of slow-moving landslides in response to changes in porewater pressure and dynamic stress. *Earth Surface Dynamics*, *7*(3), 707–722. https://doi.org/10.5194/esurf-7-707-2019

Carsel, R. F., & Parrish, R. S. (1988). Developing joint probability distributions of soil water retention characteristics. *Water Resources Research*, *24*(5), 755–769. https://doi.org/10.1029/WR024i005p00755

Carson, M. A., & Petley, D. J. (1970). The Existence of Threshold Hillslopes in the Denudation of the Landscape. *Transactions of the Institute of British Geographers*, (49), 71–95. https://doi.org/10.2307/621642

Chambers, J. E., Wilkinson, P. B., Kuras, O., Ford, J. R., Gunn, D. A., Meldrum, P. I., et al. (2011). Three-dimensional geophysical anatomy of an active landslide in Lias Group mudrocks, Cleveland Basin, UK. *Geomorphology*, *125*(4), 472–484. https://doi.org/10.1016/j.geomorph.2010.09.017

Chen, X., Hossain, F., & Leung, L. R. (2017). Probable Maximum Precipitation in the U.S. Pacific Northwest in a Changing Climate. *Water Resources Research*, *53*(11), 9600–9622. https://doi.org/10.1002/2017WR021094

Chiang, S.-H., & Chang, K.-T. (2011). The potential impact of climate change on typhoon-triggered landslides in Taiwan, 2010–2099. *Geomorphology*, *133*(3), 143–151. https://doi.org/10.1016/j.geomorph.2010.12.028

Coe, J. (2016). Landslide Hazards and cLimate Change: A Perspective from the United States (pp. 479–523). https://doi.org/10.1201/9781315387789-16

Coe, J. A., Ellis, W. L., Godt, J. W., Savage, W. Z., Savage, J. E., Michael, J. A., et al. (2003). Seasonal movement of the Slumgullion landslide determined from global positioning system surveys and field instrumentation, July 1998-March 2002. *Engineering Geology*, *68*(1–2), 67–101. https://doi.org/10.1016/S0013-7952(02)00199-0

Coe, Jeffrey A. (2012). Regional moisture balance control of landslide motion: Implications for landslide forecasting in a changing climate. *Geology*, *40*(4), 323–326. https://doi.org/10.1130/G32897.1

Coe, Jeffrey A. (2020). Bellwether sites for evaluating changes in landslide frequency and magnitude in cryospheric mountainous terrain: a call for systematic, long-term observations to decipher the impact of climate change. *Landslides*, *17*(11), 2483–2501. https://doi.org/10.1007/s10346-020-01462-y

Cohen, D., & Schwarz, M. (2017). Tree-root control of shallow landslides. *Earth Surface Dynamics*, *5*(3), 451–477. https://doi.org/10.5194/esurf-5-451-2017

Collins, B. D., & Sitar, N. (2008). Processes of coastal bluff erosion in weakly lithified sands, Pacifica, California, USA. *Geomorphology*, *97*(3), 483–501. https://doi.org/10.1016/j.geomorph.2007.09.004

Contreras, I. A., Grosser, A. T., & Ver Strate, R. H. (2012). The Use of the Fully-Grouted Method for Piezometer Installation, 1–20. https://doi.org/10.1061/40940(307)67

Cook, B. I., Ault, T. R., & Smerdon, J. E. (2015). Unprecedented 21st century drought risk in the American Southwest and Central Plains. *Science Advances*, *1*(1), e1400082. https://doi.org/10.1126/sciadv.1400082

Corominas, J., Moya, J., Ledesma, A., Lloret, A., & Gili, J. A. (2005a). Prediction of ground displacements and velocities from groundwater level changes at the Vallcebre landslide (Eastern Pyrenees, Spain). *Landslides*, *2*(2), 83–96. https://doi.org/10.1007/s10346-005-0049-1

Corominas, J., Moya, J., Ledesma, A., Lloret, A., & Gili, J. A. (2005b). Prediction of ground displacements and velocities from groundwater level changes at the Vallcebre

landslide (Eastern Pyrenees, Spain). *Landslides*, *2*(2), 83–96. https://doi.org/10.1007/s10346-005-0049-1

Crozier, M. J. (2010). Deciphering the effect of climate change on landslide activity: A review. *Geomorphology*, *124*(3), 260–267. https://doi.org/10.1016/j.geomorph.2010.04.009

Dahlin, T. (2001). The development of DC resistivity imaging techniques. *Computers & Geosciences*, *27*(9), 1019–1029. https://doi.org/10.1016/S0098-3004(00)00160-6

Damsgaard, A., Egholm, D. L., Beem, L. H., Tulaczyk, S., Larsen, N. K., Piotrowski, J. A., & Siegfried, M. R. (2016). Ice flow dynamics forced by water pressure variations in subglacial granular beds. *Geophysical Research Letters*, *43*(23), 12,165-12,173. https://doi.org/10.1002/2016GL071579

Denlinger, R. P., & Iverson, R. M. (2001). Flow of variably fluidized granular masses across three-dimensional terrain 2. Numerical predictions and experimental tests. *Journal of Geophysical Research: Solid Earth*, *106*(B1), 553–566. https://doi.org/10.1029/2000jb900330

Dibblee, T. W. (2006). Geologic map of the Mount Day quadrangle, Santa Clara & Alameda counties, California. Santa Barbara, CA: Santa Barbara Museum of Natural History.

Dong, L., Leung, L. R., Lu, J., & Gao, Y. (2019). Contributions of Extreme and Non-Extreme Precipitation to California Precipitation Seasonality Changes Under Warming. *Geophysical Research Letters*, *46*(22), 13470–13478. https://doi.org/10.1029/2019GL084225

East, A. E., & Sankey, J. B. (2020). Geomorphic and Sedimentary Effects of Modern Climate Change: Current and Anticipated Future Conditions in the Western United States.

Reviews of Geophysics, *58*(4), e2019RG000692. https://doi.org/10.1029/2019RG000692

Ebel, B. A., Loague, K., Montgomery, D. R., & Dietrich, W. E. (2008). Physics-based continuous simulation of long-term near-surface hydrologic response for the Coos Bay experimental catchment. *Water Resources Research*, *44*(7). https://doi.org/10.1029/2007WR006442

Elrick, D. E., & Reynolds, W. D. (1992). Methods for Analyzing Constant-Head Well Permeameter Data. *Soil Science Society of America Journal*, *56*(1), 320–323. https://doi.org/10.2136/sssaj1992.03615995005600010052x

Fan, L., Lehmann, P., Zheng, C., & Or, D. (2021). The Lasting Signatures of Past Landslides on Soil Stripping From Landscapes. *Water Resources Research*, *57*(12), e2021WR030375. https://doi.org/10.1029/2021WR030375

Fan, L., Lehmann, P., Zheng, C., & Or, D. (2022). Vegetation-Promoted Soil Structure Inhibits Hydrologic Landslide Triggering and Alters Carbon Fluxes. *Geophysical Research Letters*, *49*(18), e2022GL100389. https://doi.org/10.1029/2022GL100389

Feddes, R. A. (1978). *Simulation of field water use and crop yield / R. A. Feddes, P. J. Kowalik, and H. Zaradny*. Wageningen: Pudoc for the Centre for Agricultural Publishing and Documentation.

Ferdowsi, B., Ortiz, C. P., & Jerolmack, D. J. (2018). Glassy dynamics of landscape evolution. *Proceedings of the National Academy of Sciences of the United States of America*, *115*(19), 4827–4832. https://doi.org/10.1073/pnas.1715250115

Finnegan, N. J., Perkins, J. P., Nereson, A. L., & Handwerger, A. L. (2021a). Unsaturated Flow Processes and the Onset of Seasonal Deformation in Slow-Moving Landslides.

Journal of Geophysical Research: Earth Surface, *126*(5), e2020JF005758. https://doi.org/10.1029/2020JF005758

Finnegan, N. J., Perkins, J. P., Nereson, A. L., & Handwerger, A. L. (2021b). Unsaturated Flow Processes and the Onset of Seasonal Deformation in Slow-Moving Landslides. *Journal of Geophysical Research: Earth Surface*, *126*(5), e2020JF005758. https://doi.org/10.1029/2020JF005758

Fleming, R. W., & Taylor, F. A. (1980). *Estimating the costs of landslide damage in the United States* (USGS Numbered Series No. 832). *Estimating the costs of landslide damage in the United States* (Vol. 832). U.S. Geological Survey. https://doi.org/10.3133/cir832

Flinchum, B. A., Steven Holbrook, W., Rempe, D., Moon, S., Riebe, C. S., Carr, B. J., et al. (2018). Critical zone structure under a granite ridge inferred from drilling and three-dimensional seismic refraction data. *Journal of Geophysical Research: Earth Surface*, *123*(6), 1317–1343. https://doi.org/10.1029/2017JF004280

Freeze, R. A. (1979). *Groundwater*. Englewood Cliffs, N.J: Prentice-Hall.

Froude, M. J., & Petley, D. N. (2018). Global fatal landslide occurrence from 2004 to 2016. *Natural Hazards and Earth System Sciences*, *18*(8), 2161–2181. https://doi.org/10.5194/nhess-18-2161-2018

Godt, J. W., Baum, R. L., & Chleborad, A. F. (2006). Rainfall characteristics for shallow landsliding in Seattle, Washington, USA. *Earth Surface Processes and Landforms*, *31*(1), 97–110. https://doi.org/10.1002/esp.1237

Godt, J. W., Baum, R. L., & Lu, N. (2009). Landsliding in partially saturated materials. *Geophysical Research Letters*, *36*(2). https://doi.org/10.1029/2008GL035996

Graymer, R. W., Moring, B., Saucedo, G., Wentworth, C., Brabb, E., & Knudsen, K. (2006). *Geologic map of the San Francisco Bay region*. US Department of the Interior, US Geological Survey Reston, VA, USA.

Griffin, D., & Anchukaitis, K. J. (2014). How unusual is the 2012–2014 California drought? *Geophysical Research Letters*, *41*(24), 9017–9023. https://doi.org/10.1002/2014GL062433

Hahm, W. J., Dralle, D. N., Rempe, D. M., Bryk, A. B., Thompson, S. E., Dawson, T. E., & Dietrich, W. E. (2019). Low Subsurface Water Storage Capacity Relative to Annual Rainfall Decouples Mediterranean Plant Productivity and Water Use From Rainfall Variability. *Geophysical Research Letters*, *46*(12), 6544–6553. https://doi.org/10.1029/2019GL083294

Hahm, W. Jesse, Rempe, D. M., Dralle, D. N., Dawson, T. E., Lovill, S. M., Bryk, A. B., et al. (2019). Lithologically Controlled Subsurface Critical Zone Thickness and Water Storage Capacity Determine Regional Plant Community Composition. *Water Resources Research*, *55*(4), 3028–3055. https://doi.org/10.1029/2018WR023760

Handwerger, A. L., Roering, J. J., & Schmidt, D. A. (2013). Controls on the seasonal deformation of slow-moving landslides. *Earth and Planetary Science Letters*, *377–378*, 239–247. https://doi.org/10.1016/j.epsl.2013.06.047

Handwerger, A. L., Rempel, A. W., Skarbek, R. M., Roering, J. J., & Hilley, G. E. (2016). Rate-weakening friction characterizes both slow sliding and catastrophic failure of landslides. *Proceedings of the National Academy of Sciences of the United States of America*, *113*(37), 10281–10286. https://doi.org/10.1073/pnas.1607009113

Handwerger, A. L., Huang, M.-H., Fielding, E. J., Booth, A. M., & Bürgmann, R. (2019). A shift from drought to extreme rainfall drives a stable landslide to catastrophic failure. *Scientific Reports*, *9*(1), 1569. https://doi.org/10.1038/s41598-018-38300-0

Handwerger, A. L., Fielding, E. J., Huang, M., Bennett, G. L., Liang, C., & Schulz, W. H. (2019a). Widespread Initiation, Reactivation, and Acceleration of Landslides in the Northern California Coast Ranges due to Extreme Rainfall. *Journal of Geophysical Research: Earth Surface*, *124*(7), 2019JF005035. https://doi.org/10.1029/2019JF005035

Handwerger, A. L., Fielding, E. J., Huang, M.-H., Bennett, G. L., Liang, C., & Schulz, W. H. (2019b). Widespread Initiation, Reactivation, and Acceleration of Landslides in the Northern California Coast Ranges due to Extreme Rainfall. *Journal of Geophysical Research: Earth Surface*, *124*(7), 1782–1797. https://doi.org/10.1029/2019JF005035

Handwerger, A. L., Fielding, E. J., Sangha, S. S., & Bekaert, D. P. S. (2022). Landslide Sensitivity and Response to Precipitation Changes in Wet and Dry Climates. *Geophysical Research Letters*, *49*(13), e2022GL099499. https://doi.org/10.1029/2022GL099499

Haque, U., da Silva, P. F., Devoli, G., Pilz, J., Zhao, B., Khaloua, A., et al. (2019). The human cost of global warming: Deadly landslides and their triggers (1995–2014). *Science of The Total Environment*, *682*, 673–684. https://doi.org/10.1016/j.scitotenv.2019.03.415

Hargreaves, G. H. (1994). Defining and Using Reference Evapotranspiration. *Journal of Irrigation and Drainage Engineering*, *120*(6), 1132–1139. https://doi.org/10.1061/(ASCE)0733-9437(1994)120:6(1132)

Helmstetter, A., Sornette, D., Grasso, J.-R., Andersen, J. V., Gluzman, S., & Pisarenko, V. (2004). Slider block friction model for landslides: Application to Vaiont and La Clapière landslides. *Journal of Geophysical Research: Solid Earth*, *109*(B2), 2409. https://doi.org/10.1029/2002JB002160

Hoffman, G. J., & Van Genuchten, M. Th. (1983). Soil Properties and Efficient Water Use: Water Management for Salinity Control. In *Limitations to Efficient Water Use in Crop Production* (pp. 73–85). John Wiley & Sons, Ltd. https://doi.org/10.2134/1983.limitationstoefficientwateruse.c5

Holbrook, W. S., Riebe, C. S., Elwaseif, M., L. Hayes, J., Basler-Reeder, K., L. Harry, D., et al. (2014). Geophysical constraints on deep weathering and water storage potential in the Southern Sierra Critical Zone Observatory. *Earth Surface Processes and Landforms*, *39*(3), 366–380. https://doi.org/10.1002/esp.3502

Hungr, O. (1995). A model for the runout analysis of rapid flow slides, debris flows, and avalanches. *Canadian Geotechnical Journal*, *32*(4), 610–623. https://doi.org/10.1139/t95-063

Hungr, Oldrich, Leroueil, S., & Picarelli, L. (2014). The Varnes classification of landslide types, an update. *Landslides*, *11*(2), 167–194. https://doi.org/10.1007/s10346-013-0436-y

Ikari, M. J., Saffer, D. M., & Marone, C. (2009). Frictional and hydrologic properties of clay-rich fault gouge. *Journal of Geophysical Research: Solid Earth*, *114*(5), 5409. https://doi.org/10.1029/2008JB006089

Imaizumi, F., Sidle, R. C., Togari-Ohta, A., & Shimamura, M. (2015). Temporal and spatial variation of infilling processes in a landslide scar in a steep mountainous region,

Japan. *Earth Surface Processes and Landforms*, *40*(5), 642–653. https://doi.org/10.1002/esp.3659

Iverson, R . M, & Major, J. J. (1987). Rainfall, groundwaterf low, and seasonal motion at Minor Creek landslide, northwestern California: Physical interpretation of empirical relations, Geol. Soc. Am. Bull., 99, 579 -594, 1987., (October), 579–594.

Iverson, R. M. (2000). Landslide triggering by rain infiltration. *Water Resources Research*, *36*(7), 1897–1910. https://doi.org/10.1029/2000WR900090

Iverson, R. M., & Major, J. J. (1987a). Rainfall, ground-water flow, and seasonal movement at Minor Creek landslide, northwestern California: physical interpretation of empirical relations. *Geological Society of America Bulletin*, *99*(4), 579–594. https://doi.org/10.1130/0016-7606(1987)99<579:RGFASM>2.0.CO;2

Iverson, R. M., & Major, J. J. (1987b). Rainfall, ground-water flow, and seasonal movement at Minor Creek landslide, northwestern California: Physical interpretation of empirical relations. *Geological Society of America Bulletin*. https://doi.org/10.1130/0016-7606(1987)99%3C579:RGFASM%3E2.0.CO;2

Iverson, R. M., George, D. L., Allstadt, K., Reid, M. E., Collins, B. D., Vallance, J. W., et al. (2015). Landslide mobility and hazards: implications of the 2014 Oso disaster. *Earth and Planetary Science Letters*, *412*, 197–208. https://doi.org/10.1016/j.epsl.2014.12.020

Iverson, Richard M. (1997). The Physics of Debris Flows. *American Geophysical Union*, (97), 245–296.

Iverson, Richard M. (2005). Regulation of landslide motion by dilatancy and pore pressure feedback. *Journal of Geophysical Research: Earth Surface*, *110*(F2). https://doi.org/10.1029/2004JF000268

Jakob, M., & Lambert, S. (2009). Climate change effects on landslides along the southwest coast of British Columbia. *Geomorphology*, *107*(3), 275–284. https://doi.org/10.1016/j.geomorph.2008.12.009

Jakob, M., Bovis, M., & Oden, M. (2005). The significance of channel recharge rates for estimating debris-flow magnitude and frequency. *Earth Surface Processes and Landforms*, *30*(6), 755–766. https://doi.org/10.1002/esp.1188

Jennings, C., Strand, R., & Rogers, T. (1977). Geologic map of California, scale 1: 750,000. *Calif. Div. of Mines and Geol., Sacramento*.

Jibson, R. W. (2005). The 2005 La Conchita, California, landslide. *Landslides 2005 3:1*, *3*(1), 73–78. https://doi.org/10.1007/S10346-005-0011-2

Jibson, R. W. (2007). Regression models for estimating coseismic landslide displacement. *Engineering Geology*, *91*(2–4), 209–218. https://doi.org/10.1016/J.ENGGEO.2007.01.013

Jones, J. N., Boulton, S. J., Bennett, G. L., Stokes, M., & Whitworth, M. R. Z. (2021). Temporal Variations in Landslide Distributions Following Extreme Events: Implications for Landslide Susceptibility Modeling. *Journal of Geophysical Research: Earth Surface*, *126*(7), e2021JF006067. https://doi.org/10.1029/2021JF006067

Jones, Joshua N., Bennett, G. L., Abancó, C., Matera, M. A. M., & Tan, F. J. (2023). Multi-event assessment of typhoon-triggered landslide susceptibility in the Philippines. *Natural Hazards and Earth System Sciences*, *23*(3), 1095–1115. https://doi.org/10.5194/nhess-23-1095-2023

Keefer, D. K., & Johnson, A. M. (1983a). *Earth flows: Morphology, mobilization, and movement* (USGS Numbered Series No. 1264). *Earth flows: Morphology,*

mobilization, and movement (Vol. 1264). U.S. Geological Survey. https://doi.org/10.3133/pp1264

Keefer, D. K., & Johnson, A. M. (1983b). *Earth Flows : Morphology, Mobilization, and Movement*. Washington D.C., U.S. Government Printing Office.

Kelsey, H. M. (1978). Earthflows in Franciscan melange, Van Duzen River basin, California. *Geology*, *6*(6), 361–364. https://doi.org/10.1130/0091-7613(1978)6<361:EIFMVD>2.0.CO;2

Kirschbaum, D., Kapnick, S. B., Stanley, T., & Pascale, S. (2020). Changes in Extreme Precipitation and Landslides Over High Mountain Asia. *Geophysical Research Letters*, *47*(4), e2019GL085347. https://doi.org/10.1029/2019GL085347

Krzeminska, D. M., Bogaard, T. A., Malet, J.-P., & van Beek, L. P. H. (2013). A model of hydrological and mechanical feedbacks of preferential fissure flow in a slow-moving landslide. *Hydrology and Earth System Sciences*, *17*(3), 947–959. https://doi.org/10.5194/hess-17-947-2013

Lacroix, P., Berthier, E., & Maquerhua, E. T. (2015). Earthquake-driven acceleration of slow-moving landslides in the Colca valley, Peru, detected from Pléiades images. *Remote Sensing of Environment*, *165*, 148–158. https://doi.org/10.1016/j.rse.2015.05.010

Lacroix, P., Handwerger, A. L., & Bièvre, G. (2020a). Life and death of slow-moving landslides. *Nature Reviews Earth & Environment*, *1*(8), 404–419. https://doi.org/10.1038/s43017-020-0072-8

Lacroix, P., Handwerger, A. L., & Bièvre, G. (2020b). Life and death of slow-moving landslides. *Nature Reviews Earth & Environment*, *1*(8), 404–419. https://doi.org/10.1038/s43017-020-0072-8

Larsen, I. J., & Montgomery, D. R. (2012). Landslide erosion coupled to tectonics and river incision. *Nature Geoscience*, *5*(7), 468–473. https://doi.org/10.1038/ngeo1479

Lebedeva, M. I., & Brantley, S. L. (2013). Exploring geochemical controls on weathering and erosion of convex hillslopes: beyond the empirical regolith production function. *Earth Surface Processes and Landforms*, *38*(15), 1793–1807. https://doi.org/10.1002/ESP.3424

Leone, J. D., Holbrook, W. S., Riebe, C. S., Chorover, J., Ferré, T. P. A., Carr, B. J., & Callahan, R. P. (2020). Strong slope-aspect control of regolith thickness by bedrock foliation. *Earth Surface Processes and Landforms*, esp.4947. https://doi.org/10.1002/esp.4947

Leshchinsky, B., Olsen, M. J., Mohney, C., Glover-Cutter, K., Crook, G., Allan, J., et al. (2017). Mitigating coastal landslide damage. *Science*, *357*(6355), 981–982. https://doi.org/10.1126/science.aao1722

Lu, N, & Likos, W. (2004). Rate of capillary rise in soil. *Journal of Geotechnical and Geoenvironmental Engineering*, *130*(6), 646–650.

Lu, Ning, & Godt, J. (2008). Infinite slope stability under steady unsaturated seepage conditions. *Water Resources Research*, *44*(11). https://doi.org/10.1029/2008WR006976

Lu, Ning, & Godt, J. (2012). Hillslope hydrology and stability. Retrieved from https://pubs.er.usgs.gov/publication/70044372

Mackey, B. H., & Roering, J. J. (2011). Sediment yield, spatial characteristics, and the long-term evolution of active earthflows determined from airborne LiDAR and historical aerial photographs, Eel River, California. *GSA Bulletin*, *123*(7–8), 1560–1576. https://doi.org/10.1130/B30306.1

Malet, J. P., Maquaire, O., & Calais, E. (2002). The use of global positioning system techniques for the continuous monitoring of landslides: Application to the Super-Sauze earthflow (Alpes-de-Haute-Provence, France). *Geomorphology*, *43*(1–2), 33–54. https://doi.org/10.1016/S0169-555X(01)00098-8

Malet, J.-P., Maquaire, O., & Calais, E. (2002). The use of Global Positioning System techniques for the continuous monitoring of landslides: application to the Super-Sauze earthflow (Alpes-de-Haute-Provence, France). *Geomorphology*, *43*(1), 33–54. https://doi.org/10.1016/S0169-555X(01)00098-8

Malet, J.-P., van Asch, T. W. J., van Beek, R., & Maquaire, O. (2005). Forecasting the behaviour of complex landslides with a spatially distributed hydrological model. *Natural Hazards and Earth System Sciences*, *5*(1), 71–85. https://doi.org/10.5194/nhess-5-71-2005

Mansour, M. F., Morgenstern, N. R., & Martin, C. D. (2011). Expected damage from displacement of slow-moving slides. *Landslides*, *8*(1), 117–131. https://doi.org/10.1007/s10346-010-0227-7

Mearns, L., McGinnis, S., Korytina, D., Arritt, R., Biner, S., Bukovsky, M., et al. (2017). The NA-CORDEX dataset [NetCDF]. UCAR/NCAR. https://doi.org/10.5065/D6SJ1JCH

Medley, E. W. (2001). Orderly characterization of chaotic Franciscan Melanges. *Felsbau*, *19*(4), 20–33.

Minard, J. P. (1983). Geologic map of the Edmonds East and part of the Edmonds West quadrangles, Washington. *Miscellaneous Field Studies Map*. https://doi.org/10.3133/mf1541

Mirus, B. B., Ebel, B. A., Heppner, C. S., & Loague, K. (2011). Assessing the detail needed to capture rainfall-runoff dynamics with physics-based hydrologic response

simulation. *Water Resources Research*, *47*(3). https://doi.org/10.1029/2010WR009906

Mirus, B. B., Smith, J. B., Benjamin Stark, York Lewis, Abigail Michel, & Baum, R. L. (2016). *Assessing landslide potential on coastal bluffs near Mukilteo, Washington—Geologic site characterization for hydrologic monitoring* (USGS Numbered Series No. 2016–1082). *Assessing landslide potential on coastal bluffs near Mukilteo, Washington—Geologic site characterization for hydrologic monitoring* (Vol. 2016–1082, p. 128). Reston VA: U.S. Geological Survey. https://doi.org/10.3133/ofr20161082

Mirus, B. B., Smith, J. B., & Baum, R. L. (2017). Hydrologic Impacts of Landslide Disturbances: Implications for Remobilization and Hazard Persistence. *Water Resources Research*, *53*(10), 8250–8265. https://doi.org/10.1002/2017WR020842

Montgomery, D. R., & Dietrich, W. E. (1994). A physically based model for the topographic control on shallow landsliding. *Water Resources Research*, *30*(4), 1153–1171. https://doi.org/10.1029/93WR02979

Montgomery, D. R., Dietrich, W. E., Torres, R., Anderson, S. P., Heffner, J. T., & Loague, K. (1997). Hydrologic response of a steep, unchanneled valley to natural and applied rainfall. *Water Resources Research*, *33*(1), 91–109. https://doi.org/10.1029/96WR02985

Moore, P. L., & Iverson, N. R. (2002). Slow episodic shear of granular materials regulated by dilatant strengthening. *Geology*, *30*(9), 843–846. https://doi.org/10.1130/0091-7613(2002)030<0843:SESOGM>2.0.CO;2

Moravec, B. G., White, A. M., Root, R. A., Sanchez, A., Olshansky, Y., Paras, B. K., et al. (2020). Resolving Deep Critical Zone Architecture in Complex Volcanic Terrain.

Journal of Geophysical Research: Earth Surface, *125*(1). https://doi.org/10.1029/2019JF005189

Mualem, Y. (1976). A new model for predicting the hydraulic conductivity of unsaturated porous media. *Water Resources Research*, *12*(3), 513–522. https://doi.org/10.1029/WR012i003p00513

Murphy, C. R., Finnegan, N. J., & Oberle, F. K. J. (2022). Vadose Zone Thickness Limits Pore-Fluid Pressure Rise in a Large, Slow-Moving Earthflow. *Journal of Geophysical Research: Earth Surface*, *127*(6), e2021JF006415. https://doi.org/10.1029/2021JF006415

Nappo, N., Peduto, D., Mavrouli, O., van Westen, C. J., & Gullà, G. (2019). Slow-moving landslides interacting with the road network: Analysis of damage using ancillary data, in situ surveys and multi-source monitoring data. *Engineering Geology*, *260*, 105244. https://doi.org/10.1016/j.enggeo.2019.105244

Nereson, A. L., Davila Olivera, S., & Finnegan, N. J. (2018). Field and Remote-Sensing Evidence for Hydro-mechanical Isolation of a Long-Lived Earthflow in Central California. *Geophysical Research Letters*, *45*(18), 9672–9680. https://doi.org/10.1029/2018GL079430

Nereson, Alexander L. (2018). *History and Drivers of Slow Landslide Movement at Oak Ridge Earthflow, California* (Ph.D.). *ProQuest Dissertations and Theses*. University of California, Santa Cruz, United States -- California. Retrieved from https://www.proquest.com/docview/2182936973/abstract/84115729D5E44E25PQ/1

Nereson, Alexander L., & Finnegan, N. J. (2018). Drivers of earthflow motion revealed by an 80 yr record of displacement from Oak Ridge earthflow, Diablo Range, California, USA. *GSA Bulletin*, *131*(3–4), 389–402. https://doi.org/10.1130/B32020.1

Oakley, N. S. (2021). A Warming Climate Adds Complexity to Post-Fire Hydrologic Hazard Planning. *Earth's Future*, *9*(7), e2021EF002149. https://doi.org/10.1029/2021EF002149

Onda, Y., Tsujimura, M., & Tabuchi, H. (2004). The role of subsurface water flow paths on hillslope hydrological processes, landslides and landform development in steep mountains of Japan. *Hydrological Processes*, *18*(4), 637–650. https://doi.org/10.1002/hyp.1362

Overpeck, J., & Udall, B. (2010). Dry Times Ahead. *Science*, *328*(5986), 1642–1643. https://doi.org/10.1126/science.1186591

Pachauri, R. K., Mayer, L., & Intergovernmental Panel on Climate Change (Eds.). (2015). *Climate change 2014: synthesis report*. Geneva, Switzerland: Intergovernmental Panel on Climate Change.

Palacky, G. J. (1987). Resistivity Characteristics of Geologic Targets. In M. N. Nabighian (Ed.), *Electromagnetic Methods in Applied Geophysics: Volume 1, Theory* (Vol. 3, p. 0). Society of Exploration Geophysicists. https://doi.org/10.1190/1.9781560802631.ch3

Parker, R. N., Hales, T. C., Mudd, S. M., Grieve, S. W. D., & Constantine, J. A. (2016). Colluvium supply in humid regions limits the frequency of storm-triggered landslides. *Scientific Reports*, *6*(1). Retrieved from https://www.cabdirect.org/cabdirect/abstract/20193150874

Pedrazas, M. A., Hahm, W. J., Huang, M., Dralle, D., Nelson, M. D., Breunig, R. E., et al. (2021). The relationship between topography, bedrock weathering, and water storage across a sequence of ridges and valleys. *Journal of Geophysical Research: Earth Surface*, *126*(4), e2020JF005848. https://doi.org/10.1029/2020jf005848

Perkins, J. P., Reid, M. E., & Schmidt, K. M. (2017). Control of landslide volume and hazard by glacial stratigraphic architecture, northwest Washington State, USA. *Geology*, *45*(12), 1139–1142. https://doi.org/10.1130/G39691.1

Perrone, A., Lapenna, V., & Piscitelli, S. (2014). Electrical resistivity tomography technique for landslide investigation: A review. *Earth-Science Reviews*, *135*, 65–82. https://doi.org/10.1016/j.earscirev.2014.04.002

Persad, G. G., Swain, D. L., Kouba, C., & Ortiz-Partida, J. P. (2020). Inter-model agreement on projected shifts in California hydroclimate characteristics critical to water management. *Climatic Change*, *162*(3), 1493–1513. https://doi.org/10.1007/s10584-020-02882-4

Petley, D. N., Carey, J. M., Ng, K.-Y., Massey, C. I., & Froude, M. J. (2017). Understanding patterns of movement for slow moving landslides. *20th Symposium of the New Zealand Geotechnical Society*, 1–11.

Pettit, M. M., Thomas, M. A., & Loague, K. (2014). Retreat of a Coastal Bluff in Pacifica, California. *Environmental & Engineering Geoscience*, *20*(2), 153–162. https://doi.org/10.2113/gseegeosci.20.2.153

Polade, S. D., Gershunov, A., Cayan, D. R., Dettinger, M. D., & Pierce, D. W. (2017). Precipitation in a warming world: Assessing projected hydro-climate changes in California and other Mediterranean climate regions. *Scientific Reports*, *7*(1), 10783. https://doi.org/10.1038/s41598-017-11285-y

PRISM Climate Group, O. S. U. (2014). [Data set]. Retrieved from https://prism.oregonstate.edu

Reid, M. E. (1994). A Pore-Pressure Diffusion Model for Estimating Landslide-Inducing Rainfall. *The Journal of Geology*, *102*(6), 709–717. https://doi.org/10.1086/629714

Reid, M. E., & Iverson, R. M. (1992). Gravity-driven groundwater flow and slope failure potential: 2. Effects of slope morphology, material properties, and hydraulic heterogeneity. *Water Resources Research*, *28*(3), 939–950. https://doi.org/10.1029/91WR02695

Rempe, D. M., & Dietrich, W. E. (2014). A bottom-up control on fresh-bedrock topography under landscapes. *Proceedings of the National Academy of Sciences*, *111*(18), 6576–6581. https://doi.org/10.1073/pnas.1404763111

Rempe, Daniella M., & Dietrich, W. E. (2018). Direct observations of rock moisture, a hidden component of the hydrologic cycle. *Proceedings of the National Academy of Sciences*, *115*(11), 2664–2669. https://doi.org/10.1073/pnas.1800141115

Richards, L. A. (1931). Capillary Conduction of Liquids Through Porous Mediums. *Physics*, *1*(5), 318–333. https://doi.org/10.1063/1.1745010

Riebe, C. S., Hahm, W. J., & Brantley, S. L. (2017). Controls on deep critical zone architecture: a historical review and four testable hypotheses. *Earth Surface Processes and Landforms*, *42*(1), 128–156. https://doi.org/10.1002/esp.4052

Roadifer, J. W., Forrest, M. P., & Lindquist, E. (2009). Evaluation of shear strength of mélange foundation at Calaveras Dam (pp. 20–24). Presented at the Proceedings of the 29th US Soc. for Dams, Annual Meeting and Conference:"Managing our Water Retention Systems", April.

Roberts, S., Jones, J. N., & Boulton, S. J. (2021). Characteristics of landslide path dependency revealed through multiple resolution landslide inventories in the Nepal Himalaya. *Geomorphology*, *390*, 107868. https://doi.org/10.1016/j.geomorph.2021.107868

Robeson, S. M. (2015). Revisiting the recent California drought as an extreme value. *Geophysical Research Letters*, *42*(16), 6771–6779. https://doi.org/10.1002/2015GL064593

Roering, J. J., Kirchner, J. W., & Dietrich, W. E. (2005, May 1). Characterizing structural and lithologic controls on deep-seated landsliding: Implications for topographic relief and landscape evolution in the Oregon Coast Range, USA. *Bulletin of the Geological Society of America*. GeoScienceWorld. https://doi.org/10.1130/B25567.1

Roering, J. J., Mackey, B. H., Handwerger, A. L., Booth, A. M., Schmidt, D. A., Bennett, G. L., & Cerovski-Darriau, C. (2015). Beyond the angle of repose: A review and synthesis of landslide processes in response to rapid uplift, Eel River, Northern California. *Geomorphology*, *236*, 109–131. https://doi.org/10.1016/j.geomorph.2015.02.013

Rubin, R. S. (2002). *Franciscan Complex geology northeast of Calaveras Reservoir, Diablo Range, California* (M.S.). *ProQuest Dissertations and Theses*. San Jose State University, United States -- California. Retrieved from https://www.proquest.com/docview/305457992/abstract/AA4905D8BA944151PQ/1

Saito, H., Uchiyama, S., & Teshirogi, K. (2022). Rapid vegetation recovery at landslide scars detected by multitemporal high-resolution satellite imagery at Aso volcano, Japan. *Geomorphology*, *398*, 107989. https://doi.org/10.1016/j.geomorph.2021.107989

Salve, R., Rempe, D. M., & Dietrich, W. E. (2012). Rain, rock moisture dynamics, and the rapid response of perched groundwater in weathered, fractured argillite underlying a steep hillslope. *Water Resources Research*, *48*(11). https://doi.org/10.1029/2012WR012583

Samia, J., Temme, A., Bregt, A., Wallinga, J., Guzzetti, F., Ardizzone, F., & Rossi, M. (2017). Do landslides follow landslides? Insights in path dependency from a multi-temporal landslide inventory. *Landslides*, *14*(2), 547–558. https://doi.org/10.1007/s10346-016-0739-x

Samia, J., Temme, A., Bregt, A. K., Wallinga, J., Stuiver, J., Guzzetti, F., et al. (2018). Implementing landslide path dependency in landslide susceptibility modelling. *Landslides*, *15*(11), 2129–2144. https://doi.org/10.1007/s10346-018-1024-y

Samia, J., Temme, A., Bregt, A., Wallinga, J., Guzzetti, F., & Ardizzone, F. (2020). Dynamic path-dependent landslide susceptibility modelling. *Natural Hazards and Earth System Sciences*, *20*(1), 271–285. https://doi.org/10.5194/nhess-20-271-2020

Scaringi, G., Hu, W., Xu, Q., & Huang, R. (2018). Shear-Rate-Dependent Behavior of Clayey Bimaterial Interfaces at Landslide Stress Levels. *Geophysical Research Letters*, *45*(2), 766–777. https://doi.org/10.1002/2017GL076214

Schaap, M. G., & Van Genuchten, M. T. (2006). A modified Mualem–van Genuchten formulation for improved description of the hydraulic conductivity near saturation. *Vadose Zone Journal*, *5*(1), 27–34.

Schmidt, K. M., Roering, J. J., Stock, J. D., Dietrich, W. E., Montgomery, D. R., & Schaub, T. (2001). The variability of root cohesion as an influence on shallow landslide susceptibility in the Oregon Coast Range. *Canadian Geotechnical Journal*, *38*(5), 995–1024. https://doi.org/10.1139/t01-031

Schopka, H. H., & Derry, L. A. (2012). Chemical weathering fluxes from volcanic islands and the importance of groundwater: The Hawaiian example. *Earth and Planetary Science Letters*, *339–340*, 67–78. https://doi.org/10.1016/j.epsl.2012.05.028

Schulz, W. H., Kean, J. W., & Wang, G. (2009). Landslide movement in southwest Colorado triggered by atmospheric tides. *Nature Geoscience*, *2*(12), 863–866. https://doi.org/10.1038/ngeo659

Schulz, W. H., McKenna, J. P., Kibler, J. D., & Biavati, G. (2009). Relations between hydrology and velocity of a continuously moving landslide-evidence of pore-pressure feedback regulating landslide motion? *Landslides*, *6*(3), 181–190. https://doi.org/10.1007/s10346-009-0157-4

Schulz, W. H., Smith, J. B., Wang, G., Jiang, Y., & Roering, J. J. (2018). Clayey Landslide Initiation and Acceleration Strongly Modulated by Soil Swelling. *Geophysical Research Letters*, *45*(4), 1888–1896. https://doi.org/10.1002/2017GL076807

Sidle, R. C. (1992). A theoretical model of the effects of timber harvesting on slope stability. *Water Resources Research*, *28*(7), 1897–1910. https://doi.org/10.1029/92WR00804

Sidle, R. C., & Bogaard, T. A. (2016). Dynamic earth system and ecological controls of rainfall-initiated landslides. *Earth-Science Reviews*, *159*, 275–291. https://doi.org/10.1016/j.earscirev.2016.05.013

Simoni, A., Ponza, A., Picotti, V., & Berti, M. (2013). Landslide-Related Sediment Yield Rate in a Large Apenninic Catchment. In C. Margottini, P. Canuti, & K. Sassa (Eds.), *Landslide Science and Practice: Volume 4: Global Environmental Change* (pp. 307–313). Berlin, Heidelberg: Springer. https://doi.org/10.1007/978-3-642-31337-0_39

Šimůnek, J., van Genuchten, M. Th., & Šejna, M. (2008). Development and Applications of the HYDRUS and STANMOD Software Packages and Related Codes. *Vadose Zone Journal*, *7*(2), 587–600. https://doi.org/10.2136/vzj2007.0077

Smith, J. B., Baum, R. L., Mirus, B. B., Michel, A. R., & Stark, B. (2017). *Results of hydrologic monitoring on landslide-prone coastal bluffs near Mukilteo, Washington*

(USGS Numbered Series No. 2017–1095). *Results of hydrologic monitoring on landslide-prone coastal bluffs near Mukilteo, Washington* (Vol. 2017–1095, p. 60). Reston, VA: U.S. Geological Survey. https://doi.org/10.3133/ofr20171095

Swain, D. L., Langenbrunner, B., Neelin, J. D., & Hall, A. (2018). Increasing precipitation volatility in twenty-first-century California. *Nature Climate Change*, *8*(5), 427–433. https://doi.org/10.1038/s41558-018-0140-y

Temme, A., Guzzetti, F., Samia, J., & Mirus, B. B. (2020). The future of landslides' past—a framework for assessing consecutive landsliding systems. *Landslides*, *17*(7), 1519–1528. https://doi.org/10.1007/s10346-020-01405-7

Terzaghi, K. (1943). Theoretical Soil Mechanics. *Theoretical Soil Mechanics*. https://doi.org/10.1002/9780470172766

Thomas, M. A., Mirus, B. B., Collins, B. D., Lu, N., & Godt, J. W. (2018). Variability in soil-water retention properties and implications for physics-based simulation of landslide early warning criteria. *Landslides*, *15*(7), 1265–1277. https://doi.org/10.1007/s10346-018-0950-z

Van Asch, Th. W. J., Buma, J., & Van Beek, L. P. H. (1999). A view on some hydrological triggering systems in landslides. *Geomorphology*, *30*(1–2), 25–32. https://doi.org/10.1016/S0169-555X(99)00042-2

Van Genuchten, M. Th. (1980). A Closed-form Equation for Predicting the Hydraulic Conductivity of Unsaturated Soils. *Soil Science Society of America Journal*, *44*(5), 892–898. https://doi.org/10.2136/sssaj1980.03615995004400050002x

Vogel, T., Cislerova, M., & Sir, M. (1985). Reliability of indirect estimation of soil hydraulic conductivity. *Vodohosp Cas*, *33*(2), 204–224.

Vogel, T., Van Genuchten, M. T., & Cislerova, M. (2000). Effect of the shape of the soil hydraulic functions near saturation on variably-saturated flow predictions. *Advances in Water Resources*, *24*(2), 133–144.

Wakabayashi, J. (1992). Nappes, tectonics of oblique plate convergence, and metamorphic evolution related to 140 million years of continuous subduction, Franciscan Complex, California. *Journal of Geology*, *100*(1), 19–40. https://doi.org/10.1086/629569

Wakabayashi, John, & Medley, E. W. (2004). Geological characterization of Melanges for practitioners. *Felsbau*, *22*(5), 10–18.

Warrick, J. A., Ritchie, A. C., Schmidt, K. M., Reid, M. E., & Logan, J. (2019). Characterizing the catastrophic 2017 Mud Creek landslide, California, using repeat structure-from-motion (SfM) photogrammetry. *Landslides*, *16*(6), 1201–1219. https://doi.org/10.1007/s10346-019-01160-4

Wu, W., & Sidle, R. C. (1995). A Distributed Slope Stability Model for Steep Forested Basins. *Water Resources Research*, *31*(8), 2097–2110. https://doi.org/10.1029/95WR01136

Xu, Y., Schulz, W. H., Lu, Z., Kim, J., & Baxstrom, K. (2021). Geologic controls of slow-moving landslides near the US West Coast. *Landslides*, *18*(10), 3353–3365. https://doi.org/10.1007/s10346-021-01732-3

Zhou, B., & Dahlin, T. (2003). Properties and effects of measurement errors on 2D resistivity imaging surveying. *Near Surface Geophysics*, *1*(3), 105–117. https://doi.org/10.3997/1873-0604.2003001